Improving the Calibration of Airborne Hyperspectral Sensors for Earth Observation

Dissertation

zur

Erlangung der naturwissenschaftlichen Doktorwürde
(Dr. sc. nat.)

vorgelegt der

Mathematisch-naturwissenschaftlichen Fakultät

der

Universität Zürich

von

Karim Lenhard

aus

Deutschland

Promotionskomitee

Prof. Dr. Michael E. Schaepman (Vorsitz)
Prof. Dr. Ross Purves
Dr. Peter Gege (Leitung der Dissertation)
Dr. Andreas Hüni

Zürich, 2015

Mathematisch-naturwissenschaftliche Fakultät
der Universität Zürich

Dissertation
Improving the calibration of airborne hyperspectral sensors for Earth observation
Author:
Karim Lenhard
Remote Sensing Laboratories
Department of Geography
University of Zurich
Winterthurerstrasse 190
CH-8057 Zurich
Switzerland

For Katja.

Contents

Abstract

Hyperspectral sensors are a widely used tool in remote sensing of the Earth's surface. Due to the versatility of the sensors, a multitude of applications profit from or use hyperspectral data, most prominently the assessment of the impact of climate change on the environment.

The acceptance of hyperspectral remote sensing stems, in part, from the relatively easy access to data. Besides several existing and planned spaceborne instruments, airborne sensors are by now a commercial, if expensive, commodity.

The German Aerospace Center (Deutsches Zentrum für Luft- und Raumfahrt, DLR) operates an optical laboratory for the characterization and calibration of airborne hyperspectral sensors, the calibration home base (CHB). This laboratory is needed to close the gap between the extensive characterization efforts performed for spaceborne devices, and the characterization performed by the commercial sensor's manufacturers. Currently, the latter often does not incorporate the possibility of the traceability of calibration, and may not take into consideration sensor properties that require more complex or time-consuming characterisation methods. As the airborne sensors are effectively used to develop and validate methods for spaceborne hyperspectral remote sensing, the same level of detail in characterization needs to be applied to the airborne devices, resulting in similar measurement uncertainties. One objective of this thesis is therefore to assess the impact of the characterization and calibration possible with the CHB on data from airborne hyperspectral instruments. This is shown on a pair of NEO HySpex hyperspectral instruments operated by DLR for the bathymetry of lake Starnberg as an exemplary hyperspectral remote sensing data product.

The requirements for the calibration of future spaceborne hyperspectral instruments include the traceability to the *système international d'unités* (SI). The second part of the thesis therefore deals with different aspects of propagation of measurement uncertainty and traceability. The sensors discussed here are APEX (Airborne Prism EXperiment) and ROSIS (Reflective Optics System Imaging Spectrometer). Two software tools are discussed: First, a database for the storage of the entire APEX laboratory characterization data, with frontends allowing for the rapid analysis of characterization data as well as the generation of the data needed for the calibration.

Within the database, laboratory metadata is always linked to the actual sensor data, which simplifies the tracing of calibration back to the laboratory data. The second software tool is a Monte Carlo simulation of the airborne measurement process of an inland water body. This simulation is based on a sensor model of ROSIS, but other sensor models, such as one of the HySpex instruments, can be implemented. This allows to propagate the uncertainties from the laboratory measurements to airborne data acquisition. Additionally, this simulation can be used to propagate the laboratory calibration uncertainties to final hyperspectral remote sensing products, which can support the development of hyperspectral methods.

Kurzfassung

Hyperspektralsensoren sind ein weitverbreitetes Werkzeug in der Fernerkundung der Erdoberfläche. Aufgrund der Flexibilität der Sensoren profitieren oder nutzen eine Vielzahl von geowissenschaftlichen Anwendungen Hyperspektraldaten. Das prominenteste Beispiel dafür ist die Abschätzung der Auswirkungen des Klimawandels auf die Umwelt.

Die Akzeptanz hyperspektraler Fernerkundung ist auch auf den relativ einfachen Zugang zu entsprechenden Datensätzen zurückzuführen. Neben mehreren bestehenden und für die nahe Zukunft geplanten hyperspektralen Satelliteninstrumenten, sind flugzeuggetragene Instrumente inzwischen kommerziel verfügbar.

Das Deutsche Zentrum für Luft- und Raumfahrt (DLR) betreibt ein Optiklabor für die Charakterisierung und Kalibrierung von flugzeuggetragenen Hyperspektralsensoren, die Calibration Home Base (CHB). Dieses Labor hat zum Zweck, die Lücke zwischen der umfassenden Charakterisierung, die für Satelliteninstrumente durchgeführt werden, und der unvollständigen Charakterisierung, die für die kommerziellen Geräte von deren Herstellern durchgeführt werden, zu schließen. Letztere bieten zum Teil nicht die Möglichkeit der Rückführbarkeit der Kalibrierung. Aufwändigere Messungen können unter Umständen von den Sensorherstellern nicht durchgeführt werden. Da flugzeuggetragene Sensoren für die Entwicklung und Validierung von Messmethoden für satellitengetragenen Geräte dienen, sollten für beide Geräteklassen dieselben Anforderungen für die Charakterisierung, und dadurch für die Messunsicherheiten, gelten. Ein Ziel der vorliegenden Arbeit ist es daher, die mögliche Verbesserung der Kalibrierung von Flugzeugsensoren zu untersuchen. Das wird in dieser Arbeit mit einem kommerziellen NEO HySpex Sensor, welcher vom DLR betrieben wird und in der CHB vermessen wurde, am Anwendungsbeispiel der Bathymetrie des Starnberger Sees analysiert.

Die Anforderungen an die Kalibrierung von Daten zukünftiger Satellitensensoren sehen die Rückführbarkeit der Daten zum *système international d'unités* (SI) vor. Der zweite Teil dieser Arbeit befasst sich daher mit verschiedenen Aspekten der Messunsicherheitsfortpflanzung und Rückführbarkeit. Die behandelten Sensoren sind APEX (Airborne Prism EXperiment) und ROSIS (Reflective Optics System Imaging Spectrometer). Es werden zwei Software-Werkzeuge besprochen: zunächst eine

Datenbank für die Speicherung aller APEX-Charakterisierungsdaten aus dem Labor. Diese Datenbank besitzt Schnittstellen, die zum einen die schnelle Analyse der Labordaten sowie die Erzeugung der für die Kalibrierung der Daten benötigten Datensätzen ermöglichen. Dadurch, dass innerhalb der Datenbank die Labor-Metadaten zu jedem Zeitpunkt mit den eigentlichen Sensordaten verknüpft sind, wird die Rückführbarkeit der Kalibrierungen zu den Labornormalen vereinfacht. Das zweite Software-Werkzeug besteht in einer Monte-Carlo-Simulation von Hyperspektralmessungen. In der Simulation wurde die Datenaufnahme eines Binnengewässers modelliert. Diese Simulation beruht auf einem Sensor-Modell von ROSIS, welches aber durch das eines anderen Sensors, z.B. HySpex, ersetzt werden könnte. Sie erlaubt es, die Messunsicherheiten von den Labormessungen zur Datenerfassung im Flugzeug fortzupflanzen. Zusätzlich kann diese Simulation auch dafür genutzt werden, die Auswirkungen von Unsicherheiten der Labormessungen auf die Endprodukte der Fernerkundungsdaten zu analysieren. Insofern können solche Simulationen bei der Methodenentwicklung für hyperspektrale Fernerkundung unterstützend wirken.

Chapter 1

Introduction

1.1 Hyperspectral remote sensing for Earth observation

Hyperspectral cameras, or imaging spectrometers, are passive optical sensors with many uses in Earth observation. The sensors discussed in this thesis measure the spectral radiance, a physical measure for "brightness" of a light source, of the solar irradiance reflected and scattered by the ground and the atmosphere. The typically covered spectral range spans from the near ultraviolet over the visible part of the light spectrum up to the short wave infrared, i.e. with wavelengths from $\sim 350\,\mathrm{nm}$ to $\sim 2500\,\mathrm{nm}$. The spectral range is sampled with several hundred contiguous spectral channels with individual bandwidths of a few nm. At the same time, these instruments have moderately high spatial resolutions: $\sim 1\,\mathrm{m}$ for airborne instruments, and $\gtrsim 30\,\mathrm{m}$ for spaceborne sensors.

Their usefulness for Earth observation is given by the fact that this sensor class is designed to be very versatile. Hyperspectral data combines the advantages of regular mono- or panchromatic cameras, in that they provide information about size, shape and texture of an object, with the advantages of spectrometers, the possibility to ascertain physical and chemical properties of objects based on their interaction with light (e.g. transmission or reflection) [52].

Applications for hyperspectral data can be found in many disciplines, e.g. precision farming, forestry, change detection in ecological systems, geology or determination of water constituents [52]. Specifically for climate change studies, the Earth observation community has expressed the need for a more reliable and traceable calibration of the sensors [15, 62, 16, 2, 21]. Given the inherent variability of data acquired from natural targets with remote sensing methods, additional variabilities, uncertainties, and systematic effects introduced by the sensors need to be controlled to be able to register the subtle changes caused by climate change.

This thesis focuses on the laboratory calibration of airborne imaging spectrometers. They play a special role in Earth observation as they are used not only for regional monitoring, but also for method development, simulation and validation of spaceborne missions [11, 7, 3]. Therefore, it is essential to have detailed knowledge about the properties of these sensors to calibrate the sensor data and generate reliable scientific results. Additionally, a proper characterization is a prerequisite for the removal of systematic error sources and allows an assessment of the uncertainties associated with the calibrated data.

Please note that the terms "hyperspectral sensor", "hyperspectral camera", "hyperspectral instrument" and "imaging spectrometer" will be used interchangeably in the following.

1.2 The Calibration Home Base

The German Aerospace Center (Deutsches Zentrum für Luft- und Raumfahrt, DLR) operates an optical laboratory for the characterization of airborne imaging spectrometers, the calibration home base (CHB) [20]. With this facility, sensor models can be determined, i.e., a set of mathematical relationships that link the raw sensor data to the physical units of the quantity to be measured. While it was originally commissioned as reference laboratory for APEX (see sec. 1.3), it was designed to accommodate other airborne hyperspectral instruments with similar optical characteristics. The laboratory is used regularly by APEX and DLR-owned instruments, and it is available to and used by third parties, such as other academic institutions and industry.

To enable the calibration measurements described in chap. 2, the CHB provides a set of light sources with well-known and calibrated properties: Integrating spheres and a radiance standard calibrated by PTB (Physikalisch-Technische Bundesanstalt, Germany's national metrology institute) [59, 56] for radiometric calibration, a monochromator assembly and a freely tunable laser for spectral measurements, and a slit-collimator assembly for geometric characterization. Their light beams are guided to the sensors via a rotating mirror on a translation stage to generate optical stimuli for different illumination angles.

As typical characterization procedures consist of several thousand short, individual measurements, the laboratory operation is highly automated via a control software that can be flexibly extended to accommodate new light sources and sensors. Since the laboratory software provides the laboratory settings for the individual measurement steps in a defined form, this allows to automate recurring data analyses as well.

1.3 Pushbroom imaging spectrometers

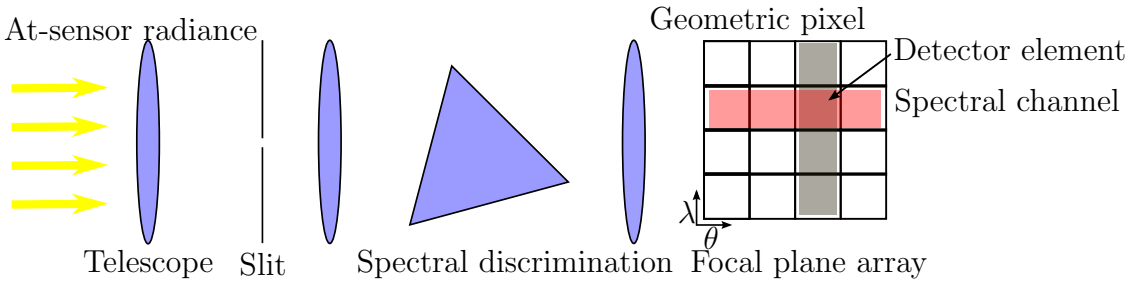

Figure 1.1: Conceptual setup of an imaging spectrometer. A detailed explanation is in the text. Additionally, the wording is defined on an idealized focal plane array (FPA): A detector element corresponds to a single light sensitive FPA pixel. A geometric pixel denotes all detector elements that belong to the same geometric position of the FPA, and a spectral channel signifies all detector elements that belong to the same FPA position along the spectral axis.

The hyperspectral sensors discussed in this thesis are all pushbroom scanners [63]. Their basic functional principle is shown in fig. 1.1. Light is collected via a telescope and focused onto the spectrometer slit. The illuminated slit is then imaged on a two-dimensional detector array. Spectral discrimination is achieved by a dispersive optical element in the light path between slit and detector array, i.e. an optical grating, prism or combination of both. Thus, one dimension of the detector array is used to resolve geometric information, and the second dimension resolves spectral information. Since the sensor works as a line camera, it needs to scan the target. In the case of airborne remote sensing, the scanning motion is provided by an airplane.

The definitions of the terms "detector", "(spectral) channel" and "(geometric) pixel", which will be used in the following, are explained in fig. 1.1

The three sensors discussed in this thesis are:

ROSIS One of the first imaging spectrometers to be built, ROSIS (Reflective Optics System Imaging Spectrometer) [60, 19, 54, 36] was originally intended as a technology demonstrator for a German spaceborne mission for the remote sensing of coastal and inland waters in the 1990s, and could be kept operational for more than two decades by several upgrades to the sensor's electronics, which also increased the total number of simultaneously usable channels and was used in airborne remote sensing until 2008. It has 102 channels, which are sensitive in the spectral range from 430 nm to 840 nm, i.e., mainly in the visible and near infrared. The spectral sampling interval (SSI) of ROSIS is 4 nm, and its spectral resolution is 6 nm FWHM (Full Width at Half Maximum). It has 512 geometric pixels, covering a field of view (FOV) of 16°.

ROSIS is equipped with an in-flight calibration (IFC) light source, consisting of a mercury spectral lamp.

APEX Originally commissioned by the ESA (European Space Agency), APEX (Airborne Prism EXperiment) [32] is now operated by the university of Zürich and the Flemish institute for technological research (VITO). The sensor has a single spectrometer slit that provides light to two spectrometers, one for the ultra-violet, visible and near-infrared spectral range (UV, VIS and NIR) from 380 nm to 972 nm and one for the short wave infrared (SWIR), from 941 nm to 2502 nm. The first spectrometer has up to 334 channels (typically binned for a total channel number of 114), with a SSI that increases from 0.55 nm in the UV to 8 nm in the NIR. Likewise, the spectral resolution degrades from 0.6 nm to 6.3 nm. For the SWIR spectrometer the SSI ranges from 5 nm to 10 nm with the resolution ranging from 6.2 nm to 11 nm with 198 channels.

For both focal plane arrays (FPAs), the FOV of 28° is sampled with 1000 geometric pixels, and, as they are illuminated via the same spectrometer slit, are aligned to achieve coregistration of the recorded hyperspectral data of better than one pixel.

APEX is also equipped with an IFC [12]. Spectral characterization is performed using rare-earth-doped filters, and radiometric measurements with a tungsten-halogen lamp. Changes in the geometric properties of the sensor model can be tracked by analyzing the projections of two wires that cross the spectrometer slit perpendicularly.

NEO HySpex The HySpex sensors are commercial, off-the-shelf systems designed and built by the company Norsk Elektro Optikks (NEO) [47, 48]. One set of instruments was acquired by DLR in 2012 as an EnMAP simulator [39]. The VIS/NIR and the SWIR spectral range are covered by two separate instruments that are mounted onto the same platform. Both sensors are derived from a grating-based design.

The HySpex VNIR-1600 covers the spectral range from 416 nm to 992 nm with a nominal spectral resolution and SSI of 3.5 nm, sampled by 160 channels. Its FOV of 17° is sampled by 1600 geometric pixels. This sensor allows the use of on-camera spectral binning.

The HySpex SWIR-320m-e covers the spectral range from 968 nm to 2497 nm with a nominal spectral resolution of 7 nm and SSI of 6 nm, sampled by 256 channels. Its FOV of 13.5° is sampled by 320 geometric pixels.

Since the instruments have individual principal axes and are not specifically aligned to each other prior to airborne remote sensing and have instantaneous FOVs (IFOVs) differing by a factor of 4, coregistration is only achieved later on in the orthorectification [53] process. Also, no IFCs are built into these instruments, as the sensors are designed to be small and lightweight and the manufacturer assumes stability of the instruments.

Both HySpex instruments are, for airborne data acquisition, typically equipped with FOV-expander lenses that approximately double the FOV at the expense of halved geometric angular resolution.

1.4 Current state of laboratory calibration of airborne imaging spectrometers for Earth observation

A sensor model, resulting from a characterization of a sensor, is required to process the raw data to calibrated at-sensor spectral radiances and to provide uncertainties, as detailed in chap. 2.

Spaceborne instruments are usually calibrated extensively [41, 65, 50], as characterization possibilities are very limited once the instrument is in space and the data provided by the sensor could become unusable for some applications due to insufficient characterization.

Currently, many hyperspectral sensors used in airborne remote sensing are commercial airborne instruments, which usually do not have to meet the calibration requirements of spaceborne instruments. This is probably caused by cost and effort required for a thorough calibration, because realignment and supplementary characterization of the sensor remain possible, and by the fact that many of the scientists responsible for the operation of these instruments do not have a background that familiarizes them with the theory and constraints of measurements. Finally, many remote sensing applications [52] yield "good enough" and "plausible" results using the radiance data generated in the way envisaged by the commercial instrument's manufacturers.

Commercial sensors are usually delivered with a set of "calibration files" that can be used with a proprietary software of the manufacturer to convert raw data to spectral radiances, but often without uncertainty estimates. According to the definition given in sec. 2, it is not conforming to the definition of calibration if no measurement uncertainties are provided, and frequently information about optical distortions and stray light is missing.

To ensure the validity of the sensor models during airborne data acquisition, some instruments are equipped with in-flight calibration light sources (IFC). IFCs allow to notice changes caused by environmental conditions. For example, in an airplane, the instruments are exposed to temperature gradients and vibrations that are not present in the laboratory. While IFCs are common in spaceborne and prototype airborne instruments [50, 61, 22, 60, 10], current commercial, off-the-shelf hyperspectral instruments [47, 28, 58, 26] do not have such components.

Even without IFCs, in-flight characterization is possible, with some limitations,

with methods relying on features in the acquired data: Spectral features of the atmosphere can be used for the characterization of spectral properties, and geometric properties can be assessed using sharp edges with large contrasts in the acquired hyperspectral images [24, 25, 12, 9].

The lack of estimates for the measurement uncertainties becomes even more important when the sensors are not used in isolation for specific studies, but if results are to be compared with those obtained with other instruments [11, 3, 35, 7] or methods are being developed. Meaning that, in consequence, the quality of spaceborne instrument characterization [15, 50, 42], needs to be extended to airborne sensors.

Notably, no publications on the independent characterization of current generation commercial imaging spectrometers can be found, with the exception of DLR's HySpex instruments, which are discussed in this thesis. For prototype, non-commercial, purely scientific instruments, more information is available [60, 49, 32, 8].

Increased dissemination of hyperspectral sensors, e.g., for remote sensing using unmanned airborne vehicles (UAVs), might reinforce these issues, as the very small hyperspectral instruments might suffer more from limitations of the optics design.

1.5 Objectives and structure of this thesis

In this dissertation, concepts and methods to obtain traceably calibrated hyperspectral sensor data are developed and applied to remedy the issues presented in the previous section. Thus, the following objectives are set for this thesis:

1. Development and realization of a detailed measurement concept for a thorough sensor characterization. This includes the characterization of DLR's HySpex sensors.

2. Assessment of the potential improvements to calibrated hyperspectral data, and of the impact on the subsequent data analysis.

3. Extension of the traceability of the calibration chain from the laboratory to airborne measurements.

4. Derivation of requirements for laboratory characterization from target measurement uncertainties.

These objectives are covered in this thesis in the following five chapters:

Chapter 2 This chapter familiarizes the reader with the relevant concepts in the calibration of pushbroom imaging spectrometer data.

Chapter 3 is based on a first-authored, peer-reviewed scientific publication [39]. It addresses the first and third objective and describes the laboratory characterization within the CHB and the data calibration for DLR's HySpex sensors. This publication is self-contained in terms of structure and content.

Chapter 4 is based on a first-authored, peer-reviewed scientific publication [38]. It addresses the first two objectives and estimates the potential improvements to calibrated data by including the additional knowledge from the characterization, and briefly discusses two sensor parameters not covered in the first paper, the FPA nonlinearity and the stray light in the instrument. This is done using the HySpex VNIR and an airborne data take of inland waters. This publication is self-contained in terms of structure and content. Current status: In preparation

Chapter 5 is based on a co-authored peer-reviewed scientific publication [27]. It presents a software framework based on a database that allows for the storage, archiving, evaluating and processing of the laboratory characterization data. This publication partly covers objective 3. This publication is self-contained in terms of structure and content.

Chapter 6 is based on a first-authored, peer-reviewed scientific publication [37]. It addresses the objectives 3 and 4 by presenting a framework that allows for the determination of measurement uncertainties for airborne-based data by implementing a Monte-Carlo-type uncertainty propagation with a ROSIS-based sensor model. This publication is self-contained in terms of structure and content.

Chapter 7 summarizes the main results from the presented publications and provides a conclusion and an outlook.

Chapter 2

Calibration of imaging spectrometer data

Metrological guidelines [31] define calibration as

> Operation that, under specified conditions, in a first step, establishes a relation between the quantity values with measurement uncertainties provided by measurement standards and corresponding indications with associated measurement uncertainties and, in a second step, uses this information to establish a relation for obtaining a measurement result from an indication.

To paraphrase, calibration consists in the first step in the measurement of a standard with the measurement device to be calibrated and to use this measurement to establish a mathematical relationship between the quantity to be measured and the measurement reading indicated by the measurement device. In the second step, this relationship is used to assign values in physical units to other measurements.

The first part of calibration, i.e. the definition of the mathematical relationship, will be referred to as "characterization" in the following. The mathematical relationship will be designated as "sensor model".

A crucial role in this definition of "calibration" lies in the measurement uncertainties. The knowledge of the uncertainties is as important as the ability to measure itself, as otherwise it is impossible to assess the accuracy and precision or significance of a measurement. Meaning that, without uncertainties, two measurements cannot be compared.

Furthermore, a proper characterization of a sensor allows to take systematic measurement effects into account, thus reducing sensor artifacts in the calibrated data.

2.1 Measurement uncertainties

Uncertainties are inherently linked to physical measurements, caused for example by the intrinsic finite accuracy and precision of an instrument, or by the measurement procedure.

Measurement results are usually calculated from several quantities to which uncertainties are associated. To obtain the total, or combined, uncertainty, propagation of measurement uncertainties, or error propagation, is used. The methods are defined by metrological guidelines [29, 33, 30].

2.1.1 Monte Carlo uncertainty propagation

Gaussian error propagation is an analytical error propagation method. It is only applicable if the measurement uncertainties are described by specific probability distribution functions (PDFs), the Gaussian distribution and the t-distribution, and for equations describing the measurement that can be differentiated [30, 29].

For airborne hyperspectral measurements, both conditions are not fulfilled: The PDF for uncertainties originating from polarization sensitivity is not Gaussian, and the dependence of radiometric errors on the shape of the recorded spectra [23] prevent an analytic solution. In such cases, metrological guidelines propose the use of a numerical method, Monte Carlo uncertainty analyses (MCA) [30].

For a MCA, the measurement process has to be simulated. For this thesis, this simulation includes a hyperspectral sensor, based on a sensor model (see 2.2), and an at-sensor radiance. Uncertainty distributions are assigned to the relevant simulation or sensor parameters. The measurement is simulated many times, and the combined uncertainty of the measurement is then given by the distribution of the simulation's results.

2.1.2 Traceability of calibrations

Within the notion of measurement uncertainties and calibration, the concept of traceability needs to be introduced. Traceability [31] designates the possibility to trace a given measurement result back to a reference of the measured quantity through a documented, unbroken chain of calibrations; each of which contributes to the combined measurement uncertainty.

To allow for the comparability of the results, the calibration of hyperspectral sensors for Earth observation have to be traceable to the international system of units (Système International des unités, SI). While spectral standard light sources exist that emit reliably light at specific wavelengths based on immutable physical principles, this is not the case for radiance standards. These have to be calibrated with respect to primary standards, which are operated and provided by national

metrological institutes (NMI) such as PTB (Physikalisch-Technische Bundesanstalt, Germany's NMI) or NIST (National Institute of Standards and Technology", USA's NMI). It is the responsibility of the NMIs to perform intercomparison experiments on their primary standards. The measured differences between the national realizations of these standards are incorporated into the uncertainty of the standard. Thus, if two NMIs operate a primary standard of comparable accuracy and precision, the quality of a calibration does not depend on the NMI.

As implied by its definition, traceability requires not just the actual measurements, but also proper documentation of the measurements and data processing, the confirmation that all measuring equipment was itself calibrated, and a thorough assessment of the uncertainties involved in the calibration measurements.

2.2 Sensor model

The sensor properties, and thus the characterization and calibration methods, can be roughly classified into three parts: the radiometric, the geometric and the spectral properties. The next sections will discuss these briefly. The geometric and spectral properties are reviewed together, as, while they are distinct sensor properties, they derive from the same optical characteristic, the point spread function.

Due to manufacturing tolerances and optical distortions prevalent in imaging spectrometers, each detector element of the FPA has its own set of properties. Thus, the goal of the characterization is to assign a set of properties to each detector element.

2.2.1 Radiometric properties

The main goal of radiometric characterization is to establish a relationship between the at-sensor radiance and the signals in digital numbers (DN), and to provide figures of merit about the data quality.

In the following, the indices i, j are used to indicate the individual pixels of the sensor's FPA, where i denotes the geometric and j the spectral axis. The omission of an index implies that all corresponding detector elements are referenced. S will denote background-corrected signals and $\hat{S}$ background-uncorrected signals.

Radiometric response Assuming a linear radiometric behavior of the FPA, the radiometric response r of each pixel is defined as

$$r_{i,j} = \frac{\hat{S}_{i,j} - S_{\mathrm{bg},i,j}}{t_{\mathrm{int}} \cdot L(\lambda)}, \tag{2.1}$$

with t_{int} the integration time, the spectral radiance $L(\lambda)$, the sensor signal $\hat{S}_{i,j}$ of pixel (i, j), and $S_{\mathrm{bg},i,j}$ the corresponding background signal.

For $r_{i,j}$, the following factorization is expected:

$$r_{i,j} = r_{\text{relative},i,j} \cdot f_{\text{optics},i}(\lambda) \cdot Q_{\text{absolute}}(\lambda). \tag{2.2}$$

The relative response r_{relative} describes the slight variations in detector element properties due to manufacturing tolerances. $f_{\text{optics},i}(\lambda)$ describes the effects of the elements in the sensor's optical path, notably the wavelength-dependent transmission, vignetting effects and inhomogeneities of the spectrometer slit that cause an inhomogeneous distribution of the light on the FPA. $Q_{\text{absolute}}(\lambda)$ describes the wavelength dependence of the sensitivity of the detector semiconductor.

Potential effects that influence eqs. 2.1 and 2.2 related to nonlinearities and stability issues are treated separately later on.

Background signal The background signal is composed of the thermal dark current signal S_{dc} and an electronic offset added during the readout process S_{offset}:

$$S_{\text{bg},i,j} = S_{\text{dc},i,j}(T, t_{\text{int}}) + S_{\text{offset},i,j}. \tag{2.3}$$

S_{dc} depends on the FPA temperature T and the integration time t_{int}. S_{offset} is set by the readout electronics.

Radiometric noise The radiometric noise is an unavoidable part of the total measured signal, and is defined by

$$\Delta S = \sqrt{\Delta S_{\text{dc}}^2 + \Delta S_{\text{ro}}^2 + \Delta S_{\text{phot}}^2} \tag{2.4}$$

for a given detector element, with the dark current noise $\Delta S_{\text{dc}} \propto \sqrt{S_{\text{dc}}}$, and the photon noise $\Delta S_{\text{phot}} \propto \sqrt{S}$, as both are categorized as shot noise [33, 39]. ΔS_{ro} is the noise introduced by the readout electronics.

Figures of merit can be derived from the sensor noise: The noise equivalent radiance (NER or NEΔR) by using eq. 2.1

$$\text{NER}_{i,j} = \frac{\Delta S_{i,j}}{t_{\text{int}} \cdot r_{i,j}}. \tag{2.5}$$

The NER provides a limit for the smallest radiance differences that can be discriminated by the sensor for a given integration time.

A second important figure of merit is the signal-to-noise ratio (SNR). The SNR is

$$\text{SNR} = \frac{S_{i,j}}{\Delta S_{i,j}} \tag{2.6}$$

and indicates how much noise is present in the data for a given signal.

Radiometric resolution The radiometric resolution is a property of the A/D converter of the FPA's readout electronics. The radiometric resolution is typically between 12 bit and 14 bit.

Bad pixels The detector elements that do not operate properly are classified as bad pixels in order to flag the detector elements or exclude their signals from the regular data calibration procedure. The criteria for bad pixel tagging are based on measures of larger nonlinearity, too high or too low signals, or much higher noise than other detector elements.

Polarization sensitivity The FPA and the sensor optics have different responses, reflectances and transmissions for light of different polarization states, meaning that eq. 2.1 is only valid for unpolarized light. During data acquisition, the at-sensor-radiance may be partially polarized, which introduces an additional uncertainty.

A polarization sensitivity P can be assigned to each detector element via

$$P_{i,j} = \frac{A_{i,j}}{\bar{S}}, \tag{2.7}$$

where A is the maximal difference in signal level for two orthogonal linear polarization states, and $\bar{S}$ the corresponding signal level for unpolarized light of the same radiance.

Nonlinearities Different types of nonlinearities can be identified:

1. The signal level is not proportional to the energy impinging on the detector elements.
2. The signal levels behave nonlinearly with respect to the integration time
3. Other electronic issues such as memory effects or smearing.

Since these effects are highly specific for each combination of FPA and readout electronics, a helpful, generic mathematical description does not exist. Thus, one can just state that the eqs. 2.1 and 2.2 need to be appended to correct for nonlinearities. Optical stray light manifests itself as a nonlinearity of the first type and will be discussed in sec. 2.2.2.

2.2.2 Imaging properties

The imaging properties of an optical system can be characterized by its point spread functions (PSF), which describe the light distribution on the focal plane of a monochromatic point source. The geometric line spread functions (LSF) and spectral response functions (SRF) that are described in the following are cross-sections through the PSFs.

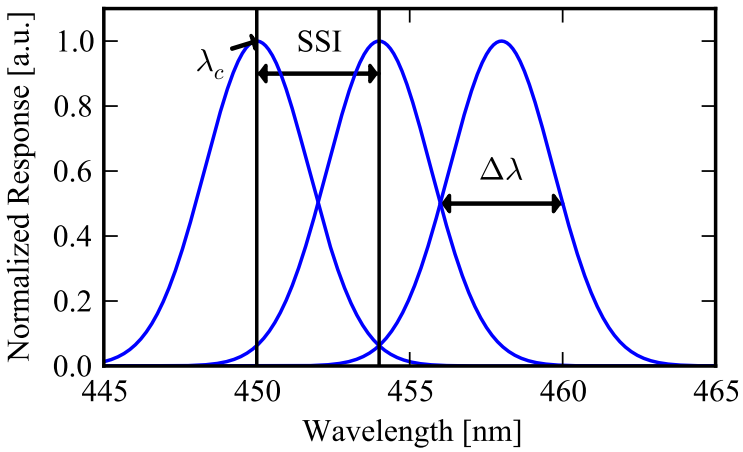

Figure 2.1: Three exemplary neighboring spectral response functions of one geometric pixel, illustrating the definitions of center wavelength λ_c, spectral resolution $\Delta\lambda$ and spectral sampling interval (SSI). The geometric LSFs have analogous quantities: The viewing angle, the angular resolution and the across-track sampling interval.

Spectral properties The spectral properties of each detector element are contained in the SRF. As part of the characterization, the SRF is measured for a subset of all pixels. Using the measurement results, a functional description can be found for the SRFs. From this description, key parameters of the SRF can be derived, notably the center wavelength λ_c and the spectral resolution $\Delta\lambda$. Their definition is illustrated in fig. 2.1. In this case, $\Delta\lambda$ is defined as the full width at half maximum (FWHM) of the SRF.

The goal of the spectral calibration is to assign a set of parameters $(\lambda_c, \Delta\lambda)$ to each detector element. As the SRFs cannot be determined directly for every pixel as the required measurement time would be excessive, the key parameters are assigned to the pixels using interpolation. The spectral parameters are then stored in a look-up-table.

From this look-up-table, other spectral figures of merit can be derived, such as the spectral sampling interval (SSI), which is defined as the spectral range between two adjacent spectral channels, i.e.,

$$\mathrm{SSI}_{i,j} = |\lambda_{c,i,j+1} - \lambda_{c,i,j}|. \tag{2.8}$$

The smile distortion can also be computed from the look-up-table. Spectral smile denotes the optical distortion that causes the center wavelength of a spectral channel to change with geometric pixel position, i.e., $\lambda_{c,i,j} \neq \lambda_{c,i',j}$. The magnitude of the

smile distortion can be defined as

$$M_{\text{smile,j}} = \max\left(\frac{\lambda_{\text{c, center},j} - \lambda_{\text{c},i,j}}{\text{SSI}}\right), \tag{2.9}$$

$$M_{\text{smile}} = \max\left(M_{\text{smile,j}}\right). \tag{2.10}$$

M_{smile} being in the units of channels and $\lambda_{\text{c, center},j}$ being the center wavelength of the detector element at the geometric center of the FPA and belonging to channel j.

Geometric properties The geometric properties of each detector element are contained in the across- and along-track LSFs. Analogously to the spectral parameters, the LSFs of a subset of pixels is measured, and across- and along-track viewing angles and resolutions ($\theta_{\text{along}}, \theta_{\text{across}}, \Delta\theta_{\text{along}}, \Delta\theta_{\text{across}}$) are derived for every detector element. The mapping from these parameters to the detector elements is carried out via a look-up-table.

Again, characteristic numbers can be derived from this look-up-table: The across-track sampling interval ASI

$$\text{ASI}_{i,j} = |\theta_{\text{across},i+1,j} - \theta_{\text{across},i,j}|, \tag{2.11}$$

and the keystone magnitude:

$$M_{\text{keystone,i}} = \max\left(\frac{\theta_{\text{across},i,\text{center}} - \theta_{\text{across},i,j}}{\text{ASI}}\right), \tag{2.12}$$

$$M_{\text{keystone}} = \max\left(M_{\text{keystone,i}}\right). \tag{2.13}$$

The optical distortion referred to as keystone denotes, for a geometric pixel, the change in viewing angles for different spectral channels, i.e., $\theta_{i,j} \neq \theta_{i,j'}$.

Stray light Stray light can be classified into two categories: in-band and out-of-band stray light. Out-of-band stray light designates light that originates outside of the nominal FOV of the instrument or outside of its nominal spectral range and still causes the sensor to register a signal. This kind of stray light can only be attenuated through hardware modifications on the sensor such as the addition of baffles or spectral filters; corrections within the data processing are difficult, as the relation between out-of-band stray light and the actually imaged data is usually not known.

In-band stray light on the other hand can be effectively corrected if the stray light distribution functions (SDF) are known. The SDFs correspond to the PSFs, with the difference that for stray light correction, the SDFs have to be known with much higher radiometric resolution than the LSFs and SRFs. I.e., while typical LSFs and SRFs of hyperspectral instruments are measured over two or three orders of magnitude,

which is sufficient for orthorectification and atmospheric correction algorithms, the stray light distribution function needs to be measured over a radiometric range of 10^5 or better [40, 1].

If the SDFs are known, an analytical correction algorithm exists [66, 45, 67]. For the case of a line array spectrometer, the correction is performed according to

$$S_{\text{corr}} = \mathbf{C} \cdot S_{\text{meas}}, \tag{2.14}$$

where $\mathbf{C}$ is a matrix that contains the SRFs of every channel, S_{meas} is a vector that contains the measured raw signals of the spectrometer, corrected for dark current and nonlinearities, and S_{corr} is then the stray light corrected signal. $\mathbf{C}$ has the dimension (channels×channels).

This correction scheme can be canonically extended to imaging spectrometers [67]. For this, the vectors S_{meas} and S_{corr} are replaced by the image frame arrays, and $\mathbf{C}$ becomes a higher-dimensional linear transformation in form of a tensor, with the dimension (pixels×channels)^2. In this case, $\mathbf{C}$ contains information of all detector elements PSFs, again over the entire FOV and spectral range of the sensor.

Unfortunately, the dimension of the tensor is too large to be practically usable: For the HySpex VNIR-1600, the tensor would use close to 245 GiB of memory, assuming a 4-byte float representation of the tensor entries.

To reduce the tensor size, the SDFs and the correction are computed on a grid of lower resolution than the FPA. This approach mostly corrects the diffuse stray light. This omits the correction of focussed "ghost images".

Stability Due to changes in atmospheric pressure Δp or temperature ΔT between the laboratory and the airborne measurement conditions, the path between the optical elements, specifically the relative position between the spectrometer slit and the FPA, can change. Sensor properties may also change due to unwanted realignment of the optical components, caused by mechanical vibrations, shock or stress introduced by the sensor mount. Since the sensor might not be in thermodynamic equilibrium, the state of the sensor is not necessarily characterized completely by Δp, ΔT, but can depend on a hysteresis [10].

Sensor instabilities can affect many sensor model parameters. The changes that are easiest to detect are shifts of the center wavelengths and shifts of the spectrometer slit, which affects the radiometry through striping.

2.3 Determination of sensor model parameters

In the following, the measurement methods and setups used for the determination of the sensor parameters discussed in the previous section will be briefly described.

Additional information about the measurement procedures can be found in [20, 33, 39, 38].

2.3.1 Radiometry

Radiometric response To determine r according to eq. 2.1, one has to determine the background signal S_{bg} and measure a light source that provides a calibrated spectral radiance $L(\lambda)$. Typically, the spectral radiance source is an integrating sphere or a diffuse reflectance panel [59], illuminated by a white, e.g. spectrally broadband light source, such as incandescent light bulb. An alternate, more complex approach uses tunable lasers for radiometric calibration [6, 55].

The factors of r, r_{relative}, $f_{\mathrm{optics}}(\lambda)$ and $Q_{\mathrm{absolute}}(\lambda)$ (see eq. 2.2) can be determined individually prior to the full assembly of a sensor. This information can be of use if additional corrections for stability issues need to be implemented, e.g. if the image of the slit moves with respect to the focal plane due to mechanical stress.

Background signal As the dark current signal level can prone to change, the background signal is recorded shortly before or after each data acquisition. This is usually done by closing a shutter and recording several hundred background frames; their average is then used for the correction.

Sensor noise To determine the radiometric noise ΔS, the instrument is illuminated at several different signal levels. While ΔS can be pixel-dependent, in practice the noise level is often similar for all detector elements. In this case, a single measurement of a broadband light source with the assembled instrument can yield an estimate of the noise, as the spectral discrimination and the spectrally varying response to light of different wavelengths by the FPA will cause a wide range of signal levels.

The individual components of ΔS, see eq. 2.4, can be separated by measuring at different integration times and signal levels.

Bad pixels Bad pixels are defined using limits on the maximally allowed deviations from the average signal or noise levels of other pixels. The signal measured from bad pixels is usually replaced with a signal level derived from neighboring pixels.

Determination of bad pixels is usually performed by illuminating the FPA directly and homogeneously. Bad pixel detection becomes more complicated with the fully assembled spectrometer due to the uneven illumination of the FPA caused by the optical system. The location of the bad pixels on the FPA is stored in a look-up-table, the bad pixel map.

Polarization sensitivity Polarization sensitivity can be measured using an integrating sphere as a broadband light source in combination with a broadband linear polarizer. By rotating the polarizer in defined angles using a rotation stage, the sensitivity can be derived.

Nonlinearities The nonlinearity with respect to the signal level can be assessed by illuminating the FPA at several well defined irradiance levels. Nonlinearities with respect to the at-sensor-radiance are not expected.

The nonlinearity with respect to the integration time can be ascertained using a stable light source and changing the integration time of the sensor. The signals normalized to the integration time should remain constant.

Nonlinearities based on other electronic effects are too specific to be treated generally, and can involve tweaking the electronic parameters of the readout electronics.

2.3.2 Imaging properties

Spectral properties The SRFs can be measured by illuminating the sensor with a collimated light beam originating from a monochromator. By scanning the monochromator's wavelength, the SRFs of channels of a single geometric pixel can be probed. By changing the incidence angle of the monochromator beam onto the sensor's aperture, the SRFs of different geometric pixels can be measured. As the beam is collimated, this method has the drawback of being able to illuminate only individual geometric pixels. As detailed above, the derived SRF parameters center wavelength and resolution are interpolated between the angular positions at which they were measured.

Another method uses the light from a tunable laser, which is coupled into the instrument via an integrating sphere. This has the advantage of illuminating the FOV of the sensor completely, thus allowing the simultaneous measurements of all SRFs of one channel.

Geometric properties For the measurement of the LSFs, the sensor is illuminated with a collimated beam of a narrow, back-illuminated slit. Focal length of the collimator and size of the slit are chosen so that, excluding diffraction, the image of the slit on the FPA is smaller than the size of the detector elements.

The slit is illuminated with an incandescent lamp, so that the LSFs are measured for all channels of the examined geometric pixels simultaneously. By changing the incidence angle of the collimated beam on the sensor aperture, the LSF can be measured.

Stray light For the stray light correction discussed in the following, the SDFs were acquired with PTB's PLACOS (Pulsed Laser for Advanced Characterization of Spectroradiometers) setup [44].

To be able to measure the SDFs or PSFs of the sensors with a resolution that is higher than the radiometric resolution of the sensors ($< 10^{-5}$), the SDFs are measured with a two-step method:

1. Measurement at a signal level where the illuminated pixel, as well as surrounding ones, are saturated. This allows to characterize the "long tails" of the SDFs that would otherwise be below the radiometric resolution of the FPA.

2. Measurement at an illumination where no saturation occurs, by reducing the impinging radiance by a defined factor. This allows to normalize the first measurement.

The light source used in PLACOS is a laser that is freely tunable in the spectral range from 410 nm to 2500 nm. The laser light is coupled into the sensor using a collimator, so that only a few detector elements are illuminated.

The CHB is currently being upgraded to incorporate a similar setup for stray light measurements.

Stability The stability of an instrument can be assessed by comparing the results of spectral, geometric or radiometric laboratory characterization measurements with prior measurements. This yields information about long-term stability, i.e., on the time scale between characterization measurements, under laboratory conditions.

To assess the short-term stability, i.e., on a time scale of single data takes, of the instruments during in-flight data acquisition, one can either use an IFC, if available for that sensor, or use methods that rely on the use of spectral and spatial features in the recorded data. Using a climate chamber, the airborne conditions could be reproduced in the laboratory. The CHB is lacking such a setup.

Chapter 3

Independent Laboratory Characterization of NEO HySpex Imaging Spectrometers VNIR-1600 and SWIR-320M-E

This chapter has been published as: Lenhard, K., Baumgartner, A., & Schwarzmaier, T. (2015). Independent Laboratory Characterization of NEO HySpex Imaging Spectrometers VNIR-1600 and SWIR-320m-e. IEEE Transactions on Geoscience and Remote Sensing.

1828 IEEE TRANSACTIONS ON GEOSCIENCE AND REMOTE SENSING, VOL. 53, NO. 4, APRIL 2015

Independent Laboratory Characterization of NEO HySpex Imaging Spectrometers VNIR-1600 and SWIR-320m-e

Karim Lenhard, Andreas Baumgartner, and Thomas Schwarzmaier

***Abstract*—The Remote Sensing Technology Institute (Institut für Methodik der Fernerkundung) of the German Aerospace Agency (DLR) operates two sensors for airborne hyperspectral imaging, i.e., a Norsk Elektro Optikk A/S (NEO) HySpex VNIR-1600 and a NEO HySpex SWIR-320m-e. Since these sensors are used for the development of physically based inversion algorithms, atmospheric correction algorithms and for calibration/validation activities, their properties need to be characterized in detail, and an accurate calibration is mandatory. The characterization is performed at the calibration laboratory of DLR for imaging spectrometers in Oberpfaffenhofen. Key results of the characterization are assessments of the radiometric, spectral, and geometric performances, including the typical optical distortions prevalent in pushbroom imaging spectrometers, keystone and smile, and the associated measurement uncertainties. Potential sources of systematic error, the detector nonlinearity and the polarization sensitivity are discussed. The radiometric calibration is traceably performed to the German national metrology institute Physikalisch-Technische Bundesanstalt, whereas the spectral measurements can be traced back to the spectral properties of atomic line lamps. The implemented level 0 to level 1 calibration procedure is presented as well.**

***Index Terms*—Calibration, characterization, hyperspectral, HySpex.**

I. Introduction

THE goal of this paper is to present the results of the calibration and characterization efforts performed on the Norsk Elektro Optikk (NEO) HySpex VNIR-1600 and SWIR-320m-e imaging spectrometers [1] that were acquired by the German Aerospace Agency (DLR) for the development of physically based inversion algorithms, atmospheric correction and for calibration/validation activities, as well as for the preparation of the EnMAP mission [2]. The measurements are performed in the calibration laboratory (CHB) of DLR [3] for imaging spectrometers in Oberpfaffenhofen, Germany, which is also the calibration home base for APEX (the Airborne Prism EXperiment) [4] and that is available to third parties for measurements.

Manuscript received October 15, 2013; revised April 16, 2014 and July 12, 2014; accepted August 1, 2014.

The authors are with the Deutsches Zentrum für Luft- und Raumfahrt, Institut für Methodik der Fernerkundung, 82234 Oberpfaffenhofen, Germany (e-mail: karim.lenhard@dlr.de; andreas.baumgartner@dlr.de; thomas.schwarzmaier@dlr.de).

Color versions of one or more of the figures in this paper are available online at http://ieeexplore.ieee.org.

Digital Object Identifier 10.1109/TGRS.2014.2349737

TABLE I
PROPERTIES OF THE HYSPEX IMAGING SPECTROMETERS WITH THE FOV EXPANDERS. WITHOUT THE EXPANDERS, THE FOVS AND IFOVS ARE APPROXIMATELY HALVED

	VNIR-1600	SWIR-320m-e
Detector technology	Si CCD	HgCdTe CMOS
Spectral range	416 – 992 nm	968 – 2497 nm
Spectral sampling interval	3.6 nm	6 nm
Spectral bandwidth	3.5 nm	7 nm
FOV	34.5°	27.2°
IFOV (across track)	0.37 mrad	1.49 mrad
IFOV (along track)	0.5 mrad	1.04 mrad
Pixels / line	1600	320
Channels	160	256
Radiometric quantization	12 bit	14 bit
Max. frame rate	135 Hz	100 Hz
Detector temperature	ambient	203 K

While both sensors were characterized by the manufacturer during assembly and prior to their delivery to DLR, an independent characterization of the sensors is performed to base subsequent scientific measurements and data analysis on detailed knowledge of the sensor properties and behaviors, as well as a radiometric calibration that is traceable to the système international (SI) units via the German national metrology institute Physikalisch-Technische Bundesanstalt (PTB).

The characterization presented here is similar to those performed for other remote sensing imaging spectrometers [4]–[8] to obtain a clear understanding of the specifics of the instruments and to provide the processing steps of radiometric calibration, atmospheric correction and orthorectification with the required sensor data.

II. Sensors

The main properties of the HySpex pushbroom imaging spectrometers are listed in Table I. For typical in-flight measurements, both sensors are equipped with field-of-view (FOV) expander lenses that approximately double the FOVs to reduce the number of flight lines required to cover a target area at the cost of higher ground sampling distances at respectively, lower spatial resolution.

The detector used in the visible and near-infrared (VNIR) camera is a Kodak KAI2020 that is part of a Adimec-1600m/D camera [9], and the detector used in the short-wave infrared (SWIR) camera is a MARS SW chip from SOFRADIR [10]. The detector array of the SWIR sensor is actively temperature controlled.

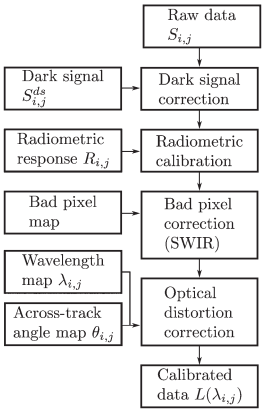

Fig. 1. Schematic of the level 0 to level 1 calibration procedure. Note that for the VNIR sensor, the raw data is already corrected for bad pixel by the camera software.

The VNIR sensor operates in one of three spectral binning modes, $2\times$, $4\times$, and $8\times$. Note that no $1\times$-binning option is available and that the binning patterns are fixed by the manufacturer. For the $4\times$ binning, the signals of two neighboring $2\times$-binning channels are combined pairwise, and the $8\times$ binning is created by combining four neighboring $2\times$-binning channels.

If not mentioned otherwise, statements are referring to and measurements are performed with the sensor with the highest spectral resolution, the $2\times$-binning mode.

The detector array of the VNIR sensor is logically divided along the spatial axis into two parts that are independently read out. This is noticeable by different dark signal levels and slightly different radiometric responses.

Unless stated otherwise, the results presented in the following for the HySpex SWIR exclude the data from bad pixels.

III. Methods

A. Calibration Procedure

The following steps are performed for the conversion to physical units, i.e., level 0 to level 1 calibration, of raw hyperspectral data. These steps are illustrated in Fig. 1 and correspond to the calibration procedure used by NEO, except for the correction of optical distortions. The distinction is that the calibration data that is used now stems from the measurements described in this article.

In the following, detector element denotes a single light-sensitive element of the 2-D detector array, channel denotes a row in spectral direction on the detector array, and pixel denotes a spatial column on that array. The subscripts i, j will be used to denote individual elements of the detector array. The first index indicates a channel number, whereas the second one indicates a pixel number.

1) Radiometric Calibration: The raw data coming from the sensor is radiometrically calibrated using the equation

$$L_{i,j} = \frac{S_{i,j} - S^{\mathrm{ds}}_{i,j}}{R_{i,j} \cdot t_{\mathrm{int}}} \tag{1}$$

where L is the at-sensor radiance in $\mathrm{mW/m^2 \cdot nm \cdot sr}$, S is the signal measured by the sensor in digital numbers (DNs), S^{ds} is the dark signal in DN, R is the radiometric response in $\mathrm{DN \cdot m^2 \cdot nm \cdot sr/\mu s \cdot mW}$, and t_{int} is the integration time in μs. This assumes a linear relationship between the radiance, the integration time, and the sensor signal. The determination of the radiometric responses is described in Section III-B2.

The dark signal S^{ds} is the sum of the thermal dark current signal and an electronic offset. The dark signal is recorded by the sensors automatically for each data acquisition. For this, the shutter closes, 200 frames are acquired, and an averaged frame is stored in the header of the data file. The VNIR sensor acquires the dark signal before each data acquisition, and the SWIR sensor before and after each acquisition. In the SWIR case, both averaged frames are stored separately. The frame used for the correction is generated from a linear interpolation between the two stored frames. This is possible as the changes in dark signal during the time span of a data acquisition is small compared with the noise of the sensors, see Section III-B1.

The first 100 frames of data acquired with the NEO software for airborne data acquisition are discarded, as they may exhibit a lower than expected signal level.

2) Bad Pixel Correction: For the SWIR sensor, the bad pixels are corrected after the radiometric calibration. In this case, the bad pixel map is provided by NEO. For the VNIR sensor, the bad pixel map is provided by Adimec, i.e., the manufacturer of the camera. The bad pixel correction is performed on camera prior to the storage of the raw data. In both cases, the signals of the bad pixels are replaced using linear interpolation along the spectral direction. More information about the determination of bad pixels is found in Section III-B4

3) Optical Distortion Correction: Spectral smile and keystone are optical distortions occurring in pushbroom imaging spectrometers [11]. Smile denotes the change of the central wavelength of a channel over the FOV, and keystone denotes changes in the viewing angle across the channels of the same pixel.

The last step in the calibration procedure is the correction of these distortions. For this, two mappings are required: 1) one that assigns a central wavelength to each detector element, i.e., the wavelength map; and 2) one that assigns an across-track viewing angle to each detector element, i.e., the across-track angle map. These maps are a result of the spectral and geometric characterization, see Section III-B7 and B8.

The distortions are simultaneously corrected by resampling the data using bicubic spline interpolation [12].

This correction step is not performed by the manufacturer's calibration procedure and is optional in our procedure, as these corrections can alternately be performed during atmospheric correction and orthorectification. Smile and keystone correction can also be performed independently.

B. Measurement Setups

Here, the setups for the measurements of the different sensor parameters are described. All activities take place within the CHB [3].

Most radiometric measurements are performed on the large integrating sphere of the CHB. It has a diameter of 1.65 m,

a large aperture of 55 cm × 40 cm and is equipped with 18 quartz–tungsten–halogen (QTH) lamps that can be switched on in different combinations to produce varying radiance levels. The inside of the sphere is coated with $BaSO_4$.

1) Dark Signal: To investigate the stability of the dark signal and, hence, the quality of the dark signal correction, two sets of measurements are performed for both sensors:

- ten consecutive measurements of 5000 frames with constant illumination from the integrating sphere.
- close to 200 consecutive measurements of 25 frames each with low illumination from the monochromator.

From each of these measurements, the automatically acquired averaged dark signal frames are analyzed. The first set of measurements corresponds to in-flight data acquisition. The second set resembles laboratory operations.

For the VNIR sensor, the dark signal frames from the beginning of two consecutive measurements are compared with each other, and for the SWIR sensor, the frames of the same measurement, taken at the beginning and the end of each data acquisition. Bad pixels are corrected according to the correction scheme aforementioned.

To determine the dependence of the dark signal on the integration time, the signal is measured in darkness by recording 1000 frames and determining noise and the average dark signal for each detector element. This is done at 11 integration times, for the VNIR sensor from 3 to 32 ms, and for the SWIR sensor from 1 to 12 ms.

2) Radiometric Response: The spectral radiance standard of CHB is RASTA [13]. This radiance standard is traceable to SI units via PTB, where it has been extensively characterized and calibrated. The radiometric responses of both HySpex sensors are measured by illuminating them directly with RASTA. However, due to constraints in the viewing angle geometry for the spectral radiance measurement of RASTA, this is only feasible for the pixels at the geometric center of the FOV of the HySpex sensors.

To obtain the radiometric responses $R_{i,\mathrm{center}}$, the following equation is used:

$$R_{i,\mathrm{center}} = \frac{S_{i,\mathrm{center}} - S^{\mathrm{ds}}_{i,\mathrm{center}}}{L_{\mathrm{RASTA}}(\lambda_i) \cdot t_{\mathrm{int}}} \tag{2}$$

where S is the signal measured by the sensor, S^{ds} is the dark signal, $L_{\mathrm{RASTA}}(\lambda_i)$ is the calibrated radiance of RASTA evaluated at the central wavelength of channel i, λ_i, and t_{int} is the integration time of the sensor. L_{RASTA} is resampled to the nominal resolution of the sensors listed in Table I, and using the center wavelengths determined in Section III-B7.

To transfer the calibration from the geometric center pixels to all geometric pixels of both instruments, the sensors are illuminated by the large integrating sphere, which provides homogeneous illumination for all pixels. The center pixel's calibration data is used to determine the spectral radiance of the integrating sphere using (1). The sphere's radiance is resampled to the center wavelengths of the channels of each pixel. It can then be substituted in (2) for L_{RASTA} to determine the radiometric response for all detector elements.

The radiometric response of each detector element can be factorized into the absolute response R_A and the relative response R_R according to

$$R_{i,j} = R_{A,i} \cdot R_{R,i,j} \tag{3}$$

where R_A is the spatial average of the radiometric response and therefore contains information about the spectrally dependent properties of the optics and the detector. R_R then describes the deviations from the average behavior, such as the photoresponse nonuniformity of each detector element, the vignetting of the optics, and inhomogeneities of the spectrometer slit, which also results in an inhomogeneous illumination of the detector array. R_R therefore assumes values around 1.

The integrating sphere is operated at its highest radiance setting, since this mode produces the most homogeneous radiance distribution. Since the radiance emitted by the large integrating sphere and RASTA then differ by more than an order of magnitude, the sensors are operated at different integration times for both measurements.

One thousand frames are recorded with each instrument and then averaged to a single frame to minimize the noise contribution. According to Section IV-C, the contribution of noise to the averaged frame is then below 1 DN.

3) Radiometric Noise: In the following, noise is defined as the standard deviation of a signal calculated from 1000 frames recorded during constant illumination conditions. The standard deviation is calculated for each pixel individually from the 1000 frames, so that uneven illumination of the detector array is not included in the determination of the sensor noise. For these measurements, the sensors are illuminated by the large integrating sphere. The stability of the sphere's output radiance is monitored by a highly stable Si radiometer.

Three noise types are considered to appear in the data: thermal dark current noise, which is caused by the nonzero temperature of the detector arrays, readout noise, which is the sum of electronic effects, and shot noise, which originates from the quantization of the light field into photons. The term "dark signal noise" designates the sum of thermal and readout noise. As for both sensors, the quantization noise originating from the A/D-conversion is much lower than the dark signal noise, it effectively does not contribute to the total sensor noise and will not be taken into consideration in the following.

To compare the noise properties of the three different binning modes of the sensor, the integration time for the measurement with $8\times$ binning is chosen so that the highest signal level is close to saturation. This integration time is then also used for the measurements with $4\times$ and $2\times$ binning.

4) Bad Pixels: Bad pixels are determined using uniform illumination of the detector array prior to the full assembly of the hyperspectral sensor. For the SWIR detector array, this was done by NEO, and for the VNIR detector array by Adimec.

According to these measurements, the VNIR sensor has two bad, nonadjacent subpixels. A subpixel is one of two detector elements that make up a $2\times$-binning pixel. The SWIR sensor has 102 bad pixels evenly distributed over the detector array.

To verify the existing bad pixels maps and to monitor changes, the following bad pixel measurements were performed. For

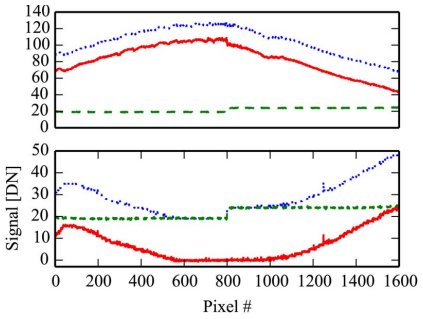

Fig. 2. Illustration of the radiometric discontinuity of the VNIR sensor around pixel 800. The sensor is illuminated with monochromatic laser light, so that light is measured only by a few neighboring channels. The dashed curves are the dark signal measurements performed automatically by the instrument, the dotted curves the raw data and the continuous curves are the dark signal-corrected raw data. In the upper graph, the illuminated channel is shown, and the discontinuity is visible. The lower graph shows the signal measured by an adjacent channel. As this channel measures almost no light, no discontinuity appears. The change in signal for geometric pixels over the entire detector array is caused by a combination of uneven illumination of the sensor's aperture, vignetting and smile.

this, the automatic bad pixel correction of the VNIR sensor is disabled.

Bad pixels are detector elements that significantly differ from the average pixel concerning signal, nonlinearity, or noise. The measurements are not as straightforward and extensive as the one performed by NEO, as a uniform illumination of the detector array is not achievable due to the assembled spectrometer optics. The light source used is the large integrating sphere, which is monitored for stability by the radiometer. For each data set, 1000 frames are recorded, and the averaged frames are compared. The criteria are chosen as follows.

1) Nonlinearity: Sphere measurements at two integration times are divided. Detector elements that differ more than $\pm 1\%$ from the ratio of the integration times are classified as bad. Only signals above 1000 DN for both integration times are used.
2) Noise: The standard deviation of the signal measured by each detector element is computed over the 1000 frames. The detector elements are classified as bad if they deviated by at least four standard deviations from the mean of the noise of the same channel.

5) Nonlinearity: According to an unpublished test protocol from Adimec, both VNIR detector halves exhibit nonlinearities for small signal up to signal levels on the order of 300 DN. This nonlinearity is slightly different for both halves. The measurements shown in Fig. 2 illustrate that this leads to discontinuities on the order of 5 DN–10 DN for low signal levels. As of this writing, this effect cannot be corrected during radiometric calibration.

For the SWIR sensor, no nonlinearity became apparent during our measurements. The bad pixel definition measurements of NEO include a more stringent test of nonlinearity of the sensor, which indicates that nonlinearities are not expressed to a noticeable degree in this sensor.

6) Polarization Sensitivity: The setup of this measurement consists of a rotation stage and a wire grid polarizer that are placed on top of the aperture of the small integrating sphere of the CHB [3]. The small integrating sphere of the CHB, which is equipped with QTH lamps as well, has an aperture of 4 cm $\times$ 20 cm, and provides higher radiance levels than the large sphere.

Due to the small size of the wire grid polarizer, not the entire FOV can be illuminated this way for sensor configurations with the FOV expanders. Hence, for these configurations, only the center parts are investigated for polarization sensitivity. Without the expanders, the entire FOV of the SWIR sensor is covered, and for the VNIR sensor, 100 geometric pixels are not covered on each side of the FOV. Since the integrating sphere is a "white" light source, the polarization properties of the sensors are measured for all channels simultaneously.

The polarizer is rotated in steps of 15° between 0° and 165°, and for each step, 1000 frames are recorded.

For each illuminated detector element, the polarization sensitivity is then determined by fitting a sine-squared curve to the series of signals $S(\phi)$ obtained during the measurement sequence. The fit function is

$$S_{i,j}(\phi) = A_{i,j} \cdot \sin^2(\phi + \phi_0) + O_{i,j} \tag{4}$$

with amplitude A, the rotation angle of the wire grid polarizer ϕ, the angular offset ϕ_0, and the signal offset, i.e., the average signal level, i.e., O. The fit function models Malus' law [14] for the transmission of linearly polarized light through a linear polarizer, depending on the angle between the light's polarization and the axis of the polarizer. The offset is required as the HySpex instruments behave as imperfect polarizers, and the angular offset is needed as the relative angle between the external polarizer and the effective polarizer of the sensor is not known.

The polarization sensitivity P is then defined as

$$P_{i,j} = \frac{A_{i,j}}{O_{i,j}} \cdot 100\%. \tag{5}$$

7) Spectral Properties: To determine the spectral properties of the imaging spectrometers, the spectral response functions (SRFs) of the spectral channels need to be characterized. The SRF of a channel changes in general over the FOV of the instrument, i.e., every single detector of the detector arrays has its individual SRF. Due to time constraints, these measurements are only feasible for a small subset of all detector elements. The SRFs of HySpex VNIR for the $4\times$- and $8\times$-binning modes are not measured separately, as they can be calculated as the sum of the SRFs for $2\times$ binning.

To measure the SRF, a collimated beam of nearly monochromatic light from a monochromator is used. The collimated beam is guided into the sensor's aperture by a movable and rotatable plane mirror that allows for the illumination of a selectable pixel. To guarantee that the sensor aperture and instantaneous FOV (IFOV) are completely overfilled, the beam cross section is larger than the aperture, and the beam divergence is larger than the sensor's IFOV. The monochromator has an absolute uncertainty of ± 0.1 nm for wavelengths below 1000 nm

and ± 0.2 nm for longer wavelengths. The spectral bandwidth is set to 0.65 nm for the measurement of the VNIR sensor and 1.2 nm for the measurement of the SWIR sensor. Simulations indicate that the chosen bandwidth of the monochromator has only very little influence on the measured bandwidths. For the measurement of the VNIR sensor's SRFs, the wavelength of the monochromator is scanned from 410 to 1010 nm in steps of 1 nm, and for the SWIR sensor, from 950 to 2550 nm in steps of 2 nm. For the VNIR sensor, the SRFs are measured at nine angles evenly distributed over its across-track FOV and seven angles for the SWIR sensor.

To determine the two relevant parameters of the SRF, i.e., the center wavelength and the bandwidth, a Gaussian function is fitted to the data measured for each channel. The center wavelength is then given by the center position of the Gaussian, and the bandwidth as the full-width at half-maximum (FWHM), as illustrated in Fig. 10. The spectral sampling interval (SSI), i.e., the average spectral distance between two neighboring channels, is determined by the gradient of a linear fit to the center wavelengths of the channels of the center pixel. Since both imaging spectrometers use a grating for spectral separation, the relationship between center wavelength and channel number is expected to be linear.

The result of these measurements are the Gaussian parameters of the SRFs of all channels of a few geometric pixels. The spectral properties of all detector elements are inferred by fitting the center wavelengths and bandwidths with a second-order polynomial. This procedure assumes that the properties of the optical system do not vary rapidly on the scale of the detector array. This assumption holds for the HySpex imaging spectrometers, and this approach was validated in [15].

As the sensor's telescope and the spectrometer are separated by the spectrometer slit, the FOV expander should not influence the results of the SRF measurements. This assumption was validated for each sensor for the three channels. Thus, the measurements are performed only without the FOV expander.

The smile is computed here as the difference between the center wavelength of each channel and the center wavelength of the same channel of the center pixel.

The measurement setup is described in more detail in [3] and details about the data analysis and a validation of the approach can be found in [15].

8) Geometric Properties: The information about the geometric properties of the sensors is contained in the across- and along-track line spread functions (LSFs), in particular, the viewing angles and the angular resolution.

The measurement setup consists of a narrow slit with a width of 0.05 mm, illuminated by a QTH lamp and positioned at the focal plane of a reflective collimator with a focal length of 750 mm. This results in a collimated beam with a divergence of 0.07 mrad that is guided via a folding mirror onto the sensor's aperture. Through linear movement and rotation of the folding mirror, different sensor pixels can be illuminated. The collimated beam is large enough to overfill the sensor's aperture.

The across-track LSFs are measured by using a slit that is imaged perpendicularly to the spectrometer slit of the sensor. The angular scan for the selected pixels is accomplished by changing the illumination angle via the folding mirror in increments of 0.07 mrad over a range of 3.5 mrad for the VNIR sensor measurement. For the measurement of the SWIR sensor, the scan is performed over 7 mrad in increments of 0.35 mrad.

The along-track LSFs are measured by using a slit that is imaged parallel to the spectrometer slit of the sensor. A linear translation of the illuminated slit is approximated by a rotation of the wheel the slit is mounted on, which results in a change in the incidence angle of the collimated beam on the sensor's aperture. For the measurement of the selected pixels of the VNIR sensor, the along-track LSF is scanned over a range of 3 mrad in increments of 0.15 mrad, and for the SWIR sensor over a range of 4.6 mrad in increments of 0.23 mrad.

Both along- and across-track LSFs are measured at 18 angles that are evenly distributed over the FOVs of the instruments. To retrieve the viewing angles and angular resolutions from the measurements, Gaussian functions are fitted to the data, the viewing angle being the center of the Gaussian, and the angular resolution being defined as its FWHM. The geometric properties of the detector elements that are not measured directly are inferred by fitting the viewing angles and angular resolution in between the measured pixels. For the fit of the along track values, a second-order polynomial is chosen, and for the across-track values, a fourth-order polynomial is taken. The order of the polynomial functions is selected so that higher order polynomials do not reduce the residuals any further. The keystone is computed here for each pixel as the largest difference in across-track viewing angles across the channels of that pixel.

The measurement setup and data analysis method are described in more detail in [3], [15].

9) Temporal Stability: The radiometric responses, the SRFs and the LSFs are meaningful parameters for monitoring the instrument's conditions, as the degradation of the optical surfaces or the detector arrays and misalignments lead to changes in these functions.

Most measurements presented in this report were performed during spring and autumn of 2012. To analyze potential changes, a representative set of measurements was repeated in spring 2013:

- The radiometric responses are measured again and compared with those measured previously.
- The validity of the spectral calibration is checked by illuminating it with monochromatic light at three different wavelengths, and by comparing the position of the monochromatic light on the detector array with the expected positions according to the wavelength maps. The center position of the monochromatic light is determined by fitting a Gaussian to the spectrum acquired by each geometric pixel.
- The validity of the geometric calibration is checked by comparing the across-track angular resolutions of all channels at three angular positions.

IV. Results

A. Dark Signal

For the VNIR sensor, the dark signal is of 24.0 ± 0.3 DN on one-half of the detector array, and 19.1 ± 0.3 DN for the

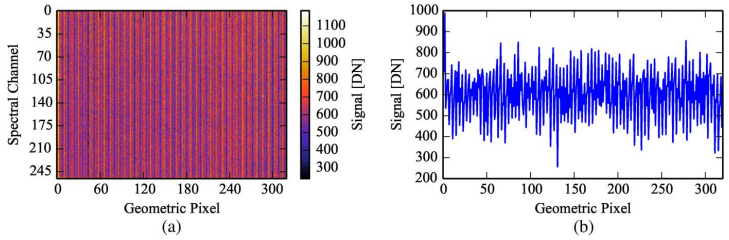

Fig. 3. (a) Averaged dark signal frame of the SWIR sensor at 1-ms integration time. (b) Dark signal of the SWIR sensor at 1-ms integration time for all geometric pixels of channel 100.

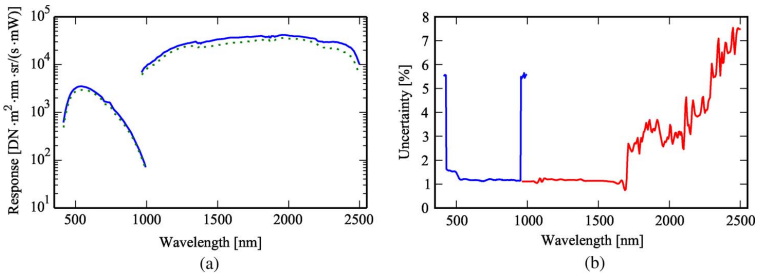

Fig. 4. (a) Averaged absolute radiometric responses for VNIR and SWIR sensors. The dotted lines show the responses for the sensors with the FOV expanders, the continuous lines the responses for the sensors without the FOV expanders. (b) Uncertainties of the radiometric responses for the center pixels of both HySpex sensors without FOV expander for a coverage factor of $k = 1$.

other half. These values are independent of integration time, and no repetitive patterns are apparent. The differences in the dark signals of a detector element in two consecutive dark signal frames are always smaller than 2 DN, and the standard deviation of the pixel-wise difference of dark signals is of 0.3 DN.

For the SWIR sensor, the dark signal frame exhibits a repetitive pattern, as shown in Fig. 3. The dark signal, averaged over the detector array, approximately increases linearly with integration time from 612 $\pm$ 125 DN at 1-ms integration time to 3014 $\pm$ 145 DN at 12 ms, thus reducing the available radiometric dynamic range. Note that the radiometric quantization of the SWIR sensor (14 bit) is higher than the quantization of the VNIR sensor (12 bit).

The differences in the dark signals of a detector element in two consecutive dark signal frames are always smaller than 20 DN, and the standard deviation of the pixel-wise difference of dark signals are of $\sim$1 DN. This also indicates that the dark signal pattern is fixed. Additionally, averaged over the entire detector array, drifts of 1 DN to 2 DN are seen.

For both HySpex sensors, the changes in the dark signal on the time scales occurring in data acquisitions are much smaller than the radiometric noise, except for a few outliers. Thus, the dark current correction scheme is adequate.

B. Radiometric Response

To visualize the absolute radiometric response R_A, the averages of the radiometric response matrix along the spatial axes of the detector arrays are shown in Fig. 4. The uncertainties to the radiometric responses, which take into account the uncertainties of the radiometric calibration of RASTA as determined by PTB, the inhomogeneity of the large integrating sphere, the pointing errors with respect to RASTA, the sensor noise, and the nonlinearity of the VNIR sensor. This nonlinearity is assumed to introduce an additional 5% of measurement uncertainty for signals lower than 300 DN. The total uncertainties are shown in Fig. 4(b) for a coverage factor of $k = 1$ [16]. Note that the radiometric response of the SWIR sensor is heavily affected by the water vapor and CO_2 content of the air in the laboratory around 1300 and 1850 nm. This is not reflected in the shown uncertainties.

The relative radiometric responses R_R, i.e., the response divided by the absolute response, are shown in Fig. 5. The sensitivity of the VNIR sensor with the FOV expander declines rapidly for the outer $\sim$100 pixels on each side of the FOV by about 30%. This decline is not as pronounced without the FOV expander: the sensitivity is reduced in this case at most by 15% of the mean value. These changes in relative response are presumably caused by vignetting of the optics. The rapid changes in relative response introducing the vertical stripes in Fig. 5 can be explained by inhomogeneities of the spectrometer slit, since they affect all channels in a similar way.

The sensitivity of the SWIR sensor with the FOV expander changes only slowly over the FOV, from 120% of the average value to 70%. Without the FOV expander, this effect is less pronounced by a few percent. These changes in relative response are presumably caused by asymmetric vignetting of the optics.

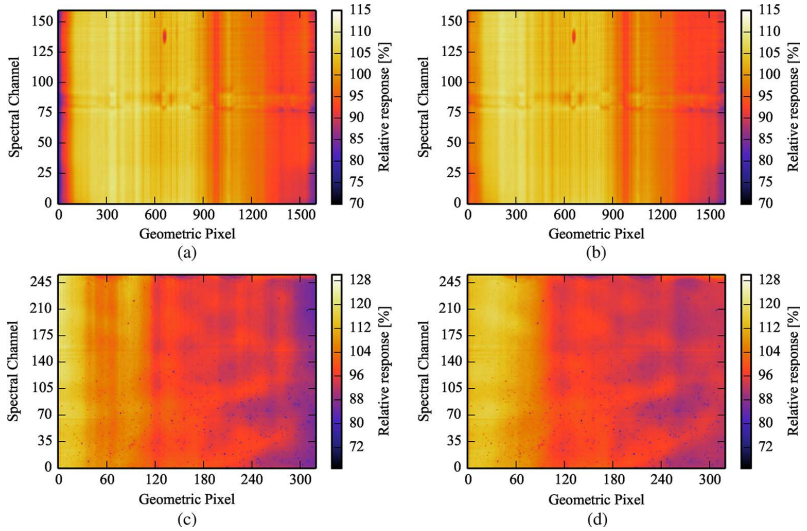

Fig. 5. Relative radiometric responses of both HySpex sensors. (a) VNIR with FOV expander. (b) VNIR. (c) SWIR with FOV expander. (d) SWIR.

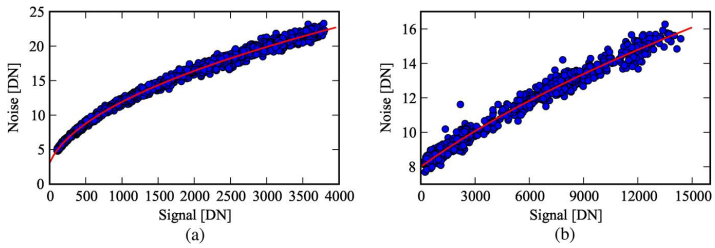

Fig. 6. (Circles) Measured noise for given signal levels for the respective sensor for every 99th detector element. (Continuous line) Fit of square root function to the data. (a) VNIR. (b) SWIR.

C. Radiometric Noise

For the VNIR sensor in the 2×-binning mode, the dark signal-noise level is on the order of 3 DN and does not increase noticeably with integration time, indicating that the thermal noise is very low and that the dark signal noise originates primarily from the readout process.

Fig. 6(a) shows the noise derived for every 99th element of the detector array from an illumination with the integrating sphere as light source, as well as a fit of a square root function to the data. The noise σ follows the function

$$\sigma(S) = 0.35 \cdot \sqrt{S + 51.4} + 0.56 \text{ [DN]} \tag{6}$$

with S the signal of a detector element.

The noise distributions for the higher binning modes are as expected: Hardware binning has only the potential to reduce the dark signal-noise level. Since it is already low, the total noise level is only reduced by 1 DN to 2 DN in the higher binning modes, as compared with software binning.

For the SWIR sensor, the dark signal noise, averaged over the entire detector array, increases linearly, from 7.5 DN at 1 ms integration time to 9.5 DN at 12 ms integration time.

Fig. 6(b) shows the noise derived for every 99th element of the detector array from an illumination with the integrating sphere as light source, as well as a fit of a square root function to the data. The noise σ follows the function:

$$\sigma(S) = 0.12 \cdot \sqrt{S + 6298.8} - 1.63 \text{ [DN]}. \tag{7}$$

The noise-equivalent radiance caused by dark signal noise is shown in Fig. 7 for both sensors. It is calculated using the radiometric responses for the combination of the instruments with the FOV expanders and integration times of 5 ms (VNIR) and 7 ms (SWIR), which are typical in-flight integration times. To facilitate comparisons, the radiance of asphalt road, as measured by the HySpex sensors from an aircraft, is also included, as well as its reflectance spectrum, retrieved after atmospheric correction. Since the dark signal noise is largely independent of integration time, whereas the signal is proportional to the

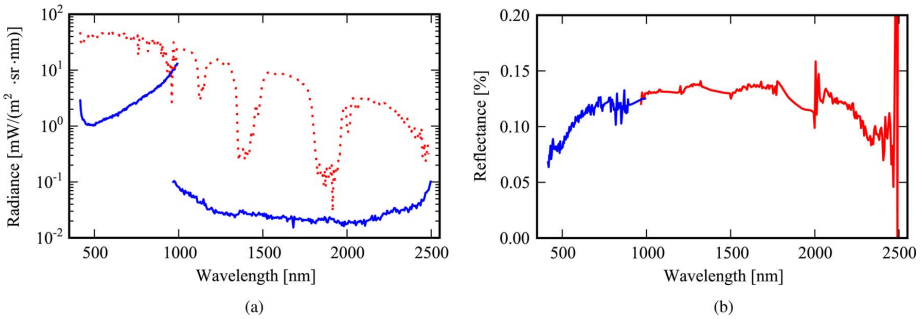

Fig. 7. (a) Dark signal-noise equivalent spectral radiance for both sensors (continuous lines, for the radiometric responses with FOV expanders), and at-sensor radiance of an asphalt road (dotted line; from an airborne measurement) for comparison. (b) shows the reflectance of the road as determined by the airborne measurement through atmospheric correction.

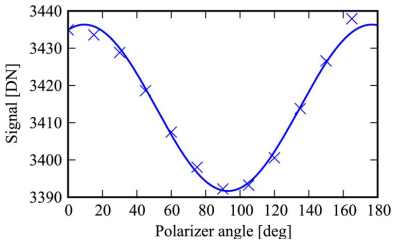

Fig. 8. Fit of (4) (continuous line) to the data (crosses) measured by a single detector element (pixel 700, channel 50) during the polarization measurement.

integration time, the signal-to-noise ratio (SNR) is approximately proportional to the integration time.

D. Bad Pixels and Linearity

Both bad pixel criteria provide satisfactory results: After the bad pixel correction performed prior to data acquisition by the camera itself, no additional bad pixels are found for the HySpex VNIR and 28 for the SWIR. The SWIR bad pixels are a subset of the NEO-defined bad pixels.

The linearity measurements show that for high signal levels, both detectors have linear radiometric responses. For low signal levels, the HySpex VNIR experiences nonlinearities on the order of 5%, according to the manufacturer of the detector hardware.

E. Polarization Sensitivity

The result of the polarization measurement of a single pixel and a fit of (4) to the data is shown in Fig. 8.

Fig. 9 shows the spatial averages of the sensitivity as a function of the channel number. The highest sensitivities for the VNIR sensor are observed at short wavelengths in the first 20 channels and are, on average, on the order of 10%, and below 4% for all channels above channel 20. For the SWIR sensor, the highest sensitivities are again on the order of 10%. The polarization sensitivity varies over the FOV by up to 50% toward the edges for the measurements without FOV expander.

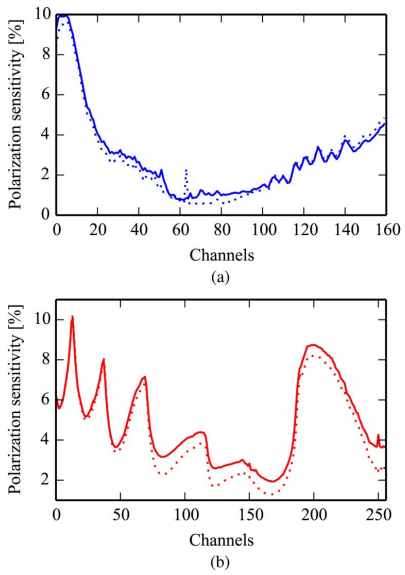

Fig. 9. Results of the polarization sensitivity measurements. The dotted lines show the results with the FOV expanders, and the continuous lines without the FOV expanders. (a) VNIR. (b) SWIR.

The differences shown in Fig. 9 are caused by the different optical elements built into the sensors, and the lenses and their coatings that compose the FOV expanders appear to introduce only small additional effects.

F. Spectral Properties

Most SRF can be reasonably approximated by Gaussian functions, as illustrated in Fig. 10 (left) for typical measurements. The largest fitting uncertainties, derived from the covariance matrix resulting from the fitting procedure, for the parameters wavelength and bandwidth of the Gaussian are on the order of 0.1 nm. According to NEO, for both sensors,

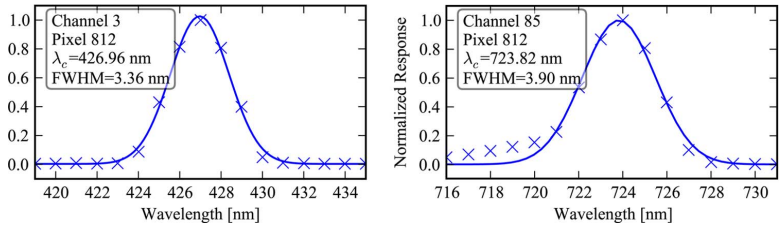

Fig. 10. (Left) SRFs for channel 3 and (right) channel 85 for the pixel 812 of the VNIR sensor. The crosses are the measurements, and the curves are Gaussian functions fitted to these data points. The uncertainties in the signal level are below 2%.

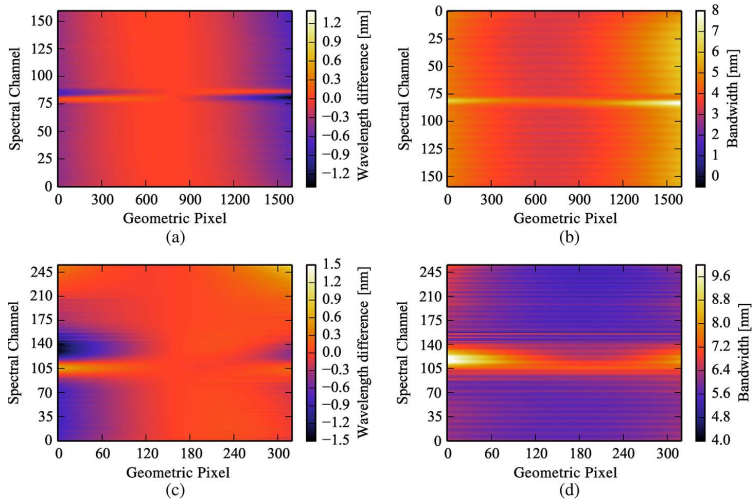

Fig. 11. Results of the spectral measurements. (a) and (c) show the difference of the center wavelength of each channel to the nadir pixel. (b) and (d) show the spectral bandwidth (FWHM). (a) VNIR. (b) VNIR. (c) SWIR. (d) SWIR.

half of the detector array is covered with an order-blocking filter that suppresses light diffracted at higher orders from the optical grating. The edge of these filters causes the SRFs to change their shapes [see Fig. 10 (right)]. This effect, and the fact that these SRFs are asymmetric and not well modeled by Gaussian functions, causes the retrieved center wavelengths and bandwidths to significantly vary in the center region of the detector (see Fig. 11). For the VNIR sensor, approximately the channels 75 to 90 (∼690 nm–745 nm) are affected, and for the SWIR sensor, the channels 90 to 140 (∼1500–1800 nm).

For the VNIR sensor, the SSI is 3.6 ± 0.1 nm, except for the channels disturbed by the edge of the order-blocking filter, where it deviates by up to 0.3 nm from the linear regression line fitted to the center wavelengths. For the SWIR, the SSI is 6.0 ± 0.2 nm, and the deviations from the regression line for the channels disturbed by the edge of the order-blocking filter are of ±0.5 nm.

Fig. 11(a) and (c) illustrates the smile distortion. For the VNIR sensor, the magnitude of the smile is between 0.4 and 0.7 nm, or 0.11 to 0.19 SSI outside the region affected by the filter. For the undisturbed channels of the SWIR sensor, the magnitude of the smile is on the order of 0.8 nm or about 0.13 SSI. Note that the sign of the smile curve changes between the bottom half and the top half of the SWIR detector array.

TABLE II
SUMMARY OF THE SPECTRAL PROPERTIES OF BOTH HYSPEX SENSORS. UNCERTAINTIES ARE GIVEN IN THE TEXT

	VNIR	SWIR
Center wavelength (first channel, center pixel) (nm)	416.3	968.5
SSI (nm)	3.6	6.0
Min/max bandwidth (nm)	3.5 – 6.0	5.6 – 7.0
Smile (SSI)	0.11 – 0.19	0.13

Fig. 11(b) and (d) shows the spectral bandwidth of each detector element. It is about 3.5 nm at the center of the detector array for the VNIR sensor, and degrades to close to 6.0 nm at the edges of the detector array. For the SWIR sensor, the bandwidth is about 5.6 nm at the center of the detector array, and increases up to 7.0 nm at the edges of the array, again without including the region influenced by the edge of the optical filter.

The sinusoidal features in the plots of Fig. 11 are probably caused by the drive of the grating turret of the monochromator and are below the wavelength uncertainty of the monochromator.

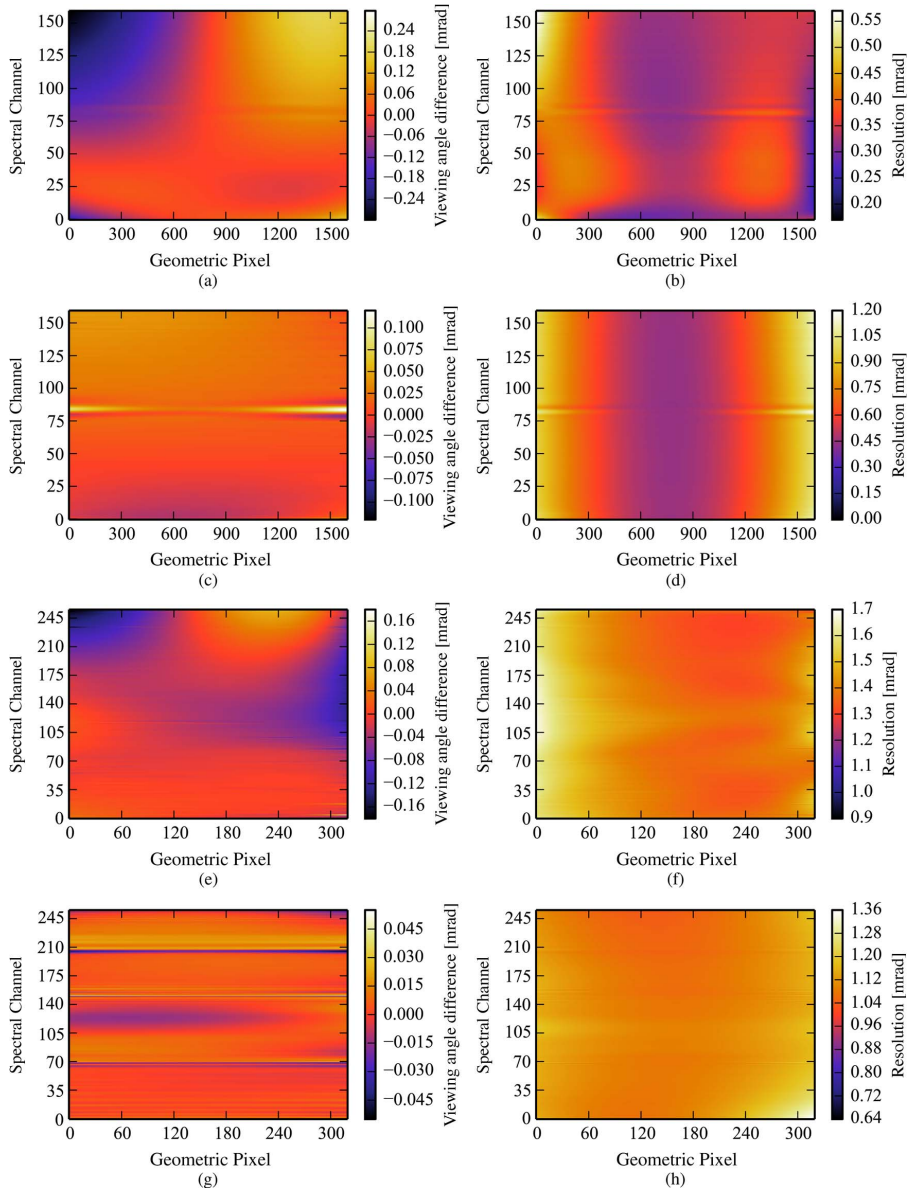

Fig. 12. Results of the geometric measurements for both sensors with the FOV expanders. (a), (c), (e), and (g) show the difference of the viewing angle of each pixel to those of channel 40. (b), (d), (f), and (h) show the angular resolution (FWHM). (a) VNIR: Across track. (b) VNIR: Across track. (c) VNIR: Along track. (d) VNIR: Along track. (e) SWIR: Across track. (f) SWIR: Across track. (g) SWIR: Along track. (h) SWIR: Along track.

The main spectral properties of the sensors are summarized in Table II.

G. Geometric Properties

For all measurements, Gaussian functions reproduce the shape of the LSFs well, with the exception of the detector elements close to the edge of the order-blocking filter. The results are shown in Figs. 12 and 13. Figs. 12(a), (c), (e), (g) and 13(a), (c), (e), (g) show the differences to the viewing angle of channel 40 to highlight the deviation from perfect pointing, i.e., keystone distortion. Channel 40 is chosen for both sensors because it is outside the channel range affected by the edge of the optical filter. The largest uncertainties in the

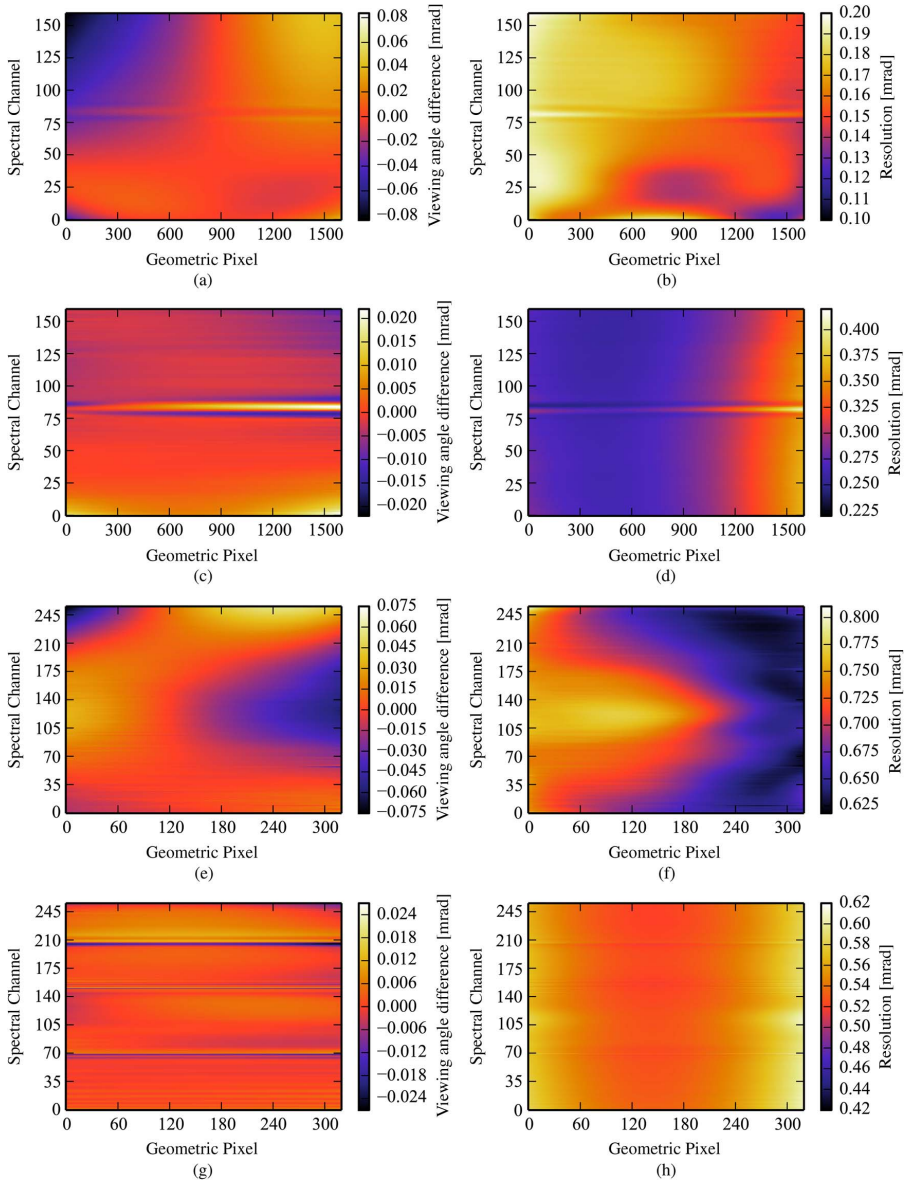

Fig. 13. Results of the geometric measurements for both sensors without the FOV expanders. (a), (c), (e), and (g) show the difference of the viewing angle of each pixel to those of channel 40. (b), (d), (f), and (h) show the angular resolution (FWHM). (a) VNIR: Across track. (b) VNIR: Across track. (c) VNIR: Along track. (d) VNIR: Along track. (e) SWIR: Across track. (f) SWIR: Across track. (g) SWIR: Along track. (h) SWIR: Along track.

fitting procedure for the parameters of the Gaussian functions are below 2%. For both SWIR and VNIR sensors, the changes in along-track viewing angles shown in Figs. 12(c), (g) and 13(c), (g) are on the order of one-tenth of the along-track IFOVs of the respective sensors, and on the order of the resolution of the measurement setup. The figures are included for the sake of completeness. Summaries of the main geometric properties of the sensors are given in Tables III and IV.

H. *Temporal Stability*

All changes in radiometric responses, the center wavelengths and geometric angular resolution are below the given measurement uncertainties.

V. Calibration Software

To be able to use our detailed knowledge of the instrument for the calibration and correction of airborne data, we

TABLE III
SUMMARY OF THE GEOMETRIC PROPERTIES OF THE HYSPEX VNIR SENSOR, WITH AND WITHOUT THE FOV EXPANDER. ASI DENOTES THE ANGULAR SAMPLING INTERVAL

	1×FOV	2×FOV
Total FOV	16.7°	34.5°
Avg. across-track ASI (mrad)	0.18	0.37
Avg. across-track IFOV (mrad)	0.16	0.36
Min/max across-track IFOV (mrad)	0.13 – 0.20	0.28 – 0.56
Min/max along-track IFOV (mrad)	0.25 – 0.40	0.50 – 1.1
Avg./max keystone (ASI)	0.22/0.50	0.46/0.84

TABLE IV
SUMMARY OF THE GEOMETRIC PROPERTIES OF THE HYSPEX SWIR SENSOR, WITH AND WITHOUT THE FOV EXPANDER

	1×FOV	2×FOV
Total FOV	13.2°	27.2°
Avg. across-track ASI (mrad)	0.72	1.49
Avg. across-track IFOV (mrad)	0.79	1.36
Min/max across-track IFOV (mrad)	0.62 – 0.81	1.30 – 1.43
Min/max along-track IFOV (mrad)	0.52 – 0.61	1.04 – 1.36
Avg./max keystone (ASI)	0.09	0.17

developed our own software tool that performs level 0 to level 1 calibration, i.e., the conversion from sensor units into physical units and the removal of measurement artifacts generated by the sensors. This tool implements the calibration procedure described in Section III-A and is written in Python, relying on the NumPy and SciPy packages.

The calibrated scene is saved as a band interleave line file together with an ENVI header file, that contains additional information, such as a list with the center wavelength of each channel of the nadir pixel. Two output formats are supported: either the calibrated radiance data can be saved in 4 bytes floating point values, or, in order to save hard disk space, in 2 bytes unsigned integer values. In case the data is saved as integers, the calibrated radiance data is scaled so that it spans the entire number range given by unsigned integers to minimize the loss of radiometric resolution due to the reduction in numerical precision. Small negative radiances that can occur via the dark signal correction are set to zero, and the scaling factor is then simply defined as $F_{\text{scale}} = (2^{16} - 2)/L_{\max}$, where $L_{\max}$ is the highest measured unsaturated radiance in the scene. The highest unsaturated value is scaled to a value of 65 534, and saturated data is set to a numerical value of 63 535.

VI. DISCUSSION

This supplemental characterization provides a lot more information about both HySpex instruments, which will be discussed in the following.

To highlight two issues in the radiometric calibration of the VNIR sensor, a data set from the airborne data acquisition of a lake is shown in Fig. 14. The data set is calibrated using the

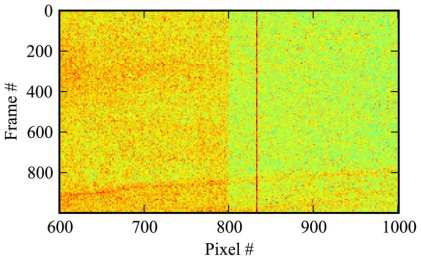

Fig. 14. Calibrated airborne image of open water, acquired with the HySpex VNIR, averaged over the channels 3 to 6. Two effects are apparent in this image: a stripe at pixel 833, and a sudden change in signal level at the center of the detector array.

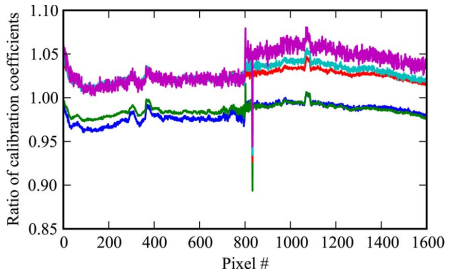

Fig. 15. Ratio of the relative radiometric responses of the VNIR sensor, as measured by NEO and DLR, for different channels.

radiometric response provided by NEO. To illustrate the issues clearly, the image shows an average of the channels 3 to 6, i.e., channels measuring the "blue part" of the spectrum, which record only a low signal on the order of 100 DN.

The first issue is that the originally provided responses lead to images with one conspicuous stripe. Fig. 15 shows the ratio of the relative radiometric responses as determined by NEO and by DLR in the CHB. Since the dip is at the same spatial position as the stripe in the airborne image, this shows that the stripe originates from an erroneous relative radiometric response. This effect could be explained with a speck of dust that stuck to the imaging spectrometer slit during calibration at NEO and that "fell off" afterward. The second issue appearing in this image, i.e., the abrupt change in radiance at the center of the image, although the recorded surface is almost homogeneous, is caused by the difference in nonlinear behavior between the two logical halves of the VNIR sensor's detector array. We intend to develop a correction algorithm for this issue, as linearity is required particularly to measure stray light at an accuracy that allows for correction.

Differences in the absolute radiometric responses as determined by NEO and DLR are shown in Fig. 16. For the SWIR sensor, significant differences occur due to atmospheric absorption features around 1300 nm and around 1850 nm. Since for the same absorption features, the atmosphere is opaque at these wavelengths; this has no consequences for airborne remote sensing. This issue may be further pursued for laboratory applications of the HySpex sensors. Larger differences ($> 30\%$)

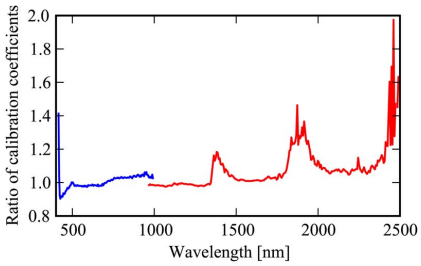

Fig. 16. Ratio of the absolute radiometric responses, as measured by NEO and DLR, for the center pixels of both instruments.

between both responses occur for the first 100 nm and last 100 nm of the spectral range. For the differences between 2400 nm and 2500 nm, the uncertainties involved in the generation of the radiometric responses are high due to the calibration uncertainties of both the radiometric standards of NEO and DLR. For the differences in the blue part of the spectrum, the exact source of the discrepancy is yet unclear.

Using the knowledge of the radiometric noise, see Section IV-C, and the absolute radiometric response, SNRs can be predicted for specific applications using the expected at-sensor-radiances. As can be seen in Fig. 6(a), the VNIR sensor is effectively shot noise limited for signal levels $>$ 300 DN, as the radiometric noise is then at least twice as big as the background signal noise. Since the background signal noise of the VNIR sensor is very low and independent of the integration time, the advantage in achievable SNRs of hardware binning over software binning is negligible, and the SNR is inversely proportional to the integration time. Hardware binning is therefore mainly useful to allow for shorter integration times and to reduce data size. For the SWIR sensor, the background signal-noise level is of similar magnitude as the shot noise, while still yielding low noise levels. The background signal level increases quickly with integration time, limiting the radiometric dynamic range. For example, for integration times of 5 ms, the dynamic range is reduced by about 10%.

The polarization sensitivity determined in Section IV-E is essential for the indication of measurement uncertainties for at-sensor radiances and complements the calibration uncertainties shown in Fig. 4(b).

The measurements with the assembled spectrometers were not adequate to provide us with complete bad pixel data, see Section IV-D. Thus, we will use the bad pixel maps provided by the manufacturers, and will monitor deterioration via the radiometric responses.

The extensive characterization of the spectral and geometric responses of the sensors, see Section IV-F and G, has the benefit that the optical distortions smile and keystone can be corrected [12], as a center wavelength and a relative viewing angle can be assigned to each detector element. This is more important for the VNIR sensor, which exhibits smile on the order of up to 0.2 SSI, and a keystone of 0.5 pixels with the FOV expander. The optical distortions of the SWIR sensor are lower, with smile and keystone on the order of 0.1 SSI and pixels, respectively. Likewise, the information that the bandwidths of the channels vary over the FOV of the instruments and that the SRFs of the channels close to the center of the detector array depart from purely Gaussian behavior, could be used to provide a more uniform data product in the future.

Finally, it could be observed that during the 1.5 years of ownership and operation of the instrument, the original alignment still appears to be unchanged at laboratory conditions.

VII. Conclusion

This paper has presented, to the authors' best knowledge, the first independent characterization and calibration of NEO imaging spectrometers for scientific use in remote sensing. Through the traceable spectral and radiometric calibration of the data, information on the uncertainties involved in the measurement process [17], [18] can now be provided. This is necessary to perform valid measurements [16] and allows potential users to ascertain the usability of the data from these sensors for their use cases. Further, the indication of measurement uncertainties is crucial for the comparison of different data sets. The traceable radiometric calibration is also a prerequisite for quantitative data analysis methods that are based on absolute at-sensor radiances and unbiased reflectances [20], including atmosphere correction [19].

Given that the HySpex sensors will be used for a variety of remote sensing applications [20], including the remote sensing of water bodies, which require very low calibration uncertainties [21], it is essential that the data is as free as possible from systematic errors and that the properties of the sensors are well known. Ideally, the characterization efforts on the airborne sensors should be as extensive as those for spaceborne missions, as otherwise airborne-sensor-specific effects might lead to inconsistencies to data products derived from spaceborne data, e.g., through validation measurements.

The detailed measurements presented here allowed for several improvements to the calibration of our HySpex sensors. Notably, the impact of several systematic error sources was reduced, in particular the striping for the HySpex VNIR, and the optical distortions keystone and smile.

Finally, this publication may be useful to scientists looking to purchase their own hyperspectral imager, as detailed characterization information about current-generation commercial hyperspectral sensors is scarce.

The next measurements will focus on the nonlinearity of the VNIR sensor, on stray light in the spectrometer, on monitoring long term changes, the determination of the stability of the instruments under airborne operating conditions, and to atmospherically correct the radiometric calibration measurements in the laboratory.

Acknowledgment

The authors would like to thank Norsk Elektro Optikk A/S and particularly T. Løke for always quickly and satisfyingly answering all of our questions and requests. The authors also thank P. Gege for his significant help in reviewing and improving this manuscript, as well as the editor and reviewers for their time and comments.

REFERENCES

[1] Norsk Elektro Optikk, Web site of Norsk Elektro Optikk, Dec. 2013. [Online]. Available: http://www.neo.no/

[2] H. Kaufmann *et al.*, "EnMAP: A hyperspectral sensor for environmental mapping and analysis," in *Proc. IEEE IGARSS*, Denver, CO, USA, 2006, pp. 1617–1619.

[3] P. Gege *et al.*, "Calibration facility for airborne imaging spectrometers," *ISPRS J. Photogramm. Remote Sens.*, vol. 64, no. 4, pp. 387–397, Jul. 2009.

[4] M. Jehle *et al.*, "APEX—Current status, performance and validation concept," in *Proc. IEEE Sensors*, Waikoloa, HI, USA, 2010, pp. 533–537.

[5] N. Oppelt and W. Mauser, "The airborne visible/infrared imaging spectrometer AVIS: Design, characterization and calibration," *Sensors*, vol. 7, no. 9, pp. 1934–1953, Sep. 2007.

[6] R. L. Lucke *et al.*, "Hyperspectral imager for the coastal ocean: Instrument description and first images," *Appl. Opt.*, vol. 50, no. 11, pp. 1501–1516, Apr. 2011.

[7] C. Davis *et al.*, "Ocean PHILLS hyperspectral imager: Design, characterization, calibration," *Opt. Exp.*, vol. 10, no. 4, pp. 210–221, Feb. 2002.

[8] G. Filacchione *et al.*, "Calibration pipeline of VIS-NIR imaging spectrometers for planetary exploration: The ROSETTA VIRTIS-M case," in *Proc. WHISPERS*, Grenoble, France, 2009, pp. 1–5.

[9] Adimec, Adimec Website, Jun. 2014. [Online]. Available: http://www.adimec.com/

[10] SOFRADIR, SOFRADIR MARS SW Datasheet, Jun. 2014. [Online]. Available: http://nasa.olin.edu/projects/2010/tec/info/marsSw.pdf

[11] P. Mouroulis, R. O. Green, and T. G. Chrien, "Design of pushbroom imaging spectrometers for optimum recovery of spectroscopic and spatial information," *Appl. Opt.*, vol. 39, no. 13, pp. 2210–2220, May 2000.

[12] A. Fridman, G. Høye, and T. Løke, "Resampling in hyperspectral cameras as an alternative to correcting keystone in hardware, with focus on benefits for the optical design and data quality," in *Proc. SPIE 8706*, 2013, p. 870602.

[13] T. Schwarzmaier, A. Baumgartner, P. Gege, C. Köhler, and K. Lenhard, "DLR's new traceable radiance standard "RASTA"," in *Proc. IGARSS*, Munich, Germany, 2012, pp. 1–4.

[14] E. Hecht, *Optics*., 4th ed. San Francisco, CA, USA: Addison-Wesley, 2002.

[15] A. Baumgartner, P. Gege, K. Claas, K. Lenhard, and T. Schwarzmaier, "Characterisation methods for the hyperspectral sensor HySpex at DLR 's calibration home base," in *Proc. SPIE*, Edinburgh, U.K., 2012, pp. 1–8.

[16] Joint Committee for Guides in Metrology, JCGM 200: 2008 International Vocabulary of Metrology—Basic and General Concepts and Associated Terms (VIM) 2008.

[17] H. J. Kostkowski, *Reliable Spectroradiometry*. La Plata, MD, USA: Spectroradiometry Consulting, 1997.

[18] K. Lenhard, "Determination of combined measurement uncertainty via Monte Carlo analysis for the imaging spectrometer ROSIS.," *Appl. Opt.*, vol. 51, no. 18, pp. 4065–4072, Jun. 2012.

[19] R. Richter and D. Schlapfer, "Geo-atmospheric processing of airborne imaging spectrometry data. Part 2: Atmospheric/topographic correction," *Int. J. Remote Sens.*, vol. 23, no. 13, pp. 2631–2649, 2002.

[20] M. E. Schaepman *et al.*, "Earth system science related imaging spectroscopy-An assessment," *Remote Sens. Environ.*, vol. 113, pp. S123–S137, Sep. 2009.

[21] H. R. Gordon, "Atmospheric correction of ocean color imagery in the Earth Observing System era," *J. Geophys. Res.*, vol. 102, no. D14, pp. 17081–17106, Jul. 1997.

Karim Lenhard received the Diploma in physics from the University of Bonn, Bonn, Germany, in 2008. He is currently working toward the Ph.D. degree at the University of Zurich, Zurich, Switzerland, in 2012.

Since 2012, he has been a Researcher with the German Aerospace Center (DLR), Oberpfaffenhofen, Germany. At DLR, he is jointly responsible for operating and improving the calibration laboratory of DLR for imaging spectrometers. His research interests are the spectral and radiometric calibration of hyperspectral instruments, with a focus on stray light issues.

Andreas Baumgartner received the B.Eng. degree in mechatronics with focus on optical engineering and the M.Eng. degree in electrical engineering and information technology from the University of Applied Sciences Deggendorf, Deggendorf, Germany, in 2008 and 2010, respectively.

Since then, he has been working with the German Aerospace Agency (DLR), Oberpfaffenhofen, Germany, and is jointly responsible for the calibration laboratory of DLR for imaging spectrometers. His research interests are improving the setup, methods and software for the spectral, geometric, and radiometric calibration of imaging spectrometers.

Thomas Schwarzmaier received the Dipl.Ing. (FH) degree in mechanical engineering from Munich University of Applied Sciences, Munich, Germany, in 2010.

Since then, he has been working with the German Aerospace Agency (DLR), Oberpfaffenhofen, Germany, and is responsible for an optics laboratory for imaging spectrometers. His research interests are improving the setup, methods and software for the spectral, geometric, and radiometric calibration of imaging spectrometers.

Chapter 4

Impact of improved calibration of a NEO HySpex VNIR-1600 sensor on remote sensing of water depth

This chapter has been published as: Lenhard, K., Baumgartner, A., Gege, P., Nevas, S., Nowy, S., & Sperling, A. (2015). Impact of improved calibration of a NEO HySpex VNIR-1600 sensor on remote sensing of water depth. IEEE Transactions on Geoscience and Remote Sensing.

This article has been accepted for inclusion in a future issue of this journal. Content is final as presented, with the exception of pagination.

Impact of Improved Calibration of a NEO HySpex VNIR-1600 Sensor on Remote Sensing of Water Depth

Karim Lenhard, Andreas Baumgartner, Peter Gege, Saulius Nevas, Stefan Nowy, and Armin Sperling

***Abstract*—This paper investigates at the example of bathymetry how much an application can profit from comprehensive characterizations required for an improved calibration of data from a state-of-the-art commercial hyperspectral sensor. A NEO HySpex VNIR-1600 sensor is used for this paper, and the improvements are based on measurements of sensor properties not covered by the manufacturer, in particular, detector nonlinearity and stray light. This additional knowledge about the instrument is used to implement corrections for nonlinearity, stray light, spectral smile distortion and nonuniform spectral bandwidth and to base the radiometric calibration on a SI-traceable radiance standard. Bathymetry is retrieved from a data take from the lake Starnberg using WASI-2D. The results using the original and improved calibration procedures are compared with ground reference data, with an emphasis on the effect of stray-light correction. For our instrument, stray-light biases the detector response from 416–500 nm up to 8% and from 700–760 nm up to 5%. Stray-light-induced errors affect bathymetry mainly in water deeper than Secchi depth, whereas in shallower water, the dominant error source is the calibration accuracy of the light source used for radiometric calibration. Stray-light correction reduced the systematic error of water depth by 19% from Secchi depth to three times Secchi depth, whereas the relative standard deviation remained stable at 5%.**

***Index Terms*—Bathymetry, calibration, hyperspectral, imaging spectrometer, nonlinearity, remote sensing, stray light.**

I. Introduction

OPERATIONAL reliability, provided data quality, and achievable calibration uncertainties of commercial hyperspectral sensors are nowadays on a high level, making these instruments a valuable tool for many applications [1]. Nevertheless, improvements in calibration are for most sensors possible since the manufacturers' procedures rarely account for all sensor properties. The calibration of a NEO HySpex VNIR-1600 sensor described in [2] is complemented here by corrections for the stray light inside the spectrometer, and for a radiometric nonlinearity introduced by the read-out electronics. The measurements enabling these corrections are presented. Such refinements of calibration are time consuming, whereas the benefits for a specific application are usually unknown. The goal of this paper is to explore the potential for improvements to calibration and their impacts on a remote sensing data product, water depth, using data from the HySpex VNIR-1600 sensor for illustration.

If the laboratory measurements used for calibration do not cover all sensor properties, a calibrated hyperspectral image can be affected by systematic errors of unknown magnitude. Since errors of spectral radiance lead to errors of the derived products, the analysis of a parameter with a large and well-known gradient can help to identify systematic calibration errors and to quantify their influence on the accuracy of that parameter. An application of remote sensing to water bodies is chosen, as calibration issues are highlighted here due to the nature of the signal. First, most of the recorded signal stems from the atmospheric path radiance, which results in at-sensor-radiances, are very different from those used for the calibration. That is, airborne at-sensor-radiances have their maximum in the blue part of the spectrum, instead of the near-infrared in the laboratory. Second, as the signal from the water body is much smaller than the one originating from the atmosphere, calibration issues can easily result in failures of the atmospheric correction, which then lead to large errors of the water leaving radiance.

Water depth, which was selected as a higher level test parameter since it changes gradually over large ranges, is stable for long time and can be measured accurately during field campaigns. Furthermore, accurate radiative transfer models exist, which allow to simulate the radiance and reflectance of shallow waters as a function of all relevant environmental parameters [3]–[5], and image processing software based on these physical models has been developed to process hyperspectral data of shallow waters [6]–[8]. In this paper, the software WASI-2D [8] is used to derive water depth of each image pixel. Its error is studied for different calibration procedures of a HySpex VNIR-1600 sensor by comparison with echo-sounding measurements.

Manuscript received February 10, 2015; revised April 28, 2015; accepted May 4, 2015. This work was supported in part by the European Metrology Research Programme (EMRP) within the joint research project Metrology for Earth Observation and Climate (MetEOC). The EMRP is jointly funded by the EMRP participating countries within EURAMET and the European Union.

K. Lenhard, A. Baumgartner, and P. Gege are with the Deutsches Zentrum für Luft- und Raumfahrt (DLR), Institut für Methodik der Fernerkundung (IMF), 82234 Oberpfaffenhofen, Germany (e-mail: karim.lenhard@dlr.de; andreas.baumgartner@dlr.de; peter.gege@dlr.de).

S. Nevas and A. Sperling are with the Physikalisch-Technische Bundesanstalt (PTB), 38116 Braunschweig, Germany (e-mail: saulius.nevas@ptb.de; armin.sperling@ptb.de).

S. Nowy was with Physikalisch-Technische Bundesanstalt (PTB), 38116 Braunschweig, Germany. He is now with Gigahertz-Optik, 82299 Türkenfeld, Germany (e-mail: s.nowy@gigahertz-optik.com).

Color versions of one or more of the figures in this paper are available online at http://ieeexplore.ieee.org.

Digital Object Identifier 10.1109/TGRS.2015.2431743

This article has been accepted for inclusion in a future issue of this journal. Content is final as presented, with the exception of pagination.

TABLE I
PROPERTIES OF THE HYSPEX VNIR-1600 CAMERA WITH FOV EXPANDER. SPECTRAL BANDWIDTH AND IFOVS ARE GIVEN FOR THE CENTER OF THE FOV; THEY DEGRADE TOWARD THE EDGES

	HySpex VNIR-1600
Detector technology	Si CCD
Spectral range	416 - 992 nm
Spectral sampling interval	3.6 nm
Spectral bandwidth	3.5 nm
FOV	34.5°
IFOV (across track)	0.37 mrad
IFOV (along track)	0.50 mrad
Pixels / line	1600
Channels	160
Radiometric quantization	12 bit

HySpex VNIR-1600 is a commercial hyperspectral camera manufactured by the company Norsk Elektro Optikk (NEO) [9]. The instrument used in this study was acquired by the German Aerospace Center (DLR) in 2011 for airborne campaigns and laboratory measurements. The basic sensor properties are listed in Table I. Additional information, including the standard calibration procedure by NEO, can be found in [2]. The characterization was mainly performed in DLR's calibration laboratory for airborne imaging spectrometers [Calibration Home Base (CHB)] [10], and the stray-light characterization was performed at Physikalisch-Technische Bundesanstalt (PTB, Germany's National Metrology Institute) using the pulsed laser for advanced characterization of spectroradiometers (PLACOS) setup [11] as a tuneable light source. For airborne data acquisition at DLR, the camera is usually equipped with a field-of-view (FOV) expander lens that approximately doubles its native FOV. As the stray-light measurements with PLACOS are very time consuming, it was only determined for the configuration with the FOV expander.

The amendments to the calibration procedure provided by NEO are the correction of a radiometric nonlinearity caused by the read-out electronics of the focal plane array (FPA), the correction of diffuse, in-band stray light, the correction of variations in the center wavelength of spectral channels (i.e., spectral smile) and the nonuniform spectral bandwidth over the FOV of the instrument, and the radiometric calibration with respect to a different radiance standard (RASTA). The radiometric, spectral, and geometric characterizations are described in detail in [2]. The former two will be briefly recapitulated in the following, with additional descriptions of the measurement of radiometric nonlinearity and stray light, including the correction algorithms.

In the following, the impact of three different calibration procedures on bathymetry derived from a calibrated image will be compared: the procedure with the calibration data set as provided by NEO, the calibration procedure described in [2], including the nonlinearity correction presented in Section IV-A2, and the latter extended by the spectral and spatial stray-light correction described in Section II-C.

II. SENSOR CHARACTERIZATION AND CALIBRATION

A. Spectral Response

To determine the spectral response function (SRF) of each channel, the sensor was illuminated with a collimated beam of spectrally narrow light generated by a monochromator that overfilled the instantaneous FOV (IFOV) of a single geometric pixel, and the monochromator wavelength was tuned across the channels' sensitive ranges. The SRF is the wavelength-dependent signal normalized to the maximum signal. The SRFs were measured for all channels at seven geometric pixels. The measurements revealed that most SRFs are well described by Gaussian functions. Thus, the channels' SRFs can be described accurately by an analytical equation with two parameters, center wavelength λ_i, and full-width at half-maximum (FWHM) $\Delta\lambda_i$, where i indicates the along-track pixel number.

To derive the center wavelengths λ_i of the channels of the geometric pixels for which no direct measurements are available, their variation as a function of pixel number i is described by a second-order polynomial. For the spectral bandwidths, a fourth-order polynomial was found to be suitable [2]. This interpolation step is necessary as a measurement for every FPA detector element would be too time consuming (i.e., on the order of months) to be practical. The assumption that SRFs are slowly changing was validated in [12] and is a typical characteristic of instruments of this design [13].

While the original NEO calibration assumes common center wavelengths and bandwidths for all pixels of one channel, the measurements at DLR have shown that these parameters change slightly across the FOV. This effect is corrected in the DLR calibration procedures by resampling the recorded spectra in two steps.

a) Resampling to a Common Spectral Bandwidth: To obtain identical spectral bandwidths for all pixels and channels, resampling of a radiometrically calibrated spectrum L is performed according to [14]

$$L_\mathrm{r} = \mathcal{F}^{-1}\left(\mathcal{F}(L)\cdot\frac{\mathcal{F}(I_\mathrm{T})}{\mathcal{F}(I_\mathrm{M})}\right) \tag{1}$$

where L_r is the resampled spectrum, $\mathcal{F}$ the Fourier transform, and I are the SRFs. I_M is the SRF derived from the measurements, and I_T the target SRF. Both SRFs are Gaussian functions, with the FWHM of I_T set to 5 nm for convenience.

This approach assumes that the shape of the SRFs is Gaussian for all channels, and that only the width is variable. According to [2], this is mostly the case, except for the channels 75 to 95, which have asymmetric SRFs. The approach is chosen as it is correct for the majority of detector elements and simplifies and shortens computations, as compared with the individual treatment of each SRF. The asymmetry of channels 75 to 95 is small; thus, it is a reasonable approximation even for these channels.

b) Resampling to a Common Wavelength Scale: To obtain identical center wavelengths for all geometrical pixels, the smile distortion [13] is corrected. For that, the recorded spectrum is resampled to a common set of center wavelengths using cubic spline interpolation. The center wavelength of the first

This article has been accepted for inclusion in a future issue of this journal. Content is final as presented, with the exception of pagination.

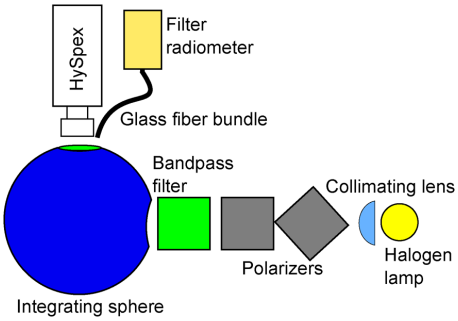

Fig. 1. Scheme of the setup for the nonlinearity measurements.

channel is set to 416 nm, and the spectral sampling interval is chosen as 3.600 nm, as compared with the spectral sampling interval given by NEO of 3.623 nm. The number of channels is preserved.

B. Nonlinearity

The camera of the HySpex VNIR-1600 sensor is an Adimec 1600m/D [15], which uses a Kodak KAI2020 FPA. Adimec provided the information that an electronic component in the read-out-circuit can cause nonlinearity with respect to the signal level. This nonlinear effect is introduced after the addition of the electronic offset, which constitutes most of the background signal [2]. Thus, determination and correction of nonlinear effects is done on background subtracted data.

Since the FPA has two similar read-out-circuits, one for the left half (pixel numbers < 800) and one for the right half (pixel numbers $\geq$ 800) of the detector array, and since all detector elements are treated equally within a read-out-circuit, only a single function describing the nonlinearity is required for each detector half, independently of channel and pixel number.

To measure the nonlinear behavior of the detector array and its read-out electronics, the setup shown in Fig. 1 was developed, which allows to precisely change the at-sensor radiance over three orders of magnitude. Light is coupled into the sensor using an integrating sphere. The sphere is illuminated by a quartz-tungsten halogen lamp. The light emitted by the lamp passes two linear polarizers and a bandpass filter centered around 530 nm with a bandwidth of $\approx$ 10 nm (FWHM). This setup illuminates a few channels of the HySpex instrument for a few hundred geometric pixels. The radiance can be varied in small steps by rotating one of the polarizers. In order not to change the polarization state of the light impinging the bandpass filter and entering the sphere, the polarizer close to the lamp is rotated. A highly stable Si radiometer (Gamma Scientific TIA-3000) monitors and records a signal proportional to the sphere's radiance. Its deviation from linearity is below 0.1% for the used signal range.

Linearity of the response is determined as a function of the signal by measuring both with the HySpex VNIR-1600 and the radiometer the sphere's output for different polarizer angles and varying integration times of HySpex. The data are extracted separately from both halves of the FPA from a single spectral channel and averaged for each detector half over 20 geometric pixels and 200 frames.

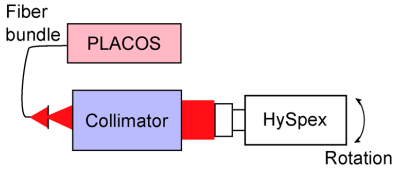

Fig. 2. Scheme of the stray-light measurement setup.

C. Stray Light

The measured imaging spectrometer signal S_{meas} consists of the properly imaged in-band signal S_{IB} and the stray light S_{SL} [16]

$$S_{\mathrm{meas}} = S_{\mathrm{IB}} + S_{\mathrm{SL}}. \tag{2}$$

The S are so-called image frames, i.e., matrices of data acquired by the instrument during a single data acquisition, and are understood to be background- and nonlinearity-corrected. Only that part of the stray light, which is generated within the nominal FOV and spectral range of the sensor, i.e., related to the in-band signal, can be determined for each measurement and thus corrected

$$S_{\mathrm{IB}} = C \cdot S_{\mathrm{meas}}. \tag{3}$$

C is the stray-light correction tensor, which is derived from the PSFs (Point Spread Functions) of the sensor. C has the dimension $(\mathrm{pixels} \times \mathrm{channels})^2$. To obtain C, a PSF has to be assigned to every detector element.

To determine the PSFs of the HySpex VNIR-1600 sensor, a setup based on PLACOS [11], sketched in Fig. 2, is used to provide quasi-monochromatic light under specific viewing angles. PLACOS provides tuneable laser light between 220 and 2200 nm, with bandwidths < 0.5 nm within the spectral range of the sensor. The laser beam provided by PLACOS was coupled into a fiber bundle using a micro-lens beam homogenizer. The fiber bundle with a cross-sectional conversion was employed to guide the laser radiation to a 0.5 mm wide slit at the focal point of an off-axis mirror collimator with a focal length of 750 mm. The collimator provides then the irradiation for the sensor. The aperture slit at the collimator entrance is oriented so that only a few (two to three) geometric pixels are illuminated at a time.

The HySpex instrument is mounted on an angular rotation stage. Hence, by setting an angular position of the sensor with respect to the optical axis of the collimator, and given the quasi-monochromatic illumination, the chosen slit width and collimator focal length, any single detector element of the sensor can be illuminated.

1) Characterization Procedure: The hyperspectral sensor has a 12-bit analog-to-digital converter and, hence, a dynamic range of $2^{12} = 4096 \approx 10^{3.6}$. Stray-light characterizations of other instruments have shown that signal levels attributed to stray light are well below a factor of 10^{-5} of the maximum signal value, i.e., below the intrinsic dynamic range of the

This article has been accepted for inclusion in a future issue of this journal. Content is final as presented, with the exception of pagination.

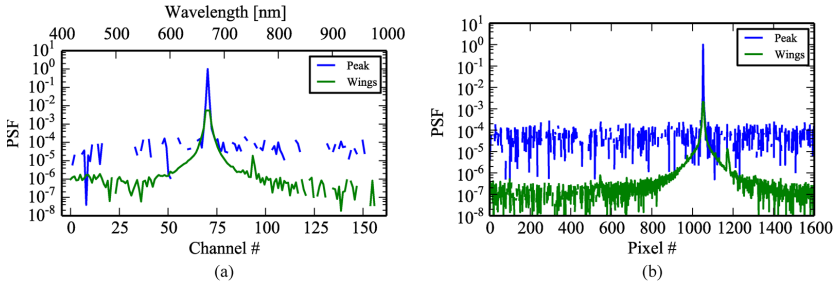

Fig. 3. (Blue) Peak and (green) wings measurements along the spectral (a) and spatial (b) axis for an illumination wavelength of 670 nm. Note that the signal of the peak measurement appears to be "choppy" because the small negative signals that occur after background correction and averaging cannot be represented in log scale.

instrument. These contributions should be measured and taken into account. In order to measure the PSFs with a resolution exceeding the intrinsic dynamic range of the instrument, a bracketing technique was used.

For each combination of laser wavelength $\lambda_k^{\mathrm{Laser}}$ and illumination angle θ_k, two measurements are performed, "peak" and "wings". The wings measurement is used to improve the signal-to-noise ratio of the PSF data away from the peak, whereas the peak measurement allows for the normalization of the wings data. For the peak measurement, the laser power is set so that the peak signal is $\approx 80\%$ of the saturation signal level. For the wings, the laser power or integration time is augmented, so that the signal increases by a factor of 10 to 100, which saturates a few detector elements of the FPA. In both cases, while the measurements are made in a dark laboratory, the background signal is measured with the laser radiation off and the shutter of the instrument open in order to account for any other disturbing light source in the laboratory. Each measurement consists in recording at least 100 signal and dark frames. The data are averaged, dark values subtracted from the signal frames and the nonlinearity corrections applied prior to further processing.

The effect of the pulsed laser radiation on Si-CCDs and equivalence of the determined line spread functions of array spectrometers when compared with results by cw-lasers has been explicitly tested on numerous array spectrometers [11], [17], [18]. The measurements at different powers of the pulsed laser are also a standard practice during initial tests and preparations for a complete stray-light characterization. In the case of the Hyspex instrument some of the PSF data was also obtained at lower powers of the laser beam. No effect on the recorded PSFs except higher noise in the wings could be seen.

For this study, the PSFs were measured at seven angular (or spatial) and at 55 spectral positions. This assumes that the PSFs change only slowly and gradually, so that PSFs can be assigned to each detector element via interpolation. This assumption was validated for the HySpex instrument used in this study [12] for the spatial and spectral cross sections of the PSF, the line spread functions and the SRFs.

The following normalization scheme allows to combine the wings and peak measurements to obtain PSFs, requiring only information contained within the peak and wings data. For

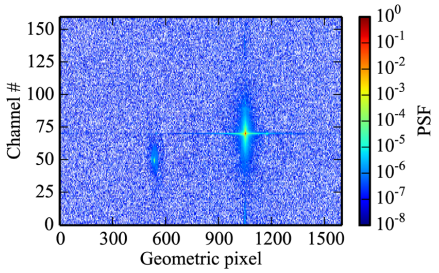

Fig. 4. Derived PSF for a wavelength of 670 nm.

every spatial pixel i, the wings spectrum is analyzed for saturation. If no saturation occurs, the wings spectrum is used.

In case saturation occurs in the wings spectrum, the sum $A_{\mathrm{wings}} = \int_{j=\mathrm{c_{min}}-2-3}^{\mathrm{c_{min}}-2} S_{i,j} + \int_{j=\mathrm{c_{max}}+2}^{\mathrm{c_{max}}+2+3} S_{i,j}$, where the integrals are computed using the trapezoidal rule, of the wing spectrum for the current spatial pixel i calculated. $\mathrm{c_{min,max}}$ designate the channels where the saturated region starts and ends, respectively. A_{wings} excludes the signals from the channels which are saturated, as well as the adjacent two channels, which might exhibit nonlinear effects such as blooming, and considers only the signals from the next three channels, to avoid summing over very small and noisy values. For the same channels, the sum A_{peak} of the peak signal is calculated. The peak signal is then normalized by the factor of $A_{\mathrm{wings}}/A_{\mathrm{peak}}$. For those channels that are saturated, the normalized peak data is used, otherwise the data of the wings measurement is considered. The combined PSF frame is then normalized to its maximum.

Fig. 3(a) shows the spectra and Fig. 3(b) the spatial cross section for the peak positions for the normalized wings and peak measurements and illustrates the normalization scheme. While the peak measurement resolves the laser peak well at short distances channels around the illuminated detector element, the radiometric resolution of the camera of the HySpex instrument does not allow to quantify long-range stray-light contributions. This is complemented by the wings spectrum.

Fig. 4 shows the derived PSF from the same measurement; the illuminated detector element has the coordinates $i = 1052$, $j = 70$. Most of the stray light is localized along the spectral

axis, with a focused component along the spatial axis. A ghost centered around detector element $i = 536$, $j = 49$, with a relative intensity of 0.04%, can be seen as well.

In principle, PSFs can be derived for every detector element by interpolation. Since the full stray-light correction tensor has $\approx 6.1 \cdot 10^{10}$ entries and would use $\approx$ 244 GB of memory, a reduction in complexity is achieved by binning in spatial direction. That is, instead of computing the stray-light correction on a grid of 1600 $\times$ 160 (spatial $\times$ spectral) detector elements, it is computed on a grid of 16 $\times$ 160 by binning along the spatial axis. The spatially binned PSF data is then used to calculate the stray-light correction tensor C', according to [16], [19].

This way of binning the PSF data frames was considered reasonable and chosen because the level of the stray light, indicated by the wings of the PSF, was observed to be generally higher in the spectral domain than in the spatial domain (see Fig. 3). This can be explained by the fact that in the spectral domain the stray-light properties are dominated by the spectrally dispersive apparatus, whereas in the spatial domain, the first order stray-light effects are caused by the imaging components. Thus, the weight of the spectral over the spatial stray light was found to be higher and the respective correction emphasized by the binning in the spatial direction.

2) Correction Procedure: To perform the correction with the reduced stray-light correction tensor C', a frame S_{meas} to be corrected is first binned to the reduced spatial resolution, yielding the frame $S_{\mathrm{meas,B}}$. $S_{\mathrm{meas,B}}$ is then stray light corrected using (3) with C' instead of C, yielding $S_{\mathrm{corr,B}}$. The stray-light contribution is calculated as $S_{\mathrm{SLC,B}} = S_{\mathrm{meas,B}} - S_{\mathrm{corr,B}}$. By resampling $S_{\mathrm{SLC,B}}$ to the original frames dimensions and subtracting it from S_{meas}, the stray-light corrected frame S_{corr} is obtained.

D. Radiometric Response

The three calibration procedures (see Section II-E) compared in this paper make use of three different radiometric response matrices R. Each matrix element $R_{i,j}$ represents the radiometric response of a detector element, i.e., the response matrices have the same dimension as the FPA. The indices i, j are referring to the geometric pixel and channel number, respectively, that together identify a detector element on the FPA.

The response matrices of the three calibration procedures are labeled R^{NEO}, R^{DLR1}, and R^{DLR2}. R^{NEO} was measured by the sensor manufacturer and was delivered together with the instrument. R^{DLR1} and R^{DLR2} were determined by combining absolute measurements with DLR's RASTA and relative measurements with DLR's large integrating sphere. RASTA [2], [20] is traceable to SI standards via a calibration at PTB [21]. Redundant calibration and stability monitoring provide an expanded uncertainty < 2.7% ($k = 2$) for the wavelength range of the HySpex VNIR-1600 sensor. However, due to constraints in the viewing angle geometry for the spectral radiance measurement of RASTA, this is only feasible for the pixels at the geometric center of the FOV of the HySpex sensors.

The radiometric response R^{DLR1} for the center pixels $i =$ 797 (for the left detector half) and $i = 803$ (for the right detector half) is obtained from the measurements as follows:

$$R_{i,j}^{\mathrm{DLR1}} = \frac{S_{i,j} - S_{\mathrm{bg},i,j}}{\gamma(S_{i,j} - S_{\mathrm{bg},i,j})} \cdot \frac{1}{L_{i,j}^{\mathrm{RASTA}}(\lambda) \cdot t_{\mathrm{int}}}\bigg|_{\mathrm{R}} \quad (4)$$

with S_{bg}, the background signal, measured at darkness, t_{int} the integration time, and $L_{i,j}^{\mathrm{RASTA}}(\lambda)$ the spectral radiance of RASTA spectrally resampled to the center wavelengths and bandwidths of detector element (i, j). The symbol $|_{\mathrm{R}}$ denotes the spectral resampling described in Section II-B, and γ the nonlinearity correction (see Section IV-A2).

The third radiometric response, R^{DLR2}, is derived according to

$$R_{i,j}^{\mathrm{DLR2}} = \Lambda\left[\frac{S_{i,j} - S_{\mathrm{bg},i,j}}{\gamma(S_{i,j} - S_{\mathrm{bg},i,j})}\right] \cdot \frac{1}{L_{i,j}^{\mathrm{RASTA}}(\lambda) \cdot t_{\mathrm{int}}}\bigg|_{\mathrm{R}} \quad (5)$$

where Λ denotes the stray-light correction of Section II-C.

To transfer the calibration from the geometric center pixels to all pixels, the HySpex sensor is illuminated by the large integrating sphere of the CHB, with an uncertainty due to inhomogeneities of $\pm$ 1.6% [22]. HySpex' center pixels calibration is used to determine the spectral radiance of the integrating sphere using (7) and (8). The radiometric response of all detector elements is derived using (4), (5) and substituting L^{RASTA} by the sphere's radiance.

E. Calibration

The manufacturer calibration of the HySpex VNIR-1600 sensor is extended in this study by accounting for a number of sensor properties that are ignored in the basic calibration. To illustrate the impact of these refinements on the calibrated data and on a derived product, water depth, three different calibration procedures are compared. The sequence of processing steps is illustrated in Fig. 5.

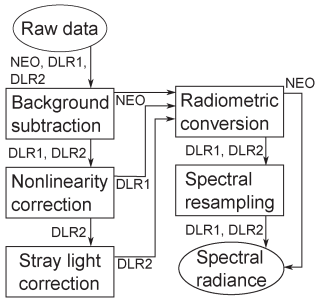

Fig. 5. Sequences of processing steps for the three calibration procedures NEO, DLR1, and DLR2.

a) Procedure NEO: It makes use of the radiometric response R^{NEO} and center wavelengths λ_i^{NEO} provided by NEO, and is applied using the NEO calibration software. The at-sensor radiance L^{NEO} is calculated as follows from the signals $S_{i,j}$ and background signals $S_{\mathrm{bg},i,j}$

$$L_{i,j}^{\mathrm{NEO}}\left(\lambda_{i,j}^{\mathrm{NEO}}\right) = (S_{i,j} - S_{\mathrm{bg},i,j}) \cdot \frac{1}{R_{i,j}^{\mathrm{NEO}} \cdot t_{\mathrm{int}}}. \quad (6)$$

This article has been accepted for inclusion in a future issue of this journal. Content is final as presented, with the exception of pagination.

Only background correction and radiometric conversion are performed for calibration, whereas nonlinear effects, spectral distortions and stray light are neglected.

b) Procedure DLR1: The calibration is performed with software developed at DLR and sensor data obtained in the CHB. The differences to procedure NEO lie in an altered radiometric response R^{DLR1}, correction of the radiometric nonlinearity and correction of spectral distortions by spectral resampling, leading to a different set of center wavelengths λ_i, as described in Section II-A. The calibration equation becomes

$$L_{i,j}^{\mathrm{DLR1}}(\lambda_{i,j}) = \frac{S_{i,j} - S_{\mathrm{bg},i,j}}{\gamma(S_{i,j} - S_{\mathrm{bg},i,j})} \cdot \frac{1}{R_{i,j}^{\mathrm{DLR1}} \cdot t_{\mathrm{int}}}\bigg|_{\mathrm{R}}. \quad (7)$$

c) Procedure DLR2: Calibration is performed as in procedure DLR1, but additionally stray light is corrected

$$L_{i,j}^{\mathrm{DLR2}}(\lambda_{i,j}) = \Lambda\left[\frac{S_{i,j} - S_{\mathrm{bg},i,j}}{\gamma(S_{i,j} - S_{\mathrm{bg},i,j})}\right] \cdot \frac{1}{R_{i,j}^{\mathrm{DLR2}} \cdot t_{\mathrm{int}}}\bigg|_{\mathrm{R}}. \quad (8)$$

Note that geometric corrections are not performed during radiometric calibration. These are done during geometric calibration using separate software like ORTHO [23] or PARGE [24]. The tasks of such software are to correct for the optical distortion known as keystone and for sensor movements during image acquisition, to resample the image pixels geometrically to a common grid, and to georeference the image.

III. Field Data and Image Processing

A. Field Campaign

The impact of the different calibration procedures on the derived water depth is studied for a data set from the Lake Starnberg. The lake is located in Southern Germany and covers an area of 65 km^2 with an average depth of 53 m and a maximum depth of 128 m. An airborne campaign with accompanying ship measurements was conducted on May 14, 2012, at the lake's southern shoreline near the marina of Seeshaupt (see Fig. 6). A HySpex image was acquired at a flight altitude of 2450 m above ground and an integration time of 22 ms. The attached FOV expander provided a swath width of 1.5 km.

The concomitant *in situ* measurements were made from two boats. One boat collected within 2 h of the overflight water samples, measured optical properties and determined Secchi depth at 7 stations. The other boat was equipped with an echo sounder (BioSonics MX Aquatic Habitat Echosounder; accuracy: 1.7 cm $\pm$ 0.2% of depth) and measured transects of water depth. These depth measurements were performed 2 weeks after the flight campaign. These data are used to validate the bathymetry maps derived from the HySpex data. Bottom reflectance $R^{\mathrm{b}}(\lambda)$ was derived by combining HySpex reflectance data with echosounding measurements [25]. It was obtained from 62 pixels of the HySpex image for which water depth is known from echosounding measurements (area Z in Fig. 6).

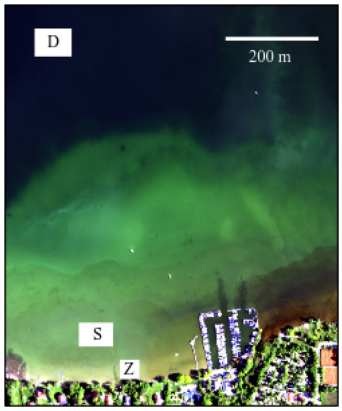

Fig. 6. Image of the test site. Reflectance spectra are shown in Fig. 13 (top) for the deep water location D and the shallow water location S. Bottom reflectance was determined for area Z.

B. Image Preprocessing

By applying the three calibration procedures described in Section II-E to the HySpex raw image, three images in units of at-sensor radiance are obtained. These are atmospherically corrected and converted into units of irradiance reflectance using ATCOR-4 [26], and then geometrically resampled and geo-referenced using ORTHO [23]. The resulting image has a pixel size equivalence of 2×2 m^2.

Processing of ATCOR-4 is initialized by resampling its database to the center wavelengths and bandwidths of the calibrated HySpex image. The critical parameters of atmosphere correction are aerosol type and concentration. ATCOR-4 uses horizontal visibility as a measure of aerosol concentration. These parameters are determined by applying ATCOR-4 to an area of dark dense vegetation on the same flight strip, and then hold constant for each image. Conversion to irradiance reflectance makes use of the solar irradiance model of [27]. The three calibrated data sets were processed with identical atmospheric parameters.

C. Inverse Modeling

Data analysis of the atmospherically corrected images is done by applying inverse modeling to each water pixel using the software WASI-2D [8]. The underlying model is the analytic shallow water model of Albert and Mobley [5], [28]. It parameterizes reflectance as a function of water depth, bottom albedo, concentrations and specific inherent optical properties of different water constituents, sun zenith angle, and viewing angle.

Major results of the field campaign were a bottom reflectance spectrum $R^{\mathrm{b}}(\lambda)$ to represent the ground at the test site, and identifying three parameters (X, Y, S) as the relevant fit parameters of the water body. The fit parameters describe parameters of the water body with large and variable impact on reflectance for the image: suspended matter concentration X, Gelbstoff

This article has been accepted for inclusion in a future issue of this journal. Content is final as presented, with the exception of pagination.

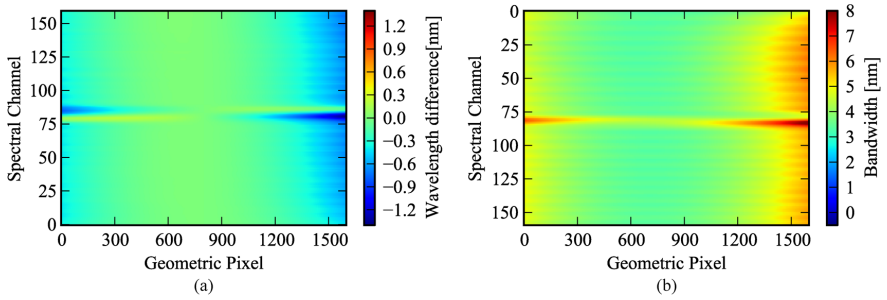

Fig. 7. Results of the spectral measurements. The plot on the left shows the difference of the center wavelength of each channel to the nadir pixel; the plot on the right shows the spectral bandwidths (FWHM). Adapted from [2].

absorption at 440 nm, Y, and spectral slope of Gelbstoff absorption, S.

The result of inverse modeling relevant for this study are maps of water depth, i.e., z_{B}, derived from the three reflectance images representing different calibrations. Thus, z_{B} is the fit parameter of interest for this study, whereas X, Y, and S are merely necessary for proper modeling. Inverse modeling requires to specify for each fit parameter an initial value and a range. The inversion algorithm of WASI-2D has been modified so that it uses two initial values for z_{B}. The one is set to 2 m, the other to the average of 15 previously processed image pixels surrounding the actual pixel. The z_{B} range is set to 0.05 to 50 m. For X, Y, and S, the averages from the 7 stations sampled during the field campaign are used as initial values: $X = 1.7$ mg/l, $Y = 0.6$ m^{-1}, $S = 0.014$ nm^{-1}. The ranges of X and Y are chosen sufficiently wide across the ranges of the *in situ* measurements to avoid frequent border hits: 0.3–10 mg/l for X, and 0–10 m^{-1} for Y. The range for S is set to its natural range of 0.010–0.025 nm^{-1} [29].

IV. Results

A. Calibration Differences

1) Spectral Response: The results of the spectral measurements are illustrated and discussed in detail in [2]. The smile is on the order of 0.2 spectral sampling intervals, i.e., the center wavelengths change across the FOV by up to 0.7 nm [see Fig. 7(a)]. This effect is corrected at DLR's calibration procedures, which spectrally resample the channels to equidistant center wavelengths λ_i (see Section II-A); it is not corrected for the NEO calibration. The differences of the center wavelengths $\lambda_i - \lambda_i^{\mathrm{NEO}}$ between DLR and NEO calibration range from -0.3 to 0.7 nm.

Fig. 7(b) shows the spectral bandwidths $\Delta\lambda$ of all detector elements; they vary between 3.5 and 6.0 nm. While this is not corrected within the NEO calibration, the two DLR calibration procedures convert all channels of all pixels to a common bandwidth of 5 nm, as described in Section II-A.

2) Nonlinearity: Nonlinearity was measured using the setup shown in Fig. 1 by tuning integration time and polarizer angle to alter the at sensor radiance over three orders of magnitude and the signal levels of HySpex over its complete dynamic range including saturation. By examining the signals of masked pixels on the edges of the FPA, it was ruled out that nonlinearity is related to variations of the electronic offset. A dependence of the nonlinearity on the integration time could be ruled out as well using the same setup. For this measurement, the polarizer angle and thus the at-sensor radiance were kept constant, whereas the integration time was varied. The changes of the HySpex signals turned out to be proportional to the changes of the integration times.

For the set of measurements with the highest integration time, the deviation from linearity Δ is computed as

$$\Delta(S_k) = \frac{S_k}{S_k^{\mathrm{rad}}} \cdot \max\left(\frac{S_k}{S_k^{\mathrm{rad}}}\right)^{-1} \tag{9}$$

with S_k the background-corrected HySpex signal and S_k^{rad} the radiometer signal, for the kth setting of the polarizer. The measurement series recorded with lower integration times are normalized such that their maxima lie on the cubic spline fit to the series with the highest integration time. This normalization scheme allows to obtain a single fit curve $\gamma(S)$ from measurements at disparate signal levels. The results are shown in Fig. 8. The observed nonlinear effect corresponds to an underestimation of the detector signal. The effect increases with decreasing signal. For the left detector half, the deviation from linearity exceeds 1% for signals below 60 DN and reaches 4% for a signal of 10 DN. For the right detector half, measured signals below 32 DN are in error by more than 1%, and a measurement of 10 DN has an error of 15%.

The correction of the nonlinearity is based on empirical correction functions $\gamma_{(\mathrm{left,right})}(S)$ of the left and right detector halves. These are shown in Fig. 8 as red curves. The correction is applied according to

$$S_{\mathrm{c}} = \frac{S}{\gamma(S)} \tag{10}$$

with S the background-corrected signal, and S_c the nonlinearity-corrected signal. Small negative signals, which can occur after background correction, and saturated signals are left uncorrected. Note that these correction functions are unique to each camera and depend on camera firmware settings.

This article has been accepted for inclusion in a future issue of this journal. Content is final as presented, with the exception of pagination.

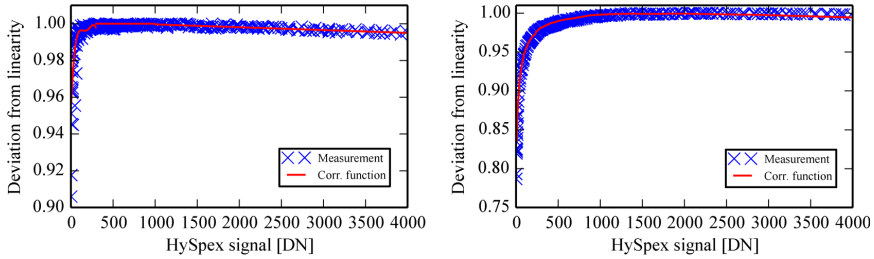

Fig. 8. Results of the nonlinearity measurements (crosses) and empirical correction functions γ (continuous lines). Left: left detector half; right: right detector half.

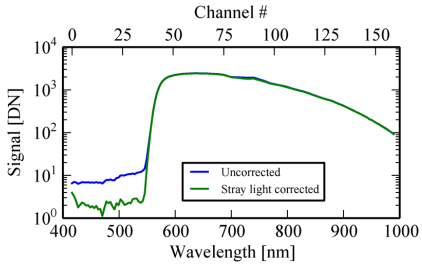

Fig. 9. Background- and nonlinearity-corrected raw signals from the measurement of a longpass-filter with a cutoff wavelength of 570 nm, prior to (blue line) and after stray-light correction (green line).

3) Stray Light: To validate the correction, it was applied to an image frame where the HySpex VNIR-1600 sensor was illuminated using an integrating sphere with broadband illumination from halogen lamps. The exit port of the sphere was covered with a longpass filter with a cutoff wavelength of 570 nm. For wavelengths < 530 nm, the filter has a transmission $< 10^{-4}$, so that the instrument is expected to measure zero signal at these wavelengths. Fig. 9 compares the background-corrected raw signal with the stray-light corrected signal: the background-corrected raw signal has a nonzero component at the blocked wavelengths, which mostly disappears after the stray-light correction. The remaining signals are on the order of the radiometric resolution.

4) Radiometric Response: To illustrate the wavelength dependence of the radiometric response of the HySpex VNIR-1600 sensor, Fig. 10 (top) shows R^{DLR2} of all channels for a single geometric pixel. The instrument has its maximum sensitivity near 550 nm; the sensitivity strongly decreases below 450 and above 800 nm. The spectral differences of the radiometric responses are illustrated in Fig. 10 (bottom). The ratio $R^{\mathrm{DLR1}}/R^{\mathrm{DLR2}}$ (green curve) is a measure of stray light of the HySpex VNIR-1600 sensor. It is close to 1 for all wavelengths, with the exception of two spectral regions, 416–500 nm and 700–760 nm. In the blue region, $R^{\mathrm{DLR1}}/R^{\mathrm{DLR2}}$ is increasing with decreasing wavelength, alike the radiometric response is decreasing, leading to maximum differences of 8% for the first channels. In the red region, the bump centered at 740 nm with an amplitude of 5% can be physically attributed to the edge of an order-sorting filter that is mounted on the

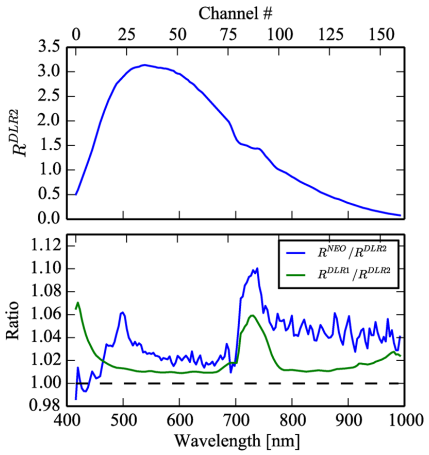

Fig. 10. Radiometric response R^{DLR2} in DN $\cdot$ m^2 $\cdot$ nm $\cdot$ sr/(ms $\cdot$ mW) for the center pixel $i = 800$. (Bottom) Illustration of spectral differences between the three calibration procedures for pixel $i = 800$. Blue: $R^{\mathrm{NEO}}/R^{\mathrm{DLR2}}$; green: $R^{\mathrm{DLR1}}/R^{\mathrm{DLR2}}$.

FPA; it obviously introduces local stray light. The blue curve shows that R^{NEO} is mostly consistent with R^{DLR2} within 5%. Significant wavelength-dependent differences are present at the same two spectral regions as before, 416–500 nm and 700–760 nm. The "noise-like" features in the curve $R^{\mathrm{NEO}}/R^{\mathrm{DLR2}}$ are caused by slight differences of the center wavelengths and the spectral resampling.

Fig. 11 shows the background-corrected raw spectral signal measured during radiometric calibration, and during data acquisition over lake Starnberg (see Section III-A). The intense red and infrared components of the calibration light source, which are not present in the water spectra, lead to systematic errors for shorter wavelengths if spectral stray light, which is present to a certain degree in all sensors, is not corrected properly. To illustrate the geometric differences of the different radiometric responses, Fig. 12 shows the ratio $R^{\mathrm{NEO}}/R^{\mathrm{DLR2}}$ for several channels. The high-frequency components correspond to slightly different results concerning the sensor's photo response non uniformity (PRNU). PRNU errors lead to image striping. Striping is observable using the NEO calibration data set, but does not appear when calibrating with the R^{DLR1} responses.

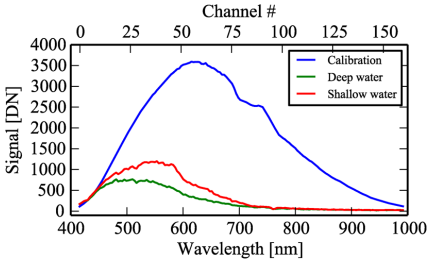

Fig. 11. Exemplary raw spectra of the radiometric calibration light source (blue line), shallow water (red line), and deep water (green line).

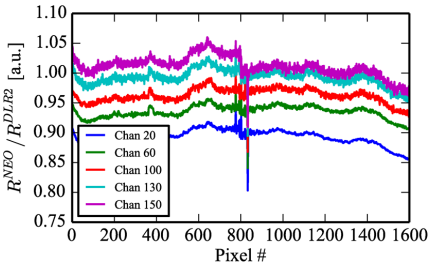

Fig. 12. Illustration of geometric differences between the NEO and DLR2 calibration procedures for channels 20, 60, 100, 130, 150 (bottom to top). For improved clarity, the curves are offset with respect to each other.

Not shown in Fig. 12 is a comparison of the responses R^{DLR1} and R^{DLR2}. Their ratio exhibits some spatial variations caused by the stray-light correction, but high-frequency components that cause striping are not present.

B. Impacts of Calibration Differences

1) Impacts on Reflectance: The HySpex image acquired at the test site was calibrated to at-sensor radiance using the three different calibration procedures described before, and then atmospherically corrected and converted to reflectance, as described in Section III-B. The resulting reflectances and their differences are illustrated in Fig. 13 (top) for representative spectra of deep and shallow water. The reflectance ratios for DLR1 and DLR2 calibration (see Fig. 13 (bottom), green and yellow curves) illustrate the impact of stray light on the derived reflectance spectra. As expected, their spectral shapes are similar to the response ratio shown in Fig. 10, i.e., stray light introduces wavelength-dependent errors mainly in two spectral regions, 416–500 nm and 700–770 nm. However, the reflectance ratio has a double peak in the red region, in which the response ratio has a single peak. The second peak is caused by the low radiance at 760 nm due to oxygen absorption of the atmosphere, which increases the relative intensity of stray light. The reflectance error depends on the radiance spectrum and reaches for the two examples 20% in the blue and 10% in the red region. For comparison, the response error from neglecting stray light is 8% and 5%, respectively, i.e., the reflectance error can be much higher than the response error.

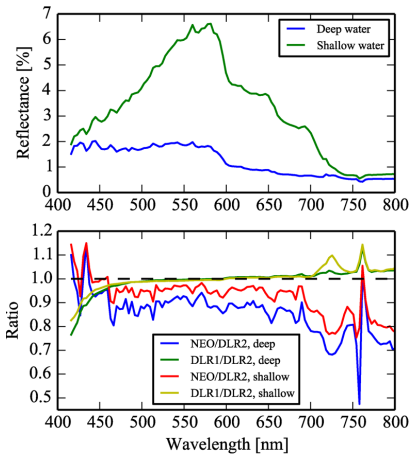

Fig. 13. (Top) Retrieved shallow (green) and deep (blue) water reflectances after atmospheric correction for the DLR2 calibration procedure. (Bottom) ratios of NEO and DLR2 calibrated reflectances (blue: deep water, red: shallow water), and ratios of DLR1 and DLR2 calibrated reflectances (green: deep water, yellow: shallow water).

In both the deep and shallow water example, the ratios of NEO and DLR2 reflectances differ from 1 at almost all wavelengths (see Fig. 13 (bottom), red and blue curves). The average reflectance difference is 5% for shallow water and 12% for deep water in the range from 500 to 650 nm. This is primarily a consequence of the altered radiance source used for calibration. The stray-light-induced systematic differences below 500 nm and in the range 700–770 nm are also present, leading in these spectral regions to reflectance differences up to 10% and 30%, respectively. Furthermore, the NEO to DLR2 ratios exhibit spiky features that are neither related to noise or to the water spectra. These are artifacts introduced by the atmospheric correction in combination with spectral differences of the two calibrated images. Most affected is the oxygen absorption region at 760 nm, in which the difference reaches 50% for the deep water spectrum.

2) Impacts on Bathymetry: Bathymetry was derived from the atmospherically corrected HySpex images by applying inverse modeling to each water pixel, as described in Section III-C. Fig. 14 shows the resulting map of water depth for the image that has been calibrated with the DLR2 procedure [see (8)]. Nonwater areas and depths $>$ 10 m are masked. The map is noise-free and shows clear bathymetry structures. Some artifacts from image processing can be observed: the occasional striping to the right of masked pixels is probably caused by fit parameter initialization errors of the used software WASI-2D. The maps derived using the NEO and DLR1 calibration procedures look very similar and are not shown. An echo-sounding survey provided 4148 independent water depth measurements in the image area. These are used for validation. Fig. 15 shows the comparison with the three sets of HySpex derived depth values. The correspondence between HySpex derived depths and echo-sounding data is similar for the three calibration procedures up to approximately 4.1 m. This critical

This article has been accepted for inclusion in a future issue of this journal. Content is final as presented, with the exception of pagination.

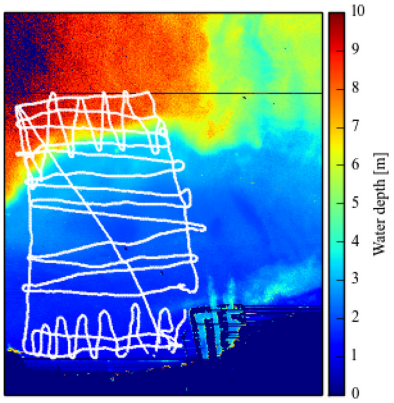

Fig. 14. Water depth retrieved from the data set shown in Fig. 6 using the DLR2 calibration procedure. The track of the echo sounder is marked in white. Nonwater areas and depths > 10 m are masked (dark blue).

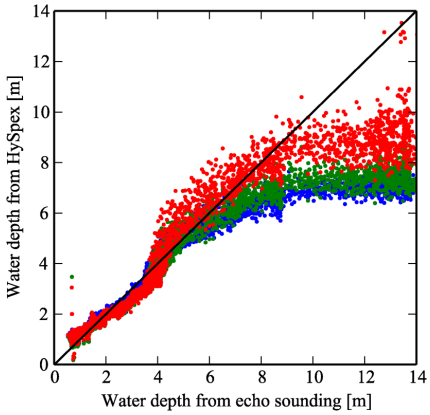

Fig. 15. Comparison of water depth derived from HySpex and from echo sounding (blue: NEO procedure; green: DLR1 procedure; red: DLR2 procedure).

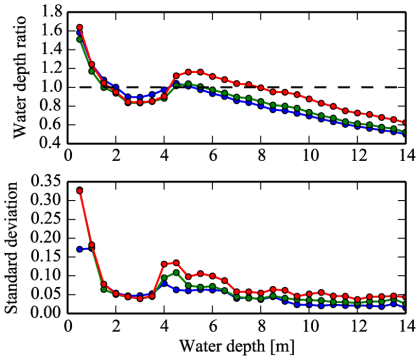

Fig. 16. Ratios of water depth derived from HySpex data and from echo sounding. Blue: $z_{\mathrm{B}}^{\mathrm{NEO}}/z_{\mathrm{B}}^{\mathrm{echo}}$, green: $z_{\mathrm{B}}^{\mathrm{DLR1}}/z_{\mathrm{B}}^{\mathrm{echo}}$, red: $z_{\mathrm{B}}^{\mathrm{DLR2}}/z_{\mathrm{B}}^{\mathrm{echo}}$.

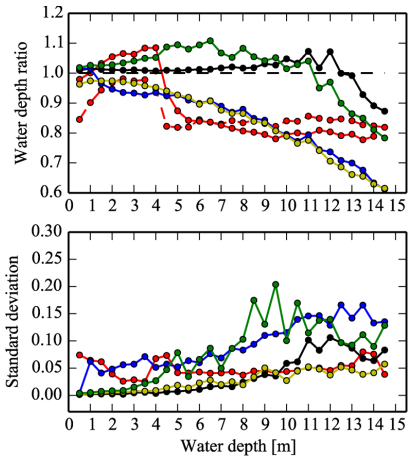

Fig. 17. Errors of water depth introduced by calibration errors. (Top) Mean water depth ratio; bottom: standard deviation. (Red) Derived from HySpex images; black, green, blue, yellow: derived from sensitivity analysis. For details see text.

depth is close to Secchi depth, which was determined during the field campaign as 4.2 ± 0.5 m [25]. For water deeper than Secchi depth, the differences in calibration are larger and lead to significant systematic differences of the derived water depth. To quantify the differences between the water depths derived from HySpex ($z_{\mathrm{B}}^{\mathrm{NEO}}, z_{\mathrm{B}}^{\mathrm{DLR1}}, z_{\mathrm{B}}^{\mathrm{DLR2}}$) and from echo sounding ($z_{\mathrm{B}}^{\mathrm{echo}}$), the ratios were calculated and averaged in steps of 0.5 m. The result is shown in Fig. 16. No model is perfect, thus systematic errors introduced by the processing algorithm are unavoidable. Error sources are, besides sensor calibration, atmosphere correction, reflections at the water surface, and optical properties of water constituents and the bottom. Errors of image georeferencing, measurement uncertainties of the echo-sounding data, water level changes between flight campaign and echo-sounding survey, and water depth variation within the 2×2 m^2 pixels can introduce additional validation errors. The systematic errors, represented in Fig. 16 by the mean water depth ratios, show a similar depth-dependent relative pattern for all three calibration procedures, but differ in the absolute values. For the most elaborate procedure (DLR2), the differences can reach $\pm$ 20% for the depth range 1–11 m (see Fig. 16, red curves). The depth range with a correspondence better $\pm$ 20% is 1–8 m for the NEO procedure and 1–9 m for the DLR1 procedure. The statistical error, represented by the standard deviation, is very similar for all three procedures up to 3.5 m. In deeper water, it is lowest for the NEO procedure and highest for the DLR2 procedure. For the DLR2 procedure, the standard deviation is typically 5% and exceeds 10% below 1.5 m and from 4.0 to 5.5 m.

In order to quantify the changes of water depth introduced solely by calibration differences, and to exclude the echo sounding and processing errors, the ratio $z_{\mathrm{B}}^{\mathrm{NEO}}/z_{\mathrm{B}}^{\mathrm{DLR2}}$ was calculated. Fig. 17 shows mean and standard deviation of these ratios binned in 0.5 m steps (red solid lines). The shallowest depth range, for which echo-sounding measurements are available, is 0.25–0.75 m. The average ratio $z_{\mathrm{B}}^{\mathrm{NEO}}/z_{\mathrm{B}}^{\mathrm{DLR2}}$ is 0.98

TABLE II
IMPROVEMENTS OF CALIBRATION COMPARED WITH THE MANUFACTURER PROCEDURE

Effect	Magnitude	Improvement
Center wavelength changes across FOV (smile)	< 0.7 nm	Resampling to equidistant center wavelengths
Spectral bandwidth changes across FOV and with band number	3.5 – 6.0 nm	Resampling to defined bandwidth (5.0 nm)
Nonlinear readout of detector signal	> 1 % for signals $< 60/32$ DN (left/right detector half)	Correction of raw signal using empirical functions for left and right detector half
Spectral stray light falsifies radiometric response measurement	up to 8 % in first channels, up to 5 % near 730 nm	Correction of response matrix using stray light tensor
Spectral and spatial stray light illuminates wrong detector elements	scene dependent	Correction of image frame using stray light tensor
Inhomogeneity of radiance source used for calibration	unknown	Inhomogeneity of DLR's integrating sphere $< \pm 1.6$ % (peak to valley)
Uncertainty of radiance source used for calibration	unknown	SI traceable radiance standard provides expanded uncertainty $< 2.7\%$ ($k = 2$)

$\pm$ 0.07 ($N = 193$) for this range. It increases to 1.08 $\pm$ 0.07 ($N = 399$) at 4 m. Beyond 5 m, the ratio scatters around 0.81 with an average standard deviation of 0.05. Hence, calibration errors systematic introduce errors of water depth on the order of 2–7% below 4 m and 19% above 5 m. Above 4 m, calibration errors lead to an underestimation of water depth.

The ratio $z_{\mathrm{B}}^{\mathrm{DLR1}}/z_{\mathrm{B}}^{\mathrm{DLR2}}$ is also shown in Fig. 17 (red dashed line). Since the only difference between procedures DLR1 and DLR2 is stray light, this curve illustrates the impact of stray light on water depth retrieval. The error is depth dependent and has a minimum of 3% from 2.0 to 3.5 m. It increases steadily with decreasing water depth, reaching 15% in the depth range 0.25–0.75 m. In water deeper than Secchi depth, it remains nearly constant at 16%. The ratios $z_{\mathrm{B}}^{\mathrm{DLR1}}/z_{\mathrm{B}}^{\mathrm{DLR2}}$ and $z_{\mathrm{B}}^{\mathrm{NEO}}/z_{\mathrm{B}}^{\mathrm{DLR2}}$ are quite similar from 5 to 14 m, but differ in shallower water; hence, the NEO discrepancies are mainly caused by stray light in deep water, and by uncertainties of the calibration light source in shallow water.

In order to clarify the propagation path of calibration uncertainties toward water depth errors, a sensitivity analysis was made as follows. In a first series of computations, a number of reflectance spectra $R_{\mathrm{rs}}^{\mathrm{fwd}}(\lambda)$ were calculated for depths ranging from 0.5 to 10 m in 0.5 m steps using the same model as taken for inverse modeling. Calibration errors were simulated by multiplying $R_{\mathrm{rs}}^{\mathrm{fwd}}(\lambda)$ with the ratio $R_{\mathrm{rs}}^{\mathrm{DLR1}}(\lambda)/R_{\mathrm{rs}}^{\mathrm{DLR2}}(\lambda)$ derived from the HySpex image for deep water (see Fig. 13). Sensor noise was accounted for by adding Gaussian distributed random noise and calculating each spectrum 20 times. The noise amplitude of each channel was derived from the HySpex image as the standard deviation of a homogeneous deep water area. The simulated spectra were adjusted to the measurements by using the same model constants as during inverse modeling, and taking for the model variables the means of the fit parameters at the locations of echo-sounding measurements: $X = 1.8$ mg $\cdot$ l^{-1}, $Y = 0.34$ m^{-1}, $S = 0.014$ nm^{-1}. Each spectrum $R_{\mathrm{rs}}^{\mathrm{fwd}}(\lambda)$ was then inverted with water depth as fit parameter. Similar as before, the ratios $z_{\mathrm{B}}^{\mathrm{fit}}/z_{\mathrm{B}}$ were calculated, with $z_{\mathrm{B}}^{\mathrm{fit}}$ denoting the fit result and z_{B} the true water depth from forward modeling. The averages and standard deviations of that ratio are shown as black curves in Fig. 17. Obviously, calibration errors and image noise alone introduce only small errors of water depth: up to 12 m, z_{B} is overestimated by 2% on average. The main depth errors are consequently the result of error propagation between the fit parameters.

A second series of calculations was made to illuminate this error propagation between fit parameters. In contrast to the first series, a second parameter was changed additionally during forward calculation and treated as fit parameter during inverse modeling. X, Y, S were used subsequently as second variable. Their ranges were set to mean $\pm$ standard deviation at the locations of echo-sounding measurements: 0.4 to 3.2 mg $\cdot$ l^{-1} for X, 0.15 to 0.54 m^{-1} for Y, and 0.012 to 0.016 nm^{-1} for S. The curves representing the ratios $z_{\mathrm{B}}^{\mathrm{fit}}/z_{\mathrm{B}}$ and their standard deviations are shown in Fig. 17 (blue: X, yellow: Y, green: S). It can be seen that the simulated errors of the reflectance spectra now introduce significant errors of water depth. While S as second fit parameter leads to an overestimation of z_{B} up to 11 m, X and Y cause an underestimation at all depths. With X or Y as fit parameter, the simulated z_{B} errors are similar to those derived from the HySpex image with DLR1 calibration for z_{B} between 1.5 and 11 m (red dashed line). From 11.5 to 14 m, the simulated errors are even higher than the observed ones. It can be concluded that the observed systematic errors of z_{B} are primarily the result of error propagation between z_{B}, X and Y, introduced by wavelength-dependent radiometric errors due to calibration errors.

V. CONCLUSION

A. Improvements of Calibration

Much effort was spent to refine the manufacturer calibration of a HySpex VNIR-1600 sensor. Table II provides an overview of the considered effects and summarizes the resulting improvements.

This article has been accepted for inclusion in a future issue of this journal. Content is final as presented, with the exception of pagination.

The spectral properties of the HySpex sensor are not constant across the FOV or across the spectral bands, hence introducing to a hyperspectral image differences of the center wavelengths of individual bands up to 0.7 nm in across track direction, and variable bandwidths ranging from 3.5 to 6.0 nm. These sensor properties are left uncorrected in the manufacturer calibration procedure, whereas DLR calibration makes the hyperspectral images spectrally consistent by applying resampling. Note that also the geometric sensor properties change across both the FOV and the spectral bands (see [2] for details). As these do not affect radiometric calibration, they are not discussed in this study.

Radiometric calibration has been improved compared with manufacturer calibration by considering additionally radiometric nonlinearity and stray-light effects, and using calibration sources with small and well-known uncertainties of absolute and relative radiance values. The measurable nonlinear effects of the HySpex VNIR-1600 instrument are related to the signal amplitude, but not to wavelength, integration time or radiance. They are caused by the detector readout circuit, and because the left and right detector halves are read out using separate circuits, the nonlinear effect is different for the left and right image half and introduces a clearly visible brightness step in dark images. DLR calibration corrects for this effect by using two signal-dependent empirical correction functions. It eliminates the brightness step which is present in images calibrated using the NEO software.

The key improvement of nonlinearity correction is to enable reliable stray-light measurements. The signal during the stray-light characterization is on the order of a few DN, and for such low signals the nonlinear effects of DLR's HySpex VNIR-1600 sensor can exceed 15%. Stray-light measurements at the PLACOS facility of PTB have shown that the diffuse stray-light level of the instrument is quite low and leads only in two spectral regions to significant errors of the radiometric response. In the first region, 416–500 nm, the low detector response for blue light in combination with high red and infrared radiance from the calibration light source is responsible for an overestimation of the response by up to 8% for the first channels. In the second region, 700–760 nm, a filter mounted on the detector introduces local stray light up to 5%. A stray-light tensor has been derived which is used to correct the radiometric laboratory measurements as well as the airborne measurements. A comparison of stray light corrected and uncorrected airborne data from deep and shallow waters has shown that the derived reflectance spectra can have significant wavelength-dependent differences up to 20%. It should be noted that calibration errors introduced by stray light cannot be corrected reliably using ground based validation measurements (vicarious calibration) because the error depends on the radiance spectrum.

Relative radiometric measurements were made using an integrating sphere with an inhomogeneity below $\pm$ 1.6% (peak to valley). Using these data, the marked stripes in the raw images vanish in the calibrated images, whereas the radiometric response provided by the sensor manufacturer NEO conserves some striping after calibration. Absolute radiometric calibration is based on DLR's RASTA, which is traceable to SI units with an expanded uncertainty below 2.7% ($k = 2$). In contrast, no uncertainties are given for the manufacturer calibration, thus prohibiting comparisons with data from other calibrated instruments. A comparison of DLR and NEO radiometric responses reveals differences between 4 and 6% over most of the spectral range, and up to 10% between 700 and 760 nm. Assuming similar uncertainties of NEO's and DLR's radiance sources, and excluding the effects caused by stray light and striping, the responses are basically consistent.

Summarizing, the commercial hyperspectral sensor HySpex VNIR-1600 is a well-working instrument with only small issues related to smile, nonlinearity and stray light, and the standard calibration provided by the manufacturer NEO is quite accurate. Nevertheless, it could be shown in this study that thorough laboratory measurements, together with improved sensor models, can improve the calibration. The most relevant effect for refined calibration is stray light. However, stray-light characterization was by far the most complex and time-consuming task. The development of the laboratory infrastructure and data analysis software was on the order of some person years, whereas the measurements themselves required approximately one week. Thus the question is legitimate whether applications benefit significantly from such calibration efforts which require a sophisticated calibration facility [10]. An answer is given for a shallow water application, i.e., determination of water depth.

The characterization procedures presented in this paper can be applied to many current hyperspectral instruments. The stray-light correction was already validated on nonimaging spectrometers [11], [17], and current imaging spectrometers are expected to behave and benefit similarly in this regard. One indication for this comes from atmospheric correction algorithms, which routinely fail to retrieve correct reflectances for very short wavelengths [30], [31]. The remaining issue with the stray-light measurement scheme is that not all FPAs might be able to handle the short laser pulses of PLACOS, or the saturation levels required by the bracketing scheme. The measurements in such cases, however, could be carried out using spectrally tunable quasi-cw mode lasers with a pulse-to-cw converter, like those available at the TULIP setup of PTB [32]. Note that independent validation of sensor characterization is always valuable to ascertain the correct function of the instrument. Furthermore, SI-traceability of hyperspectral sensor data calibration can only be achieved by characterization measurements performed on this level of detail.

B. Impacts on Water Depth

A HySpex image from a shallow water area of lake Starnberg was used to study the impact of different calibration procedures on the derived bathymetry map. An echo-sounding survey provided more than 4000 independent measurements of water depth for validation. Since optical bathymetry should not be feasible beyond Secchi depth [33], and Secchi depth was 4.2 $\pm$ 0.5 m, no echo-sounding measurements were made at depths above 14 m. Surprisingly, the HySpex derived depths were highly correlated for the entire depth range of the echo-sounding data set, i.e., up to three times Secchi depth. Even at the upper limit of 14 m, the relative standard deviation is below 5%.

The relative standard deviation between HySpex derived depths and echo-sounding measurements, i.e., the statistical error, does not depend much on the calibration procedure. The depth ratios, representing systematic differences, are slightly different for NEO and DLR1 calibration, but change significantly for DLR2 calibration, i.e., after stray-light correction. The remaining systematic differences, reaching 20% for the depth range from 1 to 11 m, can be attributed to errors from atmosphere and sun glint correction, concentrations and optical properties of water constituents, bottom reflectance, georeferencing and echo-sounding data.

In order to separate the calibration errors from the other error sources, the water depths obtained from the HySpex images were compared for the NEO and DLR2 calibration procedures. The differences are between 2 and 7% at depths below 4 m, and nearly constant at 19% from 5 to 14 m. The comparison with the two DLR procedures unveils the radiance uncertainty of the calibration light source as the major error source below approximately Secchi depth, and stray light above. As shown by sensitivity analysis, only a small fraction of the error (typically 2%) is caused by the calibration error directly, whereas most of it is the indirect consequence of error propagation between the fit parameters. Due to this mechanism, even small calibration errors can lead to large errors of fit parameters, including water depth.

To answer to the question how much an application profits from extended calibration effort: the improvement was up to 19% in our case. Thus, calibration and model should be as accurate as possible since error propagation between fit parameters can amplify errors.

ACKNOWLEDGMENT

The authors would like to thank the DLR's Flight Department and the OpAiRS team for the flight campaign, and the Limnological Station of TU Munich for the echo sounding and *in situ* measurements. The authors also thank R. Richter and C. Köhler for the fruitful discussions.

REFERENCES

[1] M. E. Schaepman *et al.*, "Earth system science related imaging spectroscopy—An assessment," *Remote Sens. Environ.*, vol. 113, pp. S123–S137, Sep. 2009.

[2] K. Lenhard, A. Baumgartner, and T. Schwarzmaier, "Independent Laboratory Characterization of NEO HySpex Imaging Spectrometers VNIR-1600 and SWIR-320m-e," *IEEE Trans. Geosci. Remote Sens.*, vol. 53, no. 4, pp. 1828–1841, Apr. 2015.

[3] C. D. Mobley *et al.*, "Comparison of numerical models for computing underwater light fields," *Appl. Opt.*, vol. 32, no. 36, pp. 7484–7504, 1993.

[4] Z. Lee, K. L. Carder, C. D. Mobley, R. G. Steward, and J. S. Patch, "Hyperspectral remote sensing for shallow waters. I. A semianalytical model," *Appl. Opt.*, vol. 37, no. 27, p. 6329, Sep. 1998.

[5] A. Albert and C. Mobley, "An analytical model for subsurface irradiance and remote sensing reflectance in deep and shallow case-2 waters," *Opt. Exp.*, vol. 11, no. 22, p. 2873, Nov. 2003.

[6] A. G. Dekker *et al.*, "Intercomparison of shallow water bathymetry, hydro-optics, and benthos mapping techniques in Australian and Caribbean coastal environments," *Limnology Oceanogr., Methods*, vol. 9, pp. 396–425, 2011.

[7] C. Giardino*et al.*, "BOMBER: A tool for estimating water quality and bottom properties from remote sensing images," *Comput. Geosci.*, vol. 45, pp. 313–318, Aug. 2012.

[8] P. Gege, "WASI-2D: A software tool for regionally optimized analysis of imaging spectrometer data from deep and shallow waters," *Comput. Geosci.*, vol. 62, pp. 208–215, Jan. 2014.

[9] Norsk Elektro Optikk, "Web site of Norsk Elektro Optikk," Dec. 2013. [Online]. Available: http://www.neo.no/

[10] P. Gege *et al.*, "Calibration facility for airborne imaging spectrometers," *ISPRS J. Photogramm. Remote Sens.*, vol. 64, no. 4, pp. 387–397, Jul. 2009.

[11] S. Nevas, M. Lindemann, A. Sperling, A. Teuber, and R. Maass, "Colorimetry of LEDs with array spectroradiometers," *MAPAN*, vol. 24, no. 3, pp. 153–162, Dec. 2009.

[12] A. Baumgartner, P. Gege, K. Claas, K. Lenhard, and T. Schwarzmaier, "Characterisation methods for the hyperspectral sensor HySpex at DLR's calibration home base," in *Proc. SPIE*, Edinburgh, U.K., 2012, pp. 1–8.

[13] P. Mouroulis, R. O. Green, and T. G. Chrien, "Design of pushbroom imaging spectrometers for optimum recovery of spectroscopic and spatial information," *Appl. Opt.*, vol. 39, no. 13, pp. 2210–2220, May 2000.

[14] J. Kauppinen and J. Partanen, *Fourier Transforms in Spectroscopy*, 1st ed. Hoboken, NJ, USA: Wiley-VCH, 2001.

[15] Adimec, "Adimec website," Jun. 2014. [Online]. Available: http://www.adimec.com/

[16] M. E. Feinholz *et al.*, "Stray light correction algorithm for multichannel hyperspectral spectrographs," *Appl. Opt.*, vol. 51, no. 16, pp. 3631–3641, Jun. 2012.

[17] S. Nevas and A. Sperling, "Stray light characterization of array spectroradiometers with PLACOS for applications in the UV spectral range," in *Proc. NEWRAD*, Daejeon, Korea, 2008, pp. 17–19.

[18] A. Sperling, O. Larionov, U. Grusemann, and S. Winter, "Stray-light correction of array spectrometers using tunable pulsed and CW-lasers," in *Proc. NEWRAD*, Davos, Switzerland, 2005, pp. 1–2.

[19] Y. Zong, S. W. Brown, K. R. Lykke, and Y. Ohno, " *Simple Matrix Method for Stray Light Correction in Imaging Instruments*," U.S. Patent 20090059210 A1, Mar. 5, 2009.

[20] T. Schwarzmaier, A. Baumgartner, P. Gege, C. Köhler, and K. Lenhard, "DLR's new traceable radiance standard "RASTA"," in *Proc. IGARSS*, Munich, Germany, 2012, no. 1, pp. 1–4.

[21] D. R. Taubert *et al.*, "Providing radiometric traceability for the calibration home base of DLR by PTB," *AIP Conf. Proc.*, 2013, vol. 1531, pp. 376–379.

[22] A. Baumgartner, "Characterization of integrating sphere homogeneity with an uncalibrated imaging spectrometer," in *Proc. WHISPERS*, Gainesville, FL, USA, 2013, pp. 1–4.

[23] R. Müller, S. Holzwarth, M. Habermeyer, and A. Müller, "Ortho image production within an automatic processing chain for hyperspectral airborne scanner ARES," in *Proc. EARSeL Workshop 3D-Remote Sens.*, Porto, Portugal, 2005, pp. 1–9.

[24] D. Schlaepfer, M. E. Schaepman, and K. I. Itten, "PARGE: Parametric geocoding based on GCP-calibrated auxiliary data," in *Proc. SPIE 3438, Imaging Spectrometry IV*, 1998, pp. 1–11.

[25] P. Gege, "A case study at Starnberger See for hyperspectral bathymetry mapping using inverse modeling," in *Proc. WHISPERS*, Lausanne, Switzerland, 2014, pp. 1–4.

[26] R. Richter and D. Schlapfer, "Geo-atmospheric processing of airborne imaging spectrometry data. Part 2: Atmospheric/topographic correction," *Int. J. Remote Sens.*, vol. 23, no. 13, pp. 2631–2649, 2002.

[27] J. M. Fontenla, J. Harder, W. Livingston, M. Snow, and T. Woods, "High-resolution solar spectral irradiance from extreme ultraviolet to far infrared," *J. Geophys. Res.*, vol. 116, no. D20, Oct. 2011, D20108

[28] A. Albert, "Inversion technique for optical remote sensing in shallow water," Ph.D. dissertation, Univ. Hamburg,Hamburg, Germany, 2005.

[29] M. Babin *et al.*, "Variations in the light absorption coefficients of phytoplankton, nonalgal particles, and dissolved organic matter in coastal waters around Europe," *J. Geophys. Res.*, vol. 108, no. C7, p. 3211, 2003.

[30] R. Richter and D. Schläpfer, *Atmospheric/Topographic Correction for Satellite Imagery (ATCOR—2/3 User Guide)*. Wil, Switzerland: ReSe Applications Schläpfer, Jan. 2014.

[31] B. C. Gao, M. J. Montes, Z. Ahmad, and C. O. Davis, "Atmospheric correction algorithm for hyperspectral remote sensing of ocean color from space," *Appl. Opt.*, vol. 39, no. 6, pp. 887–896, Feb. 2000.

[32] M. Schuster, S. Nevas, and A. Sperling, "Validation of short-pulse-laser-based measurement setup for absolute spectral irradiance responsivity calibration," *Appl. Opt.*, vol. 53, no. 13, pp. 2815–2821, May 2014.

[33] C. Flener, "Estimating deep water radiance in shallow water: Adapting optical bathymetry modelling to shallow river environments," *Boreal Environ. Res.*, vol. 18, no. 6, pp. 488–502, 2013.

This article has been accepted for inclusion in a future issue of this journal. Content is final as presented, with the exception of pagination.

Karim Lenhard received the diploma degree in physics from the University of Bonn, Bonn, Germany, in 2008. He has been working toward the Ph.D. degree at the University of Zurich, Zurich, Switzerland, since 2012.

Since then, he has been a Researcher with the German Aerospace Center (DLR). At DLR, he is jointly responsible for operating and improving DLRs calibration laboratory for imaging spectrometers. His research interests are the spectral and radiometric calibration of hyperspectral instruments, with a focus on stray-light issues.

Andreas Baumgartner received the B.Eng. degree in mechatronics with focus on optical engineering, in 2008 and the M.Eng. degree in electrical engineering and information technology from the University of Applied Sciences, Hochschule Deggendorf, Deggendorf, Germany, in 2010.

Since then, he has been working with the German Aerospace Center (DLR) and is jointly responsible for DLR's calibration laboratory for imaging spectrometers. His research interests are improving the setup, methods and software for the spectral, and geometric and radiometric calibration of imaging spectrometers.

Peter Gege received the diploma in physics from TU München, Munich, Germany, and the Ph.D. degree from the University of Hamburg, Hamburg, Germany, in 1994.

He has been employed as a Research Scientist with the German Aerospace Center (DLR), Oberpfaffenhofen, Germany, since 1988. From 2001 to 2004, he headed the group "Inland waters". Since 2005, he has been the Head of the group "Sensor Characterisation and Concepts." His research interests include radiative transfer modeling in water and the atmosphere, algorithm development for optically complex water types (inland, coastal, shallow), inverse modeling, and calibration of field spectrometers and hyperspectral sensors.

Saulius Nevas has studied at Helsinki University of Technology, Espoo, Finland. He received the M.Sc. degree in optical technologies and optical communications, in 2000 and received the Dr.Sc. (Tech.) degree in 2004.

Since 2006, he has been with Physikalisch-Technische Bundesanstalt, Braunschweig, Germany, and currently leads the working group "Spectroradiometry." His research interests are concentrated on applications of wavelength-tuneable lasers in radiometry.

Stefan Nowy received the diploma degree in physics from TU München, Munich, Germany, in 2006, and the Ph.D. degree from the University of Augsburg, Augsburg, Germany, in 2010.

From 2010 to 2013, he was with Physikalisch-Technische Bundesanstalt (PTB, National Metrology Institute of Germany). For this paper, he implemented the calculation of the stray-light correction tensor from the pulsed laser for advanced characterization of spectroradiometers measurements. Since 2014, he has been a Product Manager and R&D Scientist with Gigahertz-Optik GmbH.

Armin Sperling studied electronic engineering and telecommunications at the University of Applied Science in Dieburg and semiconductor physics and optics at the Technical University of Braunschweig. He received the Ph.D. degree for his work at the Physikalisch-Technische Bundesanstalt (PTB), Braunschweig, Germany, in metrology for solar cells, in 1994.

After a period of six years working in the field of R&D in industry, he came back to PTB, where he now leads the working group Photometry. His main research focus is on laser-based characterization of photometric and radiometric detectors, including array-spectroradiometers and the metrology with imaging devices in photometry and radiometry. He is an Associate Director of Division 2 of CIE and Member of the Advisory Board of the Standardization Committee NA 58 for Light of the German standardization body DIN.

Chapter 5

Airborne Prism Experiment Calibration Information System

This chapter has been published as: Hueni, A., Lenhard, K., Baumgartner, A., & Schaepman, M. E. (2013). Airborne Prism Experiment Calibration Information System. IEEE Transactions on Geoscience and Remote Sensing.

This article has been accepted for inclusion in a future issue of this journal. Content is final as presented, with the exception of pagination.

Airborne Prism Experiment Calibration Information System

Andreas Hueni, *Member, IEEE*, Karim Lenhard, Andreas Baumgartner, and Michael E. Schaepman, *Senior Member, IEEE*

***Abstract*— The calibration of remote sensing instruments is a crucial step in the generation of products tied to international reference standards. Calibrating imaging spectrometers is particularly demanding due to the high number of spatiospectral pixels and, consequently, the large amount of data acquired during calibration sequences. Storage of these data and associated meta-data in an organized manner, as well as the provision of efficient tools for the data analysis and fast and repeatable calibration coefficient generation with provenance information, is key to the provision of traceable measurements. The airborne prism experiment (APEX) calibration information system is a multilayered information technology solution comprising a database based on the entity–attribute–value (EAV) paradigm and software written in Java and MATLAB, providing data access, visualization and processing, and handling the data volumes over the expected lifetime of the system. Although developed in the context of APEX, the system is rather generic and may be adapted to other pushbroom-based imagers with little effort.**

***Index Terms*— Imaging spectroscopy, relational database, sensor calibration.**

I. Introduction

REMOTE sensing technologies have the potential of acquiring data with a spatial coverage, temporal resolution, and continuity, which allow the parameterization of earth system science models at regional and global scales. Such remotely sensed data are referred to as fundamental climate data records (FCDRs). These basic data are subsequently transformed into end-user products describing essential climate variables (ECVs) by data assimilation [1]. Of the 44 ECVs identified in the Global Climate Observing System Second Adequacy Report [2], a total of 25 are largely dependent on satellite observations, effectively rendering remote sensing instruments one of the most important means of data collection for earth system sciences.

Of the multitude of available sensor systems, the family of imaging spectrometers exhibits a high potential for the retrieval of ECVs from all spheres of the climate system [3], [4]. While some spaceborne imaging spectrometers do exist [5], [6] or are planned, [4], [7]–[9], most instruments [10]–[13] are currently deployed on airborne platforms [3].

Manuscript received September 29, 2012; revised December 2, 2012; accepted January 22, 2013.

A. Hueni and M. E. Schaepman are with the Remote Sensing Laboratories, University of Zurich, Zurich 8057, Switzerland (e-mail: ahueni@geo.uzh.ch; schaep@geo.uzh.ch).

K. Lenhard and A. Baumgartner are with the Remote Sensing Technology Institute, Oberpfaffenhofen 15236, Germany (e-mail: karim.lenhard@dlr.de; andreas.baumgartner@dlr.de).

Color versions of one or more of the figures in this paper are available online at http://ieeexplore.ieee.org.

Digital Object Identifier 10.1109/TGRS.2013.2246575

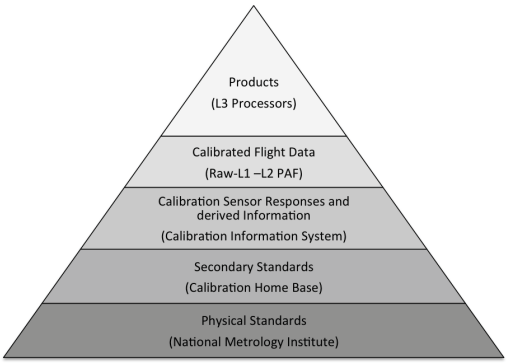

Fig. 1. DIKW applied to remote sensing system calibration and product generation.

The calibration of imaging spectroradiometers and their data is technically demanding due to the high number of spatial/spectral pixels, and also hampered by the notion that spectroradiometer measurements are still considered as one of the least reliable of all physical measurements [14], [15]. Calibration is an essential and critical step before higher product generation can be achieved with the accuracies required for the successful parameterization of climate models in order to reduce the uncertainties of predictions [16].

Imaging spectrometers generally measure at-sensor radiances by reference to Internation System of Units (SI) through either laboratory or vicarious calibration. System calibration allows defining the traceability of measurements to the SI standard and hence enables the comparison of data stemming from different sensor systems. Such traceable calibration forms the basis for the generation of consistent geophysical and biophysical products [17].

These dependencies may be conceptualized using an adapted data–information–knowledge–wisdom (DIKW) [18], [19] representation (Fig. 1). DIKW is a model describing the building of knowledge from information based on facts or data and hence has found use in multidisciplinary research, ranging from philosophy to systems analysis [20], [21]. Various flavours of the DIKW do exist [22], and for the purpose of this research, we add the notion of signals [23] while omitting the rather elusive tier of wisdom [24].

This article has been accepted for inclusion in a future issue of this journal. Content is final as presented, with the exception of pagination.

The lowest tier is formed by the physical standards, i.e., SI units, as provided by national metrology institutes. Here, instrumentation used in calibration laboratories may be calibrated and thus made traceable; these are the secondary standards, equivalent to tier 2. This second tier produces optical stimuli leading to calibration sensor responses and information derived thereof. These data and information constitute the third tier and are held by a component we refer to as the calibration information system (CAL IS). Calibrated flight data (tier 4) are based on calibration information and are generated by processing and archiving facilities (PAFs) [25]. Products are the output of higher level algorithms and form the top of the pyramid, being equivalent to knowledge as it adds actionability to information [22].

We define a CAL IS as a system layer that stores raw sensor calibration and characterization data and generates information describing the instrument's electrooptical chain that converts signals from a continuous electromagnetic space into digital numbers within a discrete space. The CAL IS produces calibration coefficients used by the PAF to calibrate flight data and by this establishes the traceability link between airborne data and physical standards. The CAL IS holds information that leads to an enhanced understanding of the sensor properties and characteristics and as such supports the calibration scientists in developing their system knowledge.

This paper defines the data sources generating raw calibration and characterization data, lists the requirements for a CAL IS, and documents the chosen implementation. The system is targeted at the airborne prism experiment (APEX) system, but the general concept essentially applies to any frame based imaging system.

II. Data Sources

A. APEX

The European Agency's (ESA) airborne imaging spectrometer APEX was developed under the PROgramme de Développement d'EXpériences scientifiques (PRODEX) program by a Swiss–Belgian consortium with the concept phase starting in 1998 and leading to a first test flight in 2008. APEX was formally accepted by ESA at the end of 2010 and entered the exploitation phase in 2011. It features up to 532 spectral bands in full spectral mode, ranging from 375 to 2500 nm. Spectral programmability of the VNIR sensor enables achieving higher signal-to-noise ratios (SNRs) by reducing the number of bands in a binned configuration. Data are acquired in 1000 pixels across track with a field of view (FOV) of 28°, resulting in ground pixel sizes of 1.5–2.5 m at typical flight levels of 3000–5000 m above ground.

The main components of the APEX system are: 1) an optical subunit (OSU) containing the optoelectronics; 2) a control and storage unit (CSU) comprising the instrument control computer, solid state devices for the storage of the data stream, and a positioning system; and 3) a temperature control unit (TCU) responsible for the regulation of the OSU optical base plate temperature to a stabilized 20 °C.

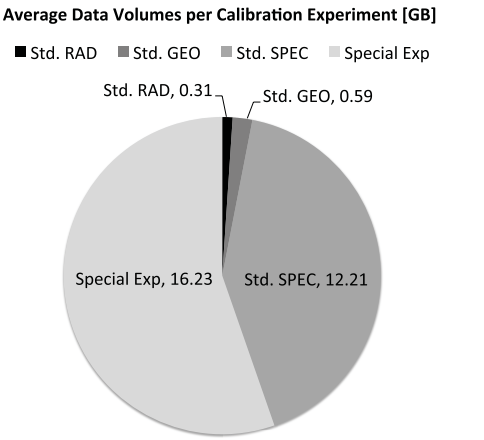

Fig. 2. Average data volumes acquired during CHB missions per calibration experiment [GB].

TABLE I
Number of Meta-Parameters Per Frame for the Most Common Calibration Experiments

Experiment	Meta-Parameters Per Frame
Absolute radiometric calibration	157
Relative radiometric calibration (flat fielding)	158
Spectral calibration	217
Across-track geometric calibration	204
Along-track geometric calibration	204

Image data are stored frame-wise, where a frame consists of a combined readout of VNIR and SWIR detectors. The storage size per frame depends on the chosen binning pattern. Frames in the default binning mode amount to storage sizes of 0.62 MB and to 1.1 MB in the unbinned mode. Meta-data per frame contain information on instrument settings (e.g., integration time) and readings of various auxiliary sensors (pressure, temperature, and voltages) mounted in the OSU. A total of 88 meta-parameters are recorded for each frame by the CSU.

B. APEX Calibration

APEX calibration refers to the calibration and characterization of APEX in the calibration home base (CHB) with the goal of collecting data allowing the radiometric, geometric, and spectral calibration of the instrument [11]. These data essentially form the base for the estimation of calibration coefficients that are applied to imaging data during data calibration. Standard system calibration runs generate around 13 GB of data, while special experiments on average double the standard data volume (Fig. 2). CHB calibration missions take place once to twice a year, resulting in a total raw data size of around 300 GB accumulated since 2007. Data are stored on the file system of the CSU in automatically generated hierarchical folder structures with a naming convention for both folders and files.

This article has been accepted for inclusion in a future issue of this journal. Content is final as presented, with the exception of pagination.

Calibration settings are sent to the CHB equipment and these parameters are also added to the meta-data file associated with each frame. The total number of meta-parameters per frame generated during calibration depends on the calibration experiment, comprising APEX system parameters and CHB settings as provided by the CHB interface (Table I).

C. Calibration Home Base

The CHB was commissioned by ESA for the calibration of APEX [26]. However, the laboratory can also be used for other sensors since imaging spectrometers used in optical remote sensing often display similar properties. The CHB provides defined light sources in the typical wavelength range of these instruments: integrating spheres for the radiometric calibration, and a monochromator assembly and a slit-collimator assembly in combination with a rotating mirror on a translation stage to generate optical stimuli for the spectral and geometric calibration, respectively.

Since the spectral and geometric calibration procedures can consist of several hundreds or thousands of short measurements with different settings of the involved light source, the CHB was set up with automation kept in mind. The software controlling the calibration procedures was designed based on the master/slave pattern. The slave controls the CHBs devices and light sources, while the master runs calibration procedures by requesting CHB settings from the slave and managing the data acquisition of APEX. Generally speaking, the master provides an interface to define measurement sequences, with specific routines being written for each specific calibration experiment.

The communication between master and slave follows a synchronous client/server model, in which the slave takes the role of the server and receives requests by the master [27]. Each request for CHB settings generates exactly one reply, which indicates that the CHB has assumed the requested state and is ready for measurements. This reply contains all the meta-data generated by the CHB. These meta-data stem from the laboratory devices, e.g., specifying the wavelength to which the monochromator is set, and from an environmental sensor that supplies room temperature, atmospheric pressure, and humidity.

The communication between master and slave takes place over a TCP/IP connection, allowing operating master and slave on separate computers. The data are exchanged in the form of eXtensible Markup Language (XML) files, which are human-readable and well suited for the small amount of data exchanged, which is on the order of 1 kB per request/reply. An additional advantage of using XML files is that their content can be checked for consistency against an XML schema definition (XSD) file. This includes checks for the completeness of the parameters, their data type, and their valid ranges.

III. Requirements

APEX CAL IS requirements are mainly based on the goals of generating system calibration information and enhancing the knowledge about the system in general, as well as on the expected data volumes over the nominal lifetime of the system.

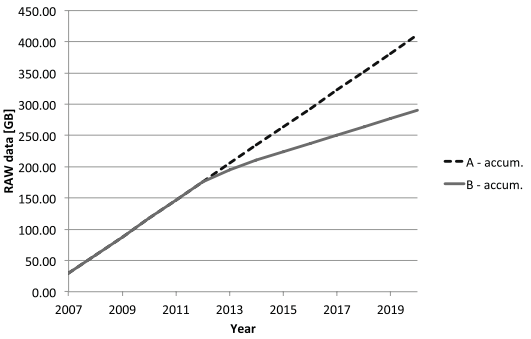

Fig. 3. Estimated RAW data volumes for two scenarios over the expected system lifetime.

A. Data Volumes

The CAL IS must be able to handle the estimated total data volume over the expected lifetime of the system. The data volume includes calibration data acquired during the operational stage, currently set at 10 years, plus data acquired during the system acceptance test phase. Raw data volumes range between 290 and 410 GB under two different scenarios (Fig. 3): 1) per-annum volumes remain identical to the current average, i.e., special experiments constitute half of the volume and 2) special experiment volumes diminish exponentially over time, leading to per-annum volumes mainly governed by the standard data calibration runs.

These estimated volumes will roughly double when data are processed to level-1 in the CAL IS, i.e., leading to total sizes in the order of 0.6–0.8 TB.

B. Generic Frame Support

The number of spectral pixels of an APEX frame depends on the binning patterns applied to the VNIR detector. The CAL IS must be able to seamlessly handle frames of differing binning patterns, including the frame-size-independent storage and the generation of calibration coefficients for various binning patterns.

C. Flexible Meta-Parameters

A flexible handling of the number of meta-parameters per frames is required because: 1) the number of meta-parameters is dependent on the particular calibration experiment; 2) the CAL IS can add new meta-parameters generated from both meta-data and frame data during the forming of information; and 3) upgrades in the CHB may lead to different or additional meta-parameters over time.

D. Data Ingestion, Data Structuring, and Quality Control

Data ingestion must be an automated process, retrieving frame and meta-data from the files generated during calibration. Near-real-time data control during calibration missions requires loading data into the CAL IS at various points in time, i.e., allowing data ingestion with a delta data loading capability.

This article has been accepted for inclusion in a future issue of this journal. Content is final as presented, with the exception of pagination.

The data hierarchy generated during the calibration campaign on the CSU reflects the experimental structure and provides an easy way for the users to interactively navigate through the wealth of calibration data. The CAL IS must retain such structures and replicate them within the database.

Automated generation of quality flags is important for two reasons: 1) detection of problems in near-real time during calibration runs and 2) exclusion of unsuitable data from calibration coefficient generation processes. Examples include saturation detection or thresholds for system temperatures and pressures.

E. Support for Processing Levels

The concept of processing levels is identical to the one commonly implemented in airborne and space-based instrument PAFs. The levels reflect various stages of processing in the system and allow the efficient generation of higher level products without a complete reprocessing starting from raw sensor data. Storage of several processing levels allows the easy study of effects caused by transforming processes, helping the debugging of according algorithms. Table II lists the required processing levels of the APEX CAL IS.

F. Interactive Data Exploration

Developing a sound knowledge about the sensor system and controlling the generation of calibration coefficients require the ability to graphically explore data in an interactive fashion. The dimensions to be explored are: 1) the spatiospectral pixel values of a frame 2) the time domain as the system response changes due to modification of or noises in the external stimuli or due to system-inherent drifts or noises 3) the meta-data space [28] and 4) combined meta-data–spatiospectral domains where the spectral response at any pixel may be mapped versus parameters of the meta-data space.

G. Provenance

Provenance describes the origin and evolution of data [29]. This information is important for the APEX CAL IS, as it allows tracing effects found at any processing stage to its original cause. Provenance data forms a graph consisting of data sources, data sinks, and processes. Such a topology is also highly useful when the definition of uncertainty budgets is required, as all the contributing sources of noise are essentially given by the provenance graph.

An example is the level-0 to level-1 processing, i.e., the dark current correction: each level-1 frame must have an associated creating process description and links to both level-0 frame and dark current frame used for the correction.

IV. Concepts

A. Overall Architecture

The APEX CAL IS is designed as a multilayered system (Fig. 4). A relational database management system (RDBMS) serves as storage solution, implemented by a MySQL server (Version 5.5). Data are stored in physical database tables within the RDBMS, using a mixture of traditional relational

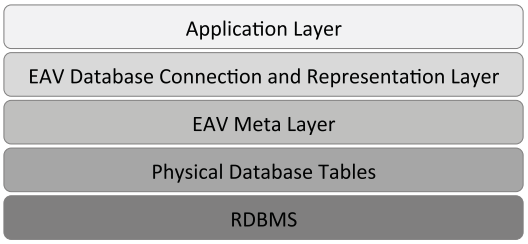

Fig. 4. APEX CAL IS layers.

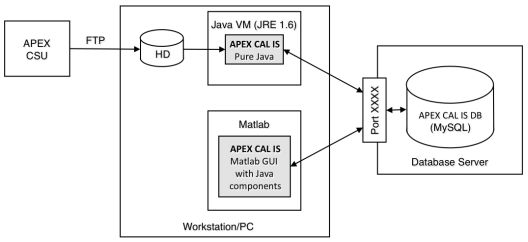

Fig. 5. APEX CAL IS system architecture and dataflow.

database model and of a meta-system architecture known as the EAV paradigm [30]. The EAV meta-layer is the representation of the meta-data known to the APEX CAL IS by according entries in physical database tables. The database connection and representation layer is written in Java and handles all communications with the database, offering functionality for data insert, querying, and deletion, essentially mapping the EAV information to an object-oriented representation and representing frame data as matrices. The application layer holds routines for the analysis and processing of data, including the graphical representation. This layer is implemented in MATLAB (Release 2010a) using Java components for the communication with the database and for some graphical data representations.

Fig. 5 illustrates the dataflow and the overall system architecture. Frame and meta-data files are transferred from the APEX CSU to a workstation by FTP. A pure Java-based application is used to ingest these files into the APEX CAL IS database, which is hosted by a database server. Higher level processing, visualization, and analysis are carried out in a MATLAB environment, relying on Java components for database communication, i.e., on lower level data services as implemented in the EAV database connection and representation layer. The illustrated setup reflects the most common one, but installations where a laptop takes the role of a database server and processing computer at the same time are also feasible, e.g., within the CHB where a direct feed into a remote database server may not be as performant as a locally hosted database instance. The centrally hosted database allows the simultaneous data access by several researchers.

This article has been accepted for inclusion in a future issue of this journal. Content is final as presented, with the exception of pagination.

TABLE II
APEX CAL IS PROCESSING LEVELS

Designator	Name	Description
Level-0	RAW	Raw frame data as generated by APEX
Level-1	DC Corrected	Frame data corrected for the dark current, taken from the closest dark-current frame in the acquisition time line
Level-2	Desmeared	Frame data corrected for image smear caused by the readout mechanism (applies only to the VNIR part of the frame)
Level-3	Intermediate system coefficients	Coefficients describing the electrooptical chain, but not yet integrated for all spatiospectral pixels, e.g., gains/offsets for the nadir pixels
Level-4	System calibration layers	Coefficients for each spatiospectral pixel, i.e., a matrix of the same dimension as the imaging frame and directly applicable in the data calibration process within the APEX PAF

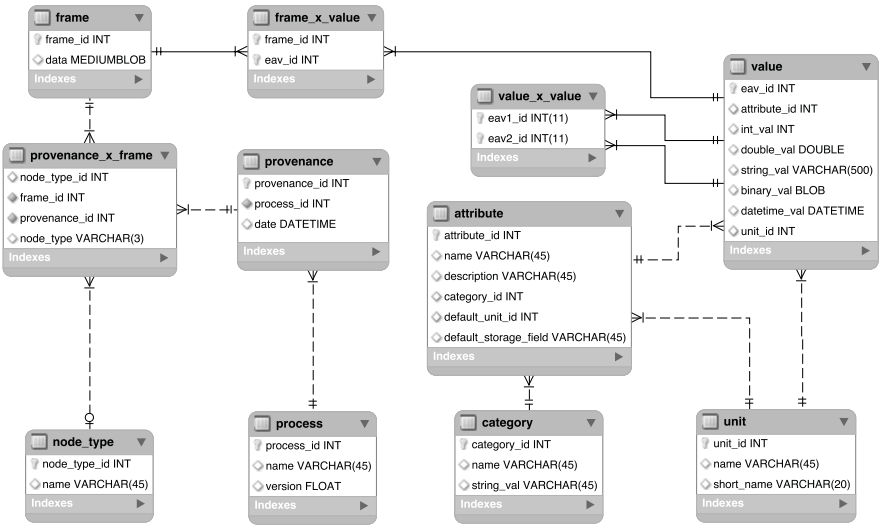

Fig. 6. Entity relationship diagram of the APEX CAL IS schema.

B. Database Schema

The APEX CAL IS schema (Fig. 6) implements the EAV paradigm, but uses some traditional relational modeling as well, as suggested in [31]. The frame table represents the primary data, i.e., the entities. Most of the entries in this table are APEX frames, but as data are stored as binary large objects, data of other dimensionality may be stored as well. Frame data are serialized objects of matrix classes belonging to the UJMP package [32], and as such may assume dimensionalities between 1 and 3, referring to single spectra, 2-D frames, and imaging cubes, respectively.

Frames can be associated with multiple meta-parameters, which in turn may be referenced by multiple frames. This is achieved by a cross-relational table (frame_x_value) and a value table holding the actual values. A tuple within the value table may assume the data types of integer, floating point, string, binary object, or date/time, storing them in the applicable fields, i.e., adopting one possible representation of the values within an EAV schema [31]. Value tuples can refer to other value tuples by the way of the value_x_value cross-relational table. This is heavily used in the modeling of hierarchical folder structures in the system, while the representation of these relations is part of the system software.

Value tuples refer to both attribute and unit table entries. The APEX CAL IS handles attributes and units in a flexible way, allowing for values of a certain attribute to have differing units. To support the use of the EAV-related Java classes in other projects where a more strict approach is needed, namely the SPECCHIO spectral database project [33], the option to define standard units and default storage fields was added to the attribute table.

Provenance is modeled by a provenance table, representing instances of transformations. A transformation comprises a processing module of a certain version, stored in the process table, and a number of input and output frames, cross-linked via the provenance_x_frame table and the input/output node type given by entries in the node_type table.

Data integrity is ensured by foreign keys and the corresponding constraints in the database schema.

C. Data Insert

Data insert deals with the ingestion of data stored on the file system and with the insert of processing output.

This article has been accepted for inclusion in a future issue of this journal. Content is final as presented, with the exception of pagination.

Data loading from the file system uses concepts developed in the SPECCHIO project [33]. It is based on the assumption that data are organized by campaign on the file system, each campaign folder forming the top of a hierarchical file/folder structure. Data are ingested into the database campaign by loader processes that parse the campaign folder structure, replicate the hierarchy in the database, and insert all spectral files. Data loaders are aware of the existing content of the database and thus will only insert new data found during the parsing. This functionality allows the continuous update of a campaign while data are being collected in the CHB and is referred to as the "delta loading capability."

Meta-data are highly redundant between frames, especially within the same calibration experiments, and a redundancy minimization is required to reduce the number of inserted meta-data parameters per frame and improve the query responsiveness of the system. This is accomplished by retaining a dynamic list of already inserted meta-parameters in the loader processes. In case a meta-parameter matches an existing entry in the list, only a reference is inserted into the frame_x_value table.

Meta-data inserts are carried out as bulk inserts, i.e., all rows that are inserted for a frame into the values table and frame_x_values table, respectively, are combined into one SQL statement, thus minimizing the database statement overhead and leading to an optimized loading speed.

Attributes and units defined in the EAV meta-layer are automatically updated when new entities are encountered during insert procedures, i.e., the EAV layer is built on the fly while files are ingested or higher level processing generates new attributes.

Frames generated by processing existing frames in the database, e.g., dark current correction, are inserted into the database by adding a new row in the frames table and linking with existing meta-data of the input frames, thus avoiding data redundancy. Meta-parameters not applying to the higher level frames are removed or updated, thus either omitting a link between new frames and original meta-parameters, or adding new meta-parameters with updated values.

D. Data Retrieval

Generally speaking, all data retrieval is based on meta-data subspace projections, i.e., frames are selected by defining meta-parameter restrictions and the frames complying with these are contained within a subspace [28]. In practice, two variations for the definition of such projections exist: 1) selection via browsing of the data hierarchy where frames are identified by either their filenames or their containing directories and 2) the programmatic definition of SQL queries that convert the restrictions to actual statements. For many instances of data processing or analysis, data selection involves both methods by first selecting a set of frames in the interactive browser and then projecting that set to a subspace by additional restrictions. Fig. 7 illustrates such a combined use on the example of the radiometric calibration in the form of a sequence diagram.

The EAV database connection and representation layer offers a number of methods to select data, refine subsets, and group data by multiple attributes. The Table III lists some of the main methods/classes and examples of their practical application.

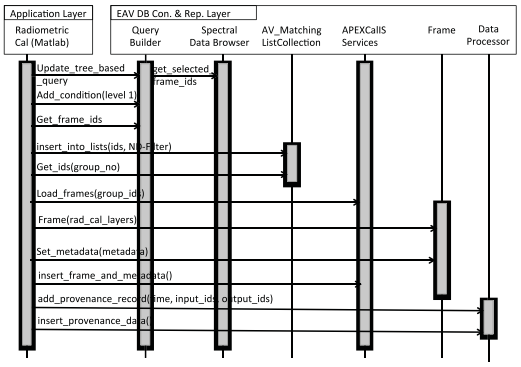

Fig. 7. Sequence diagram illustrating data selection, loading, and product/provenance inserts for the radiometric calibration.

E. Data Processing

Data processing relates to the transformation of data, either for analysis purposes or for the generation of calibration products. Data volumes are rather big, and efficient procedures are required to select and load data from the database and insert possible results. In this respect, the number of database statements must be minimized while ensuring that the memory allocation is sufficient to hold the data to be processed.

To meet these needs, data processors use the optimized methods offered by the EAV database connection and representation layer to make use of tuned functions, such as the data bulk-loading feature. Data that may be used multiple times during a processing run are ideally cached, such as dark-current frames applied in the dark-current correction procedure.

A further strategy is the partitioning of larger datasets during processing by loading only subsets into memory. This division into data collections is, e.g., applied when processing spectral calibration data, where a full calibration dataset may be several gigabytes in size.

Data processors written in Java are subclasses of a data processor class, which implements the support of provenance generation. Provenance data are compiled during processing, adding timestamps and input/output frames for each atomic operation. These accumulated provenance data are inserted into the database as one statement once the processor finished, thus minimizing the database communication overhead. Processors written in MATLAB can use an instance of the data processor class to handle the provenance generation in a seamless manner (see Fig. 7).

F. Data Representation

The graphical representation to the user is key to the efficient handling of these multidimensional data. Developing a graphical user interface (GUI) in MATLAB while using

This article has been accepted for inclusion in a future issue of this journal. Content is final as presented, with the exception of pagination.

TABLE III
MAIN METHODS/CLASSES FOR DATA RETRIEVAL, LOADING, AND GROUPING

Method/Class	Use/Example
get_list_of_metaparameter_vals (frames, attribute)	Return a list of values for a certain attribute for a set of frames, e.g., list of integration times per frame
get_eav_ids (frame, attributes)	Return all eav_ids of a frame, optionally restricted to an attribute set. Used to retrieve a complete metadata set or a metadata subset of a frame
get_eav_ids (frames, attribute)	Generic function to return all eav_ids of a set of frames for an attribute, optionally distinct: e.g., get eav_ids holding the neutral density filter value used in absolute calibration
get_closest_product_frames (frame, product)	Returns frames that are products (level-3 and level-4) and are closest on a time line to the supplied frame: e.g., used to identify spectral calibrations to apply in convolution operations required for radiometric calibration
get_frames_by_attribute (frames, attribute, value)	Returns the frames of a set of frames that have an attribute with a value matching the supplied one: e.g., select frames out of a subset that have a certain neutral density filter value
frame_bulk_reading (frames)	Read frames into memory using one database statement for speed reasons. Used to build spectral cubes on the fly
AV_MatchingListCollection	Class to group a set of frames by multiple attribute values: e.g., used to group dark current frames by integration time to build a dark current system model or grouping of absolute calibration frames by neutral density filter as required for radiometric calibration

Java Swing components allows for the seamless integration of the functionality offered by the EAV database connection and representation layer with the advanced plotting tools of MATLAB. A Java key component is the hierarchical data browser that graphically represents the structure of the data as stored in the database as recursive attribute–value entries. The integration of Swing components in the MATLAB GUI is accomplished by the JControl package [34].

Frame data within the MATLAB environment are represented as matrices. These are populated by first loading the frames from the database into Java where they are deserialized and exist as UJMP instances. In a second step, data are transferred into MATLAB matrices by using a UJMP to standard Java double-array conversion.

V. RESULTS

This section demonstrates the capabilities of the system by documenting the loading speed for data retrievals and the graphical data representation on the example of the main application user interface. A detailed description of the individual calibration and analysis modules is beyond the scope of this paper and will be treated in dedicated future publications. Readers interested in a practical usage example of the APEX CAL IS are referred to the case study presented in Section VI.

Data loading speed was tested by loading frame collections selected in the spectral data browser and ranging between 1 and 600 items into MATLAB, using three different setups to give indicative speeds for the most likely configurations: 1) database server and application running on the same machine, i.e., localhost; 2) database server hosted by a machine in the same Ethernet network as the workstation running the application; and 3) database hosted by a server at our APEX partner institution VITO and the application running on a workstation at the University of Zurich, with a network connection established using VPN tunneling. The latter setup being the one used for shared database access for both the operations and science teams of the APEX project. At the time of the testing, calibration data for the years 2010–2012 was loaded into the system, consisting of 190 000 frames and 10.2 million meta-parameter entries.

Fig. 8 shows the resulting loading speeds for the three setups: the total loading time refers to the time needed to load frames from the database into MATLAB (top left); the Java loading time is equivalent to the time spent in the EAV database connection and representation layer to load the frame data from the database into the memory of the workstation (top right); the total loading time per frame is the amount of time required to load one frame into MATLAB under the scenario of different collection sizes (bottom left); and the Java loading time per frame is the time spent within Java per frame for the different collection sizes (bottom right).

The results show clearly that the loading speed is a function of the number frames and largely governed by the time spent in the EAV database connection and representation layer, loading the frame data from the database into Java allocated memory. The loading times are also governed by the type of database connection, with the localhost being fastest as it uses a Unix socket file, while the most overhead and delays occur for the tunneled connection to a server in a different physical network.

The loading times per frame are a function of both the number of frames and the database server hosting location. Data loading involves a certain overhead such as the sending of statements and the compilation of meta-data on the frame sizes. Hence smaller frame collections show a notable overhead per frame, which gets minimized as collection sizes increase.

Actual speeds of the system can vary, as they are influenced by the database server configurations such as the memory allocated for the caching of query results, the overall network traffic, the number of other processes running on the application workstation, the amount of RAM available, and

This article has been accepted for inclusion in a future issue of this journal. Content is final as presented, with the exception of pagination.

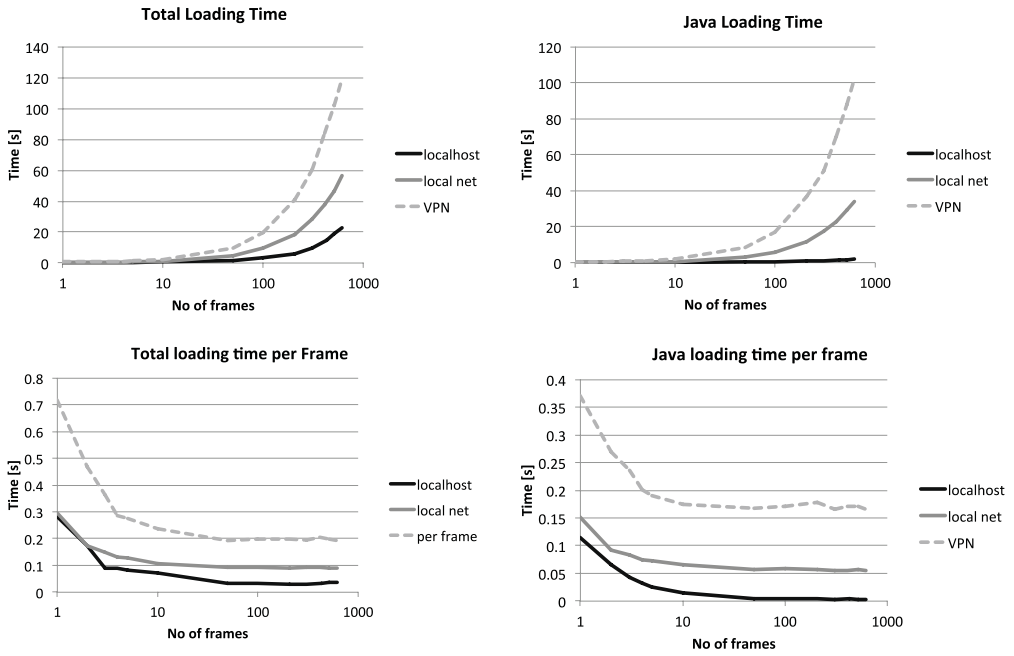

Fig. 8. Total and per-frame loading times from the database into Java and MATLAB.

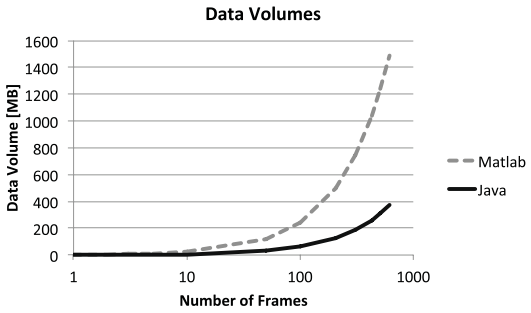

Fig. 9. Frame data volumes when loading frames into Java and MATLAB.

the fragmentation of the current free memory, which impacts the speed of memory allocation within MATLAB. Hence, the shown loading speeds hold true only when enough RAM to hold the whole virtual cube is available, and the performance will drop significantly when the operating system is forced to use virtual memory.

The data sizes involved in the loading speed test are shown in Fig. 9, illustrating the increase in data volume as frames represented by 16-bit integer matrices in Java are moved into MATLAB matrices of 64-bit floating point data type. Frame collection sizes bigger than 150 frames are very rare under usual system usage, with the most common number of frames being loaded ranging between 1 and 50, i.e., the loading speed remains in an agreeable range for the users.

Fig. 10 shows the main interface to APEX CAL IS written in MATLAB. The spectral data browser Java component is featured on the left of the window, showing the data held by the database organized by campaigns, and the directory structure below each campaign reflecting the original storage on disk. Selected data are visualized in the four displays to the right of the data browser, showing a frame view with 1000 pixels across track and spectral pixels depending on the binning pattern (top left), a spectral profile of the selected spatial position (top right), an across-track profile for the selected spectral position (bottom left), and an along-track profile for the selected across-track and spectral position (bottom right). Positions within this virtual cube are selected with three Java-based scrollbars placed at the edges of the frame display and along-track display, respectively. Java radio controls (bottom left) allow focusing the display on VNIR, SWIR, or both detectors. Two smaller data displays (middle right) show the number of saturated pixels per frame of the virtual cube split into SWIR and VNIR detectors, based on saturation data compiled during initial data loading. All further functions of the APEX CAL IS, such as calibration and analysis functions, are accessed via menu entries provided by the main window.

The virtual cube shown in Fig. 10 comprises 150 level-1 radiometric calibration frames acquired with five different radiance settings on a small integrating sphere illuminating the center of the FOV. The intensity steps can be easily discerned in the along-track profile (bottom right plot). The two last intensities exhibit saturation in both detectors as a result of

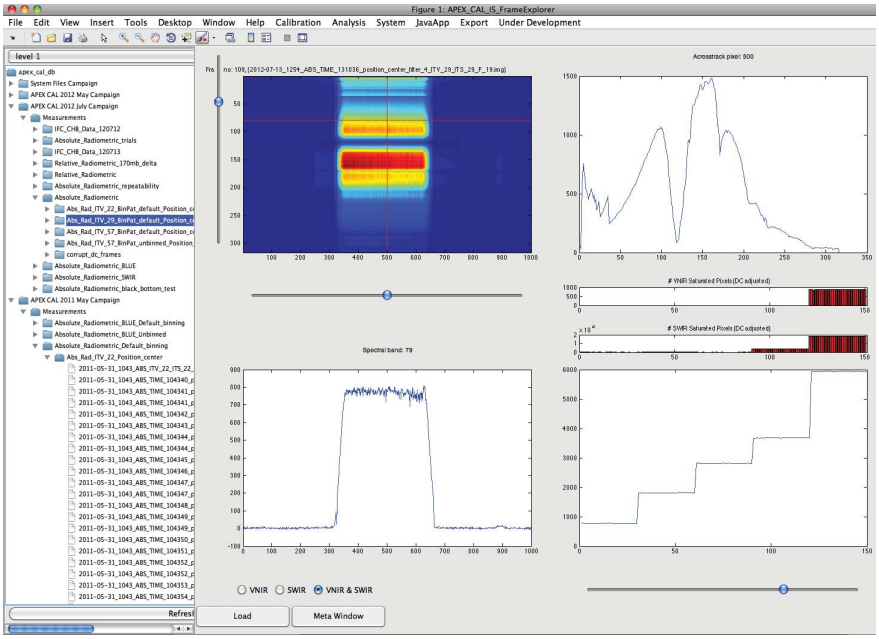

Fig. 10. MATLAB APEX CAL IS main interface.

too high an integration time for these radiance levels. These saturations are indicated in the GUI by the red bars in the two smaller displays (middle right).

VI. CASE STUDY

This section exemplifies the practical application of the APEX CAL IS by alluding to the spectral system calibration, which is rather data-intensive as well as particularly interesting from an algorithmic point of view. Goal of the spectral calibration is the definition of center wavelength and full-width at half-maximum (FWHM) parameters for all spatiospectral pixels of the system's detectors. The spectral calibration module must primarily deal with three problems: 1) processing of level-1 frames, amounting to 5.8 and 5.3 GB of standard spectral calibration data for VNIR and SWIR sensors, respectively; 2) extracting spectral response functions (SRFs) from these data at the sampled points and providing values for all pixels by suitable inter/extrapolation algorithms; and 3) enabling the user to interactively inspect each stage of the calibration layer generation. The spectral calibration is implemented generically and operates automated and independent of the selected spatiospectral sampling pattern, spectral binning pattern, and chosen monochromator sampling step size by relying on the detailed meta-data, minutely describing the acquisition and calibration instrument settings.

The overall processing time is largely governed by the loading of the data into the main memory of the client machine, and the generation of spectral calibration layers requires around a quarter of an hour per detector, which is acceptable as operationally performed only once or twice a year. Data loading is partitioned based on the sampling pattern and thus only a subset of the calibration data is loaded into memory at a time. Once extracted, the actually required data vectors and associated meta-data may be saved in intermediate files, typically taking a mere 300–500 kB of memory per detector.

Fig. 11 presents the GUI of the spectral calibration module. The displays show the following interactive information, essentially representing the extracted data for the VNIR detector (from left to right and top to bottom): (a) DN response of a selected illuminated pixel plotted versus the changing monochromator wavelength; (b) Gaussian curve fitted to the data points, used for the determination of center wavelength and FWHM; (c) spatiospectral sampling pattern with currently visualized sampling point indicated by red crosshairs; (d) center wavelength across-track profiles, i.e., equivalent to the spectral misregistration, for the measured spatial pixels at the currently selected spectral position; (e) extracted center wavelengths for selected spatial position; (f) first- and second-order statistics of center wavelength across-track profiles; (g) inter/extrapolating curve fitted to center wavelengths for the selected spatial position; and (h)–(k) similar data as in (d)–(g) but for the FWHM parameter.

Center wavelength and FWHM values are approximated for the whole detector by applying a spatial interpolation to the data points already interpolated in spectral dimension. These final layers are compiled into spectral calibration cubes per detector and stored in the database as calibration products, annotated with meta-data describing the parameterization of the calibration module as well as time and date of data

This article has been accepted for inclusion in a future issue of this journal. Content is final as presented, with the exception of pagination.

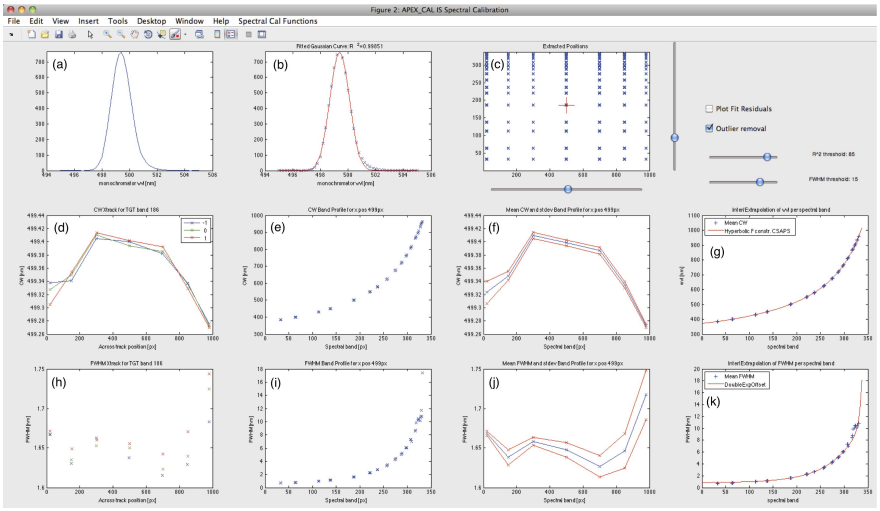

Fig. 11. Interface of the APEX CAL IS spectral calibration module, showing VNIR data.

acquisition and layer generation. At this point, it is readily available to the CAL IS to parameterize operations, such as spectral convolution, required during the radiometric calibration of the system.

VII. Discussion

In the following, we will discuss the selected architectures, namely the database schema and the interface software organized as layers using two programming languages, as these initial choices during system design have an impact on the scalability, flexibility, and speed of the final system, as well as on the implementation effort.

The choice of a flexible data schema, mainly based on the EAV paradigm, over a traditional database schema is a critical one, as it allows a very flexible approach to the handling of meta-data but, on the other hand, database performance may drop considerably as data sizes increase, the latter being one of the main criticisms of the EAV scheme. The flexibility of the system regarding frame-related meta-data could be proven, but careful analysis was needed when considering the modeling of the provenance. Including the provenance information into the EAV concept was initially considered, but the graph structure with processor and specific processing information would not easily fit into the EAV without a massive overhead of logic implemented in the data representation layer. Hence it was decided to add provenance as traditional relational structure, keeping the EAV representation as simple as possible. Data retrieval speed is a matter of the origin of data selection queries. Meta-data are queried extremely fast when starting from the primary datasets (entity-centric operation), while selecting frames based on their meta-data (attribute-centric operation) is more time consuming; this effect is in fact a well known property of EAV databases [31]. For the attribute-centric operation, a careful consideration of the SQL statements is required. Rewriting of queries during implementation to optimize them for the EAV case proved to be essential, sometimes improving the speed by a factor of 10 or more. It was also found that overly complex queries were better split into several consecutive queries, with intermediate results being cached in the EAV database connection and representation layer. An additional concept that proved useful in improving the speed while keeping database statements simple was the sorting or filtering by attributes or attribute values within the application code. The forming of queries as well as the post-query sorting/filtering in the application was implemented as generic as possible within the EAV database connection and representation layer, thus easing and abstracting the data access for the application layer. This strategy resulted in a massive implementation effort in the beginning of the project to code the generic database interface but made consecutive development of calibration specific modules within the application layer extremely efficient.

In hindsight, choosing the EAV paradigm over a traditional relational data model appears to have been the right choice. Data query speeds are time efficient and permit a fluent interaction between user and system, with a scenario dependant 19%–27% of the expected overall data volume already being loaded into the database. This performance is not expected to drop significantly and is in all cases not required to be near real time. Key to the system's performance during attribute-centric queries is the index definition on the values table with indices for eav_id, attribute_id, unit_id, as well as for the actual values. Besides that, most system queries are entity-centric operations with queries being applied to a frame subset and hence not prone to performance deficiencies. The main caveat is the implementation of efficient queries, which may require several iterations, especially while data sizes are

still to increase by several magnitudes. A major advantage of the EAV design proved to be the dynamic generation of new attributes, particularly during the evolution of data processing modules by effortlessly adding new parameters describing the chosen algorithmic configuration. Ultimately, the EAV design allows faster evolutionary development of data processing modules while providing thoroughly acceptable data access speeds for the involved data sizes, provided that queries are optimized for the EAV storage characteristics.

The combination of the programming languages Java and MATLAB proved to be a viable concept. Implementing the EAV database connection and representation layer in Java allowed the reuse of existing classes from the SPECCHIO spectral database project and in turn the addition of the new generic EAV capabilities to it with little overhead involved. The integration of Java within MATLAB was relatively flawless, given the good support of Java by MATLAB and the combination of Java and MATLAB GUI elements with the help of the JControl package in particular, as the latter allowed the development of much more flexible user interfaces than pure MATLAB would have offered. The overhead involved in the loading of frame data represented by serialized Java class instances stored in the database to in-memory instances via database queries and deserialization and the subsequent transfer of data as matrices into MATLAB turned out to be no hindrance as indicated by the loading time results presented, essentially not compromising the required interactive data exploration for databases hosted within the same physical network. Only the loading speed of data from databases via VPN connections may be prohibitive of interactive exploration, mainly caused by the massive amount of data that need transferring for larger frame collections. For these instances, running the application remotely on the server may be the preferred option.

The frame data representation in MATLAB was chosen as the default 64-bit floating point to avoid any conversions during subsequent floating point computations, but a different Java to MATLAB casting, e.g., to 16-bit integer for level-0 and level-1, could be easily added if an increase in the number of frames in memory would be critical. However, all analysis and calibration algorithms written to date have not met such limitations as data subsetting is applied when frame collections grow too big.

VIII. CONCLUSION

The APEX CAL IS is an effective system for the generic storage of imaging spectrometer calibration frame data and associated meta-data including provenance information. It provides a system layer for the database connection and data representation, allowing efficient data access for higher level application programs, such as various calibration and analysis tools whose description is beyond the scope of this paper. The main system components are a MySQL database with an EAV paradigm enabled schema, a system layer implemented in Java, and interactive interfaces written in MATLAB but using Java-based graphical and system layer components. The design was proven to cope very well with the expected amount of data, and its introduction into the APEX data processing environment resulted in a boost of sensor understanding, calibration to product cycle time, quality control, and repeatability of calibration coefficient estimation.

The rather generic nature of the system suggests that an adaptation to other pushbroom-based systems would be of little effort, requiring only the implementation of appropriate file reading routines for the data insert and the writing of higher level routines for the specific calibration routines required by the target system.

ACKNOWLEDGMENT

The authors would like to acknowledge the financial support by the Swiss Space Office during system design and implementation and the continuing support by EURAMET EMRP ENV-04. The EMRP is jointly funded by the EMRP participating countries within EURAMET and the European Union.

REFERENCES

[1] S. Ward, *The Earth Observation Handbook—Climate Change Special Edition 2008*. Noordwijk, The Netherlands: ESTEC, 2008.

[2] *The Second Report on the Adequacy of the Global Observing Systems for Climate in Support of the UNFCCC*, World Meteorological Organization (WMO), Geneva, Switzerland, 2003.

[3] M. E. Schaepman, S. L. Ustin, A. J. Plaza, T. H. Painter, J. Verrelst, and S. Liang, "Earth system science related imaging spectroscopy—an assessment," *Remote Sens. Environ.*, vol. 113, pp. S123–S137, Sep. 2009.

[4] *Earth Science and Applications from Space: National Imperatives for the Next Decade and Beyond*, National Research Council, Washington, DC, USA, 2007.

[5] J. S. Pearlman, P. S. Barry, C. C. Segal, J. Shepanski, D. Beiso, and S. L. Carman, "Hyperion, a space-based imaging spectrometer," *IEEE Trans. Geosci. Remote Sens.*, vol. 41, no. 6, pp. 1160–1173, Jun. 2003.

[6] M. J. Barnsley, J. J. Settle, M. A. Cutter, and F. Teston, "The PROBA/CHRIS mission: A low-cost smallsat for hyperspectral multi-angle observations of the earth surface and atmosphere," *IEEE Trans. Geosci. Remote Sens.*, vol. 42, no. 7, pp. 1512–1520, Jul. 2004.

[7] H. Kaufmann, K. Segl, S. Chabrillat, S. Hofer, T. Stuffler, and A. Mueller, "EnMAP a hyperspectral sensor for environmental mapping and analysis," in *Proc. IEEE Int. Conf. Geosci. Remote Sens. Symp.*, Jul.–Aug. 2006, pp. 1617–1619.

[8] D. Labate, M. Ceccherini, A. Cisbani, V. De Cosmo, C. Galeazzi, L. Giunti, M. Melozzi, S. Pieraccini, and M. Stagi, "The PRISMA payload optomechanical design, a high performance instrument for a new hyperspectral mission," *Acta Astron.*, vol. 65, pp. 1429–1436, Nov.–Dec. 2009.

[9] T. Stuffler, K. Forster, S. Hofer, M. Leipold, B. Sang, H. Kaufmann, B. Penne, A. Mueller, and C. Chlebek, "Hyperspectral imaging-an advanced instrument concept for the EnMAP mission (environmental mapping and analysis programme)," *Acta Astron.*, vol. 65, pp. 1107–1112, Oct.–Nov. 2009.

[10] T. Cocks, R. Jenssen, A. Stewart, I. Wilson, and T. Shields, "The HYMAP airborne hyperspectral sensor: The system, calibration and performance," in *Proc. 1st EARSEL Workshop Imag. Spectroscopy*, 1998, pp. 1–6.

[11] M. E. Schaepman, M. Jehle, A. Hueni, K. Meuleman, and K. I. Itten, "The 4th generation imaging spectrometer APEX and its application in earth observation," *IEEE Trans. Geosci. Remote Sens.*, 2013, to be published.

[12] R. O. Green, M. L. Eastwood, C. M. Sarture, T. G. Chrien, M. Aronsson, B. J. Chippendale, J. A. Faust, B. E. Pavri, C. J. Chovit, M. Solis, M. R. Olah, and O. Williams, "Imaging spectroscopy and the airborne visible/infrared imaging spectrometer (AVIRIS)," *Remote Sens. Environ.*, vol. 65, pp. 227–248, Jul. 1998.

[13] F. Lehmann, D. Oertel, R. Richter, P. Strobl, H. Rothfuß, A. Mueller, P. Hausknecht, S. Tischler, R. Mueller, D. Beran, J. Fries, R. Boehl, and P. Obermeier, "The digital airborne imaging spectrometer DAIS 7915," in *Proc. ISSSR Hyperspectral Appl. New Sensor*, 1995.

[14] H. Kostkowski, *Reliable Spectroradiometry*. La Plata, MA, USA: Spectroradiometry Consulting, 1997.
[15] E. J. Milton, M. E. Schaepman, K. Anderson, M. Kneubühler, and N. Fox, "Progress in field spectroscopy," *Remote Sens. Environ.*, vol. 113, pp. 92–109, Sep. 2009.
[16] P. Cox and D. Stephenson, "A changing climate for prediction," *Science*, vol. 317, no. 5835, pp. 207–208, 2007.
[17] N. Fox, J. Aiken, J. J. Barnett, X. Briottet, R. Carvell, C. Frohlich, S. B. Groom, O. Hagolle, J. D. Haigh, H. H. Kieffer, J. Lean, D. B. Pollock, T. Quinn, M. C. W. Sandford, M. Schaepman, K. P. Shine, W. K. Schmutz, P. M. Teillet, K. J. Thome, M. M. Verstraete, and E. Zalewski, "Traceable radiometry underpinning terrestrial- and heliostudies (TRUTHS)," *Adv. Space Res.*, vol. 32, no. 11, pp. 2253–2261, 2003.
[18] R. L. Ackoff, "From data to wisdom," *J. Appl. Syst. Anal.*, vol. 16, no. 1, pp. 3–9, 1989.
[19] S. Kempler, C. Lynnes, B. Vollmer, G. Alcott, and S. Berrick, "Evolution of information management at the GSFC earth sciences (GES) data and information services center (DISC): 2006–2007," *IEEE Trans. Geosci. Remote Sens.*, vol. 47, no. 1, pp. 21–28, Jan. 2009.
[20] L. Floridi, "On defining library and information science as applied philosophy of information," *Soc. Epistemol.*, vol. 16, no. 1, pp. 37–49, 2002.
[21] L. Floridi, "Understanding epistemic relevance," *Erkenntnis*, vol. 69, no. 1, pp. 69–92, 2008.
[22] J. Rowley, "The wisdom hierarchy: Representations of the DIKW hierarchy," *J. Inf. Sci.*, vol. 33, no. 2, pp. 163–180, 2007.
[23] C. W. Choo, "The knowing organization: How organizations use information to construct meaning, create knowledge and make decisions," *Int. J. Inf. Manage.*, vol. 16, no. 5, pp. 329–340, 1996.
[24] D. Chaffey and S. Wood, *Business Information Management: Improving Performance Using Information Systems*. Englewood Cliffs, NJ, USA: Prentice-Hall, 2005.
[25] A. Hueni, J. Biesemans, K. Meuleman, F. Dell'endice, D. Schläpfer, S. Adriaensen, S. Kempenaers, D. Odermatt, M. Kneubuehler, J. Nieke, and K. Itten, "Structure, components and interfaces of the airborne prism experiment (APEX) processing and archiving facility," *IEEE Trans. Geosci. Remote Sens.*, vol. 47, no. 1, pp. 29–43, Jan. 2009.
[26] P. Gege, J. Fries, P. Haschberger, P. Schötz, H. Schwarzer, P. Strobl, B. Suhr, G. Ulbrich, and W. J. Vreeling, "Calibration facility for airborne imaging spectrometers," *ISPRS J. Photogram. Remote Sens.*, vol. 64, pp. 387–397, 2009.
[27] M. Ecker, "Automatisierung einer optoelektronischen kalibriereinrichtung," M.S. thesis, Dept. Appl. Sci., Landshut Univ., Landshut, Germany, 2007.
[28] T. D. Wason and D. Wiley, "Structured metadata spaces," *J. Internet Catalog.*, vol. 3, nos. 2–3, pp. 263–277, 2000.
[29] D. Bernholdt, S. Bharathi, D. Brown, K. Chanchio, M. Chen, A. Chervenak, L. Cinquini, B. Drach, I. Foster, P. Fox, J. Garcia, C. Kesselman, R. Markel, V. Nefedova, L. Pouchard, A. Shoshani, A. Sim, G. Strand, and D. Williams, "The earth system grid: Supporting the next generation of climate modeling research," *Proc. IEEE*, vol. 93, no. 3, pp. 485–495, Mar. 2005.
[30] P. Nadkarni, L. Marenco, R. Chen, E. Skoufos, G. Shepherd, and P. Miller, "Organization of heterogeneous scientific data using the EAV/CR representation," *J. Amer. Med. Informat. Assoc.*, vol. 6, no. 6, pp. 478–493, 1999.
[31] V. Dinu and P. Nadkarni, "Guidelines for the effective use of entity-attribute-value modeling for biomedical databases," *Int. J. Med. Informat.*, vol. 76, nos. 11–12, pp. 769–779, 2007.
[32] H. Arndt, M. Bundschus, and A. Naegele, "Toward a next-generation matrix library for java," in *Proc. 33rd Annu. IEEE Int. Computer Softw. Appl. Conf.*, Jul. 2009, pp. 460–467.
[33] A. Hueni, J. Nieke, J. Schopfer, M. Kneubühler, and K. Itten, "The spectral database SPECCHIO for improved long term usability and data sharing," *Comput. Geosci.*, vol. 35, no. 3, pp. 557–565, 2009.
[34] M. Lidierth, "sigTOOL: A MATLAB-based environment for sharing laboratory-developed software to analyze biological signals," *J. Neurosci. Methods*, vol. 178, no. 1, pp. 188–196, 2009.

Andreas Hueni (M'12) received the B.Sc. degree in computer science from the University of Applied Science Brugg-Windisch, Brugg-Windisch, Switzerland, in 1997, the PG Diploma degree in geographic information systems, and the M.Phil.(Sc) degree in earth science from Massey University, Palmerston North, New Zealand, in 2005 and 2006 respectively, and the Ph.D. degree in geography from the University of Zurich, Zurich, Switzerland, in 2011.

He is currently a Post-Doctoral Researcher with the Remote Sensing Laboratories, University of Zurich, where he is involved in research on APEX sensor and data calibration. He was involved in research for the APEX project in 2007. His current research interests include calibration of spectrometers and design of combined databases and software systems such as spectral database SPECCHIO.

Karim Lenhard received the Diploma degree in physics from the University of Bonn, Bonn, Germany, in 2008, where he is currently pursuing the Ph.D. degree with the German Aerospace Center (DLR).

He is currently a Researcher with DLR where he is engaged in operating and improving the APEX calibration home base, an optical laboratory for calibration, and characterization of airborne hyperspectral imagers. His current research interests include spectral and radiometric calibration of hyperspectral instruments.

Andreas Baumgartner received the B.Eng. degree in mechatronics specialized in optical engineering and the M.Eng. degree in electrical engineering and information technology from the University of Applied Sciences Deggendorf, Deggendorf, Germany, in 2008 and 2010, respectively.

He is currently with the German Aerospace Center where he is engaged in calibration home base of APEX. His current research interests include improving setup, methods, and software for spectral, geometric, and radiometric calibration of imaging spectrometers.

Michael E. Schaepman (M'05–SM'07) received the M.Sc. and Ph.D. degrees in geography from the University of Zürich (UZH), Zürich, Switzerland, in 1993 and 1998, respectively.

He is currently the Head of the Remote Sensing Laboratories, Department of Geography, UZH, where he joined as a Full Chair of remote sensing in 2009. In 1999, he was a Post-Doctoral Researcher with the Optical Sciences Center, The University of Arizona, Tucson, USA. In 2000, he was a Project Manager with the European Space Agency Airborne Prism Experiment spectrometer. In 2003, he was a Full Chair of geoinformation science and remote sensing with Wageningen University, Wageningen, The Netherlands. His current research interests include computational Earth sciences using remote sensing and physical models, particularly land-atmosphere interface using imaging spectroscopy.

Chapter 6

Determination of combined measurement uncertainty via Monte Carlo analysis for the imaging spectrometer ROSIS

This chapter has been published as: Lenhard, K. (2012). Determination of combined measurement uncertainty via Monte Carlo analysis for the imaging spectrometer ROSIS. Applied optics

Determination of combined measurement uncertainty via Monte Carlo analysis for the imaging spectrometer ROSIS

Karim Lenhard

Deutsches Zentrum für Luft- und Raumfahrt (DLR), Institut für Methodik der Fernerkundung (IMF), 82234 Oberpfaffenhofen, Germany (karim.lenhard@dlr.de)

Received 5 January 2012; revised 3 April 2012; accepted 13 April 2012; posted 13 April 2012 (Doc. ID 160949); published 13 June 2012

To enable traceability of imaging spectrometer data, the associated measurement uncertainties have to be provided reliably. Here a new tool for a Monte-Carlo-type measurement uncertainty propagation for the uncertainties that originate from the spectrometer itself is described. For this, an instrument model of the imaging spectrometer ROSIS is used. Combined uncertainties are then derived for radiometrically and spectrally calibrated data using a synthetic at-sensor radiance spectrum as input. By coupling this new software tool with an inverse modeling program, the measurement uncertainties are propagated for an exemplary water data product.

OCIS codes: 120.0280, 120.3940, 280.4788.

1. Introduction

The goal of this paper is to present the use of Monte Carlo analysis for the propagation of measurement uncertainties of radiometrically and spectrally calibrated imaging spectrometer data as well as their impact on retrieved model parameters of an exemplary application. The indication of measurement uncertainties for scientifically used data is necessary to allow for an estimation the uncertainty of subsequent analyses of the taken data and to enable comparability of data between different sensors. This method was implemented into a software tool called PyROSIS.

The need for the indication of measurement uncertainties has been recognized by the hyperspectral remote sensing community [1]. Therefore, traceability to the Systeme International units of the spectral radiance data recorded by imaging spectroradiometers is increasingly a requirement, e.g., [2].

According to metrological guidelines [3], propagation of measurement uncertainties should be performed numerically using a Monte Carlo method (MCM) if an analytical error propagation is not feasible. This is the case for imaging spectrometer data, since, for example, radiometric uncertainties introduced through spectral uncertainties cannot be determined analytically, as they depend on the object spectra [4]. Also, some data processing procedures performed to process raw data [Level 0 (L0) data] to radiometrically and spectrally calibrated data [Level 1 (L1) data] cannot be modeled for an analytical error propagation, such as geometric or spectral resampling or stray light correction.

Since the uncertainties depend on the instrument, this simulation is based on the implementation of a specific sensor. For this study, Deutsches Zentrum für Luft- und Raumfahrt's (DLR's) imaging spectrometer ROSIS was chosen, as laboratory and airborne characterization data were readily available. These data are used for the calibration as well as for the generation of the sensor model for the simulation. Also, the L1-calibration software, which needs to

1559-128X/12/184065-08$15.00/0

be included in the Monte Carlo simulation, was available.

The input spectra that are used to generate at-sensor radiances in this simulation are synthetic: a water reflectance spectrum was generated and propagated through the atmosphere to simulate at-sensor radiances across the field of view. The water reflectance was generated by the software WASI [5].

By coupling PyROSIS with WASI into one workflow, the L1 data that are generated in this simulation can be used to estimate the instrument's influence on the uncertainties of the retrieved parameters of the radiative transfer model. This is shown here exemplarily for the determination of suspended matter concentration by inverse modeling using WASI.

The focus of this paper is on radiometric and spectral uncertainties; uncertainties introduced via geometric properties such as finite line spread functions (i.e., imaging of multiple objects within one pixel) or movement smearing are not considered here. These are studied in more detail in, e.g., [6]. Hence, the simulated scene used for this study is chosen to be homogeneous. Also, the uncertainties introduced through atmospheric and geometric correction are not included in this analysis, as this also was studied previously, for instance in [1,7].

This paper is organized as follows. Section 2 gives a brief recapitulation of how Monte Carlo analyses are used to determine measurement uncertainties, Section 3 presents the implementation of such an analysis into software, and Section 4 introduces the instrument model used in this study. Results obtained with the Monte Carlo analysis are presented in Section 5 and commented on in Section 6.

2. Determination of Measurement Uncertainties via the MCM

To describe the measurement uncertainties, a probability density function (PDF) or a probability distribution is assigned to each sensor and model parameter (see Section 4). After that, an MCM analysis is performed as follows.

- Select the number N of hyperspectral frames to be simulated.
- For each run of the simulation, i.e., each frame, draw a random value from each parameter's PDF and perform a forward calculation with those values to simulate the data acquisition process, the calibration, and subsequent processing steps.
- Repeat this N times to build the PDFs of the at-sensor radiance.
- Determine the shortest 95% coverage intervals.

The shortest 95% coverage interval is the smallest interval that contains 95% of the radiance values of a detector element. Reference [3] recommends the use of shortest coverage intervals in case of potentially asymmetric and *a priori* unknown PDFs of the results. For a Gaussian PDF, this corresponds to a coverage factor of $k = 2$, meaning 2 standard deviations.

Each run of the simulation by PyROSIS consists of the following steps.

- Simulate the image acquisition process using the instrument model for a given remote sensing reflectance spectrum at a well-defined viewing and illumination geometry and atmospheric conditions. This corresponds to the creation of a synthetic hyperspectral frame, which includes all spectral information of one image line, i.e., all the information collected by the instrument during one sampling; the units of the data being digital numbers (DNs).
- Perform L0 to L1 calibration. The data are now in the units of spectral radiances.
- Correct for atmosphere and illumination. The data now have the units of normalized water leaving remote sensing reflectance.
- Further analysis of the reflectance data through inverse modeling using WASI.

The hyperspectral frame is defined here as one image row of the hyperspectral cube, i.e., one spectrum for each geometric pixel.

3. Implementation of the Method

A. Work Flow

The first step is to create a hyperspectral frame, i.e., one spectrum for each geometric pixel using a simulated at-sensor radiance spectrum. This corresponds to the imaging of a completely homogeneous scene during a flight.

The second step consists in the calibration of this frame, so that one ends up with radiance spectra.

The calibrated spectra are atmospherically corrected and finally handed over to WASI to retrieve the suspended matter concentration, C_L.

B. Generation of Synthetic Imaging Spectrometer Frame

In the following, the generation of an imaging spectrometer frame is described. Some of the processing steps are explained in more detail in Subsection 3.C.

First, an at-sensor radiance spectrum L is calculated as follows:

$$L(\lambda) = R_{\mathrm{RS}}(\lambda) \cdot T_{\mathrm{atm}}(\lambda) \cdot E_0(\lambda) \cdot T_{\mathrm{window}}(\lambda) + L_{\mathrm{path}}(\lambda). \tag{1}$$

In this equation, R_{RS} denotes the water remote sensing reflectance, T_{atm} an atmospheric transmission generated with MODTRAN [8], E_0 the extraterrestrial solar irradiance [9], T_{window} the transmission of the airplane window, and L_{path} the path radiance. All input spectra have a higher resolution ($\Delta\lambda \approx 1$ nm) than the simulated instrument (for ROSIS, $\Delta\lambda \approx 6$ nm). T_{atm} is the product of the atmospheric transmission of the downwelling irradiance reaching the surface $T_{\mathrm{atm}}^{\mathrm{down}}$ and the atmospheric transmission of the upwelling radiance between water surface and sensor $T_{\mathrm{atm}}^{\mathrm{up}}$.

In the following, S denotes a sensor signal in the units of DN. The index i denotes spectral channels, the index j denotes geometric pixels. For the sake of readability, some equations take the form of matrix equations, where variables that are subscripted with only one index are to be understood as a vector; i.e., S_j is a vector containing the spectral information recorded by the geometric pixel number j. Matrices are in bold typeface.

For each geometric pixel, the radiance impinging each channel is then calculated by integrating the product of the spectral response function (SRF) $\mathrm{SRF}(\lambda)$ with the at-sensor radiance spectrum, thus yielding a radiance spectrum L_{LR} with lower resolution:

$$L_{\mathrm{LR},i,j} = \int \mathrm{SRF}(\lambda)_{i,j} \cdot L(\lambda) \mathrm{d}\lambda. \tag{2}$$

The center wavelengths of the detector element's SRF are calculated according to Section 4. An error due to polarization sensitivity is introduced multiplicatively:

$$L_{\mathrm{LR,Pol},i,j} = L_{\mathrm{LR},i,j}(1 + P \cdot U(\phi, i)), \tag{3}$$

$P = 30\%$ being a typical degree of polarization due to the reflection on water and U being the probability distribution described in Eq. (14).

Subsequently, the photoresponse nonuniformity (PRNU) is introduced. This is done by multiplying the signal of each detector element with the inverse of its PRNU correction factor, U_{PRNU}.

Then, the radiances are converted into DN:

$$S_{i,j} = L_{\mathrm{LR,Pol},i,j} \cdot r_{i,j} \cdot t_{\mathrm{exposure}}, \tag{4}$$

where the radiometric response coefficients are computed according to the following equation:

$$r_j = \frac{1}{L_{\mathrm{IS}} \cdot t_{\mathrm{exposure}}} \cdot \boldsymbol{M} \cdot \left(\frac{S_{\mathrm{IS},j}}{U_{\mathrm{PRNU},j}} - S_{\mathrm{smear},j} \right). \tag{5}$$

The radiometric response coefficients $r_{i,j}$ depend on wavelength and pixel number. S_{IS} is the signal measured by the sensor of an integrating sphere, L_{IS} is the spectral radiance of that sphere, and t_{exposure} is the exposure time. The signal is corrected for PRNU (U_{PRNU}), smear (S_{smear}), stray light using the current stray light distribution, $\boldsymbol{M}$, and smile via resampling to the reference wavelengths. A stray light distribution matrix $\boldsymbol{M}$ is generated for each run using Eq. (11).

The effects taken into account for the calculation of r have to be applied to S as well to simulate L0 data: spectral stray light is added by multiplying each pixels' spectrum with the inverse of the correction matrix. Readout smearing is added using Eq. (15). The dark current signal as well as its associated uncertainty are then added to the signal. The radiometric noise is generated using Eq. (12) and added. Detector saturation is introduced by setting signals above the detectors' maximal signal level to its maximal signal level. Finally, quantization errors are introduced to the data by rounding the signals to the next integer number. A more detailed description of these effects is given in Section 4.

C. L1 Calibration

The L1 calibration for synthetic data uses the same procedure as the regular L1 calibration process, the difference being that calibration errors are added here. The calibration steps performed are, in the same order as presented here, starting with the signals S generated according to Subsection 3.B:

The dark current is subtracted. Then, the PRNU is corrected by multiplying the signal of each detector element with its individual PRNU correction factor. The signal due to smearing is corrected for by calculating it with Eq. (15) and subtracting it from the signal. The stray light signals are removed according to Section 4. To correct for the spectral misregistration due to smile, all spectra are resampled to a single, defined set of center wavelengths using cubic spline interpolation. Finally, the resulting signal of each detector element $S'_{i,j}$ is multiplied with the detector element's radiometric response

$$L_{i,j} = \frac{S'_{i,j}}{r_{i,j} \cdot t_{\mathrm{exposure}}}, \tag{6}$$

so that the data are now radiometrically calibrated and in the units of spectral radiance.

D. Level 2 Processing

To allow further analyses, the L1 calibrated data have to be processed to Level 2; i.e., the spectral radiance has to be atmospherically corrected so that the at-sensor radiances are converted into ground reflectances. As the atmospheric contribution is completely known in these simulations, this is an idealized correction. This is done via

$$R_{\mathrm{RS}} = \frac{L(\lambda) - L_{\mathrm{path,LR}}(\lambda)}{E_{0,\mathrm{LR}}(\lambda) \cdot T_{\mathrm{atm,LR}}(\lambda) \cdot T_{\mathrm{window,LR}}(\lambda)}, \tag{7}$$

where the denominator, the combined spectrum of the Sun, the atmosphere, and the aircraft window transmission as well as the path radiance are resampled to the lower resolution of ROSIS, as indicated by the subscript "LR."

E. Generation of Level 3 Data

The "Water Colour Simulator" WASI [5] is a software tool that, in its forward mode, is capable of the calculation of optical water spectra based on physical models. In its inverse mode, WASI allows for the inversion of water spectra for the retrieval of water model parameters.

WASI was used in its forward more to generate the remote sensing reflectance spectrum used for the

simulation. Therefore, all input parameters for the generation of this spectrum are known. For this study, only the suspended matter concentration C_L was retrieved. Since this is done for each simulated spectrum of each simulated sensor frame, a combined measurement uncertainty can be determined for the retrieval of C_L by again using the shortest 95% coverage interval for all the resulting values of C_L as a measure for the uncertainty.

F. Software Tool PyROSIS

The L1 calibration software and the Monte Carlo simulation tool were implemented in Python, using the NumPy and SciPy libraries.

The sensor model description is based on text files, so the implementation of other instruments should be relatively simple. On an Intel i5 notebook processor with 2.67 GHz, the calculation of a single frame on one core takes about 30 s. Since the task is easily parallelized, the software can make use of multiple processor cores.

4. ROSIS Sensor Model

The term "sensor model" is used here in the sense that it is a mathematical description of an imaging spectrometer. All values given here are derived from the available, although partly unpublished, data and are based on laboratory and airborne measurements. As the scope of this publication does not encompass the actual characterization of ROSIS, the derivation of those values is not described here in more detail.

ROSIS [10,11] is a grating-based imaging spectrometer that has been used in three different configurations since 1991. The current configuration, ROSIS 3, has 512 geometric pixels, 115 spectral channels, 103 of which are usable for airborne measurements, and a radiometric resolution of 14 bits. The remaining 12 channels are blocked by an optical filter. ROSIS covers the wavelength range from 430 to 836 nm. Table 1 provides an overview of the sensor parameters and their uncertainties, which are used to model the measurement uncertainties of ROSIS.

Table 1. ROSIS Sensor Parameters Used for MCM with Their Associated Uncertainties[a]

Parameter	Mean Value	Uncertainty	PDF
Center wavelength	see Eq. 8	0.2 nm	Gaussian
FWHM of SRF	6 nm	0.1 nm	Gaussian
Spectral sampling interval	4 nm	0.01 nm	Gaussian
Radiometric response	From table	1%	Gaussian
Aircraft window transmission	From table	1.5%	Uniform
Polarization sensitivity	see Eq. 13	see Eq. 14	Arc sine
Dark current	900 DN	0.6 DN	Gaussian
Spectral stray light	see Eq. 11	5%	Gaussian
PRNU	From table	0.5%	Gaussian
Radiometric noise	0	see Eq. 12	Gaussian

[a]Gaussian uncertainties are given for $k = 1$. Some parameters and uncertainties are defined through the referenced equations. "From table" refers to the look-up tables in which the measurement data are stored.

The following are parameters of the sensor model.

SRFs. The SRF of a ROSIS channel is Gaussian in shape, with a FWHM of $\lambda_{\mathrm{FWHM}} = 6$ nm and an uncertainty of $\Delta\lambda_{\mathrm{FWHM}} = 0.1$ nm. The spectral sampling interval (SSI) between two adjacent channels is $\lambda_{\mathrm{SSI}} = 4$ nm, with an uncertainty of $\Delta\lambda_{\mathrm{SSI}} = 0.01$ nm. The central wavelength $\lambda_{c,i}$ of a channel i has a stability of $\Delta\lambda_c = 0.2$ nm during a flight strip. All three uncertainties are modeled with Gaussian PDFs.

The spectral smile effect is also taken into account by introducing a pixel-number-dependent spectral shift to all λ_c of each geometric pixel. The introduced shifts are up to 1.5 nm and follow a parabolic function. The uncertainty of the smile shift is set to be zero, since the smile can be accurately measured in the laboratory and the remaining uncertainty corresponds to the uncertainty in center wavelength position.

The center wavelengths are computed as follows:

$$\lambda_{c,i,j} = 380\ \mathrm{nm} + \lambda_{\mathrm{SSI}} \cdot i - \lambda_{\mathrm{smile},j}, \tag{8}$$

with the smile shift relative to pixel $j = 0$ being parametrized as

$$\lambda_{\mathrm{smile},j} = (-9.52 \cdot 10^{-6} j^2 + 6.48 \cdot 10^{-3} j)\ \mathrm{nm}. \tag{9}$$

Spectral stray light. Spectral stray light can be understood as optical cross talk: Detector elements "see" light of wavelengths that should impinge on other spectral channels. A spectral stray light correction algorithm is described in [12], and the corresponding measurements are described in [13]. The stray light distribution can be condensed into a matrix $\boldsymbol{M}$, such that the equation

$$S_{\mathrm{meas},j} = \boldsymbol{M} \cdot S_{\mathrm{in},j} \tag{10}$$

holds. S_{in} is a vector with the spectrum that would be recorded without stray light influence, while the vector S_{meas} is the spectrum actually recorded by the pixel j of the instrument. The same matrix is applied to all geometric pixels. This approach only accounts for stray light that has its origin in the covered wavelength interval; stray light that originates from outside this interval is neglected.

The stray light matrix is generated from a parametrization of the stray light in ROSIS:

$$\boldsymbol{M}_{k,k_0} = \frac{a}{b(k-k_0)^2+1} + \frac{c}{d(k-k_0)^4+1} + h, \tag{11}$$

with $a = 8.43 \cdot 10^{-4}$, $b = 9.83 \cdot 10^{-4}$, $c = -2.56 \cdot 10^{-4}$, $d = -5.58 \cdot 10^{-4}$, and $h = 7.56 \cdot 10^{-5}$. k denotes the channel that receives stray light from the channel k_0. The PDF for each parameter is chosen to be Gaussian in shape, with a width of 5%.

Radiometric response. ROSIS' calibration standard is an integrating sphere calibrated at the German National Metrology Institute (PTB). In the

relevant part of the spectrum, the sphere's emitted spectral radiance uncertainty is given as $\sigma_L = 1\%$, with a Gaussian PDF. No radiometric nonlinearities were introduced as these can be neglected for the studied sensor.

PRNU. PRNU measurements were made before the focal plane array was built into the instrument with a homogeneous light source. The uncertainty is $\sigma_{\mathrm{PRNU}} = 0.5\%$, with a Gaussian PDF. For both PRNU correction and radiometric calibration, the actual radiometric reference files are used here.

Mean dark current level. The mean dark current level has an uncertainty of $\sigma_{\mathrm{D.C.}} = 0.6$ DN during a flight strip and follows a Gaussian distribution. For the simulation, a dark current signal level of 900 DN is used. The uncertainty $\sigma_{\mathrm{D.C.}}$ is added as a constant offset to all detector elements.

Radiometric noise. The radiometric noise of the instrument has a Gaussian PDF, its width σ_{noise} given by the functional relationship

$$\sigma_{\mathrm{noise}} = (12.38 + 0.001743 \cdot S)\ \mathrm{DN}, \tag{12}$$

which is a parametrization of the noise levels measured in ROSIS. All noise sources, i.e., dark current noise, noise from the readout electronics, and photon noise, are included here. Unlike $\sigma_{\mathrm{D.C.}}$, the noise function is applied to all pixels individually.

Aircraft window transmission. Transmission measurements were performed with two laboratory spectrophotometers. A comparison of the results of the two spectrophotometers yields a wavelength-independent measurement uncertainty with a uniform PDF with a width of 1.5%.

Polarization sensitivity. The sensitivity to linear polarization is modeled to increase linearly from 5% at shorter wavelengths to 15% at longer wavelengths over the spectral range of the instrument; i.e., the polarization sensitivity p_i of a channel i is given by

$$p_i = 8.7 \cdot 10^{-4} i + 0.05. \tag{13}$$

The distribution function

$$U(\phi, i) = \frac{p_i}{2} + \frac{p_i}{2}\ \sin(\phi) \tag{14}$$

is used to model the uncertainty of the polarization of the incident light. According to [3], this is the probability distribution for sinusoidally varying quantities with an unknown phase ϕ.

Readout smearing. ROSIS does not have a shutter, and the readout of the CCD detector array is done in the frame transfer mode. Thus, the smear signal $S_{\mathrm{smear},j}$ of each pixel j is calculated with the following equation:

$$S_{\mathrm{smear},j} = \sum_{i=1}^{115} S_{i,j} \cdot \frac{t_{\mathrm{smear}}}{t_{\mathrm{exposure}}}, \tag{15}$$

with $t_{\mathrm{smear}} = 1.8 \cdot 10^{-6}$ s as the readout time and $t_{\mathrm{exposure}} = 1/40$ s as the exposure time.

Note that, except for the radiometric noise, the uncertainties are introduced so that no additional noise is generated; e.g., the entire radiometric response array is varied scalarly within the values given in Table 1, meaning that the radiometric calibration array used in a run of the MCM $\boldsymbol{r}$ is the product of the reference radiometric calibration array $\boldsymbol{r}_{\mathrm{ref}}$ and a random scalar z.

5. Results

PyROSIS can be used to calculate traceable measurement uncertainties for radiometrically calibrated data and their derived data products as well as to perform sensitivity analyses to relate the uncertainties of sensor parameters to the uncertainties in the product of interest. Examples for this are presented in this section.

A. Number of Runs

The number of runs to be repeated to get an accurate estimate of the uncertainty has to be determined. For Fig. 1, 1000 frames were calculated, and the standard deviation for the signal level of the detector at pixel 300, channel 90 was computed using an increasing number of frames. The standard deviation settles quickly to a value of about 0.53 mW/($\mathrm{m}^2 \cdot \mathrm{sr} \cdot \mathrm{nm}$), with variations not larger than 3% of that value. For the reason of economy of time, a lower number of frames, 200, is generated for the plots in the following sections. Because of the long computation times, the total number of runs is well below the required number to build a good approximation of the output PDF but is still in accordance with [3], as this approach allows for a uncertainty estimation in finite time and this accuracy is sufficient for the presentation of this method.

B. Tests of the Sensor Simulation

A test case for the sensor simulation is shown in Fig. 2: a laboratory L0 spectrum, generated by

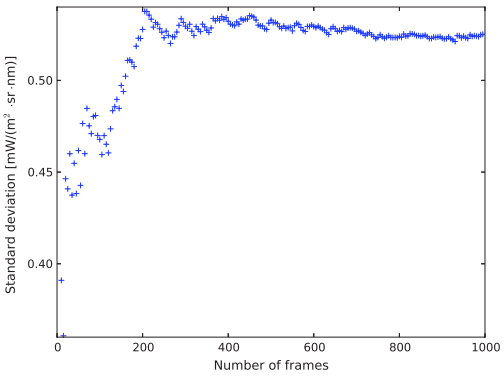

Fig. 1. (Color online) Standard deviation of the signal of one detector element depending on how many Monte Carlo frames are used.

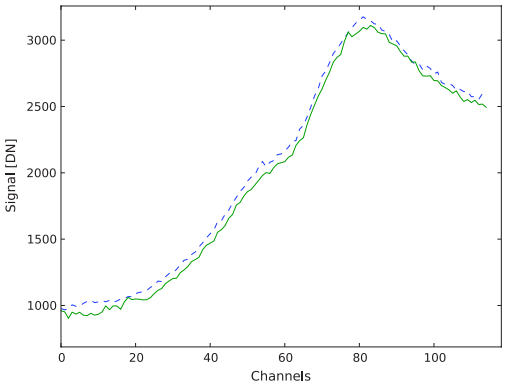

Fig. 2. (Color online) Comparison of two L0 spectra—one simulated from the calibration data and our integrating sphere (solid line) and one from a laboratory measurement of the same sphere (dashed line).

illuminating the instrument with an integrating sphere, is compared to an L0 spectrum simulated with PyROSIS using the sphere's radiance spectrum. The differences between both spectra can be attributed to the difference in mean dark current level, noise, and change in the radiance of the sphere between the measurement of the spectrum used for simulation and the actual measurement of the sphere with ROSIS.

A second test is illustrated with Fig. 3: the reflectance input spectrum is compared to the reflectance obtained after simulation. As expected, the spectrum generated by the full simulation differs mostly by the noise contribution.

C. Traceable Measurement Uncertainties on Radiance Data

A major purpose of the software is to calculate measurement uncertainties for given spectra. An example is shown in Figs. 4 and 5. The continuous curve in

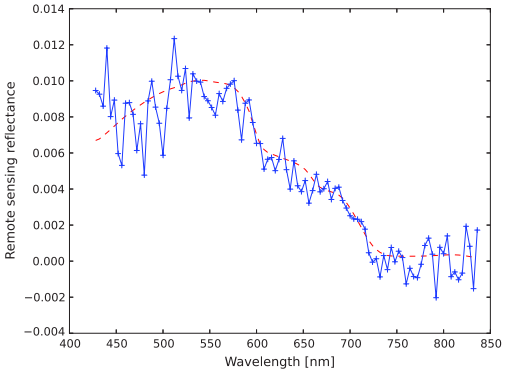

Fig. 3. (Color online) Comparison between the input reflectance spectrum generated by WASI (dashed line) and a retrieved spectrum calculated with all error sources (+ symbols).

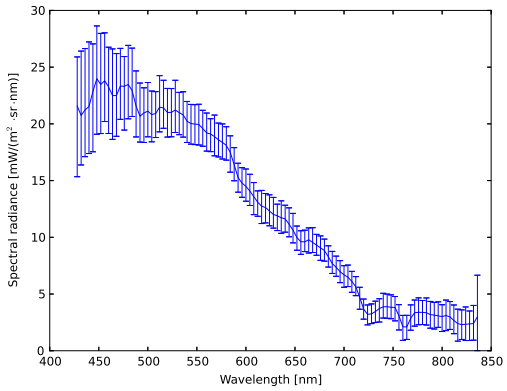

Fig. 4. (Color online) Mean calibrated spectrum with error bars defined through 95% coverage interval ($k = 2$).

Fig. 5 shows half of the error bars width shown in Fig. 4 divided by the actual value, corresponding to a relative uncertainty for $k = 2$.

For the given radiance levels, as shown in Fig. 5, the combined uncertainty is between 10% and 120% for $k = 2$. This is much larger than the radiometric calibration uncertainty of 2% that was set for the simulation. The increase of the measurement uncertainties for wavelengths smaller than 500 nm depicted in Fig. 5 is concordant with experience with ROSIS and can be explained with a low sensitivity of the instrument and the low radiance levels of the calibration source in that wavelength range. The increase of the combined uncertainty above 700 nm can be explained by the very low reflectance of water and the low level of path radiance.

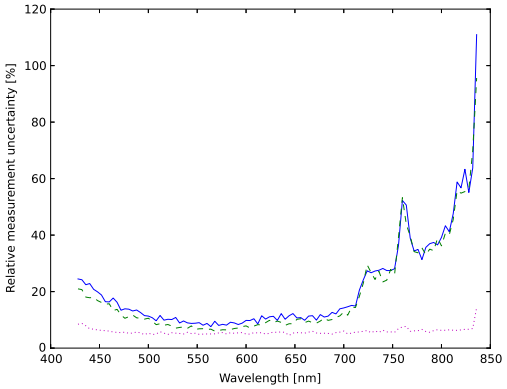

Fig. 5. (Color online) Combined measurement uncertainty for $k = 2$ for the spectral radiance data. The solid curve describes the uncertainties given all effects, the dashed curve the uncertainty obtained if only noise is an uncertainty source in the simulation, and the dotted curve the contributions of all other effects together.

D. Influence of Instrument Parameters

Further results are visible in Fig. 5, which shows the combined uncertainty for three different cases: all contributing effects are accounted for, all effects except the radiometric noise are considered, and only radiometric noise contributing to the uncertainty.

Figure 5 clearly illustrates that, for this kind of target, i.e., a water surface of low reflectance, particularly at wavelengths above 700 nm, radiometric noise is the dominating source of measurement uncertainty. Therefore, a more detailed breakdown of the uncertainty contributions of the other sensor model parameters was not studied further, as reduced calibration uncertainties would not improve the overall data quality.

E. End-to-End Simulation with PyROSIS and WASI

1. *Retrieval of C_L*

The simulated signal and uncertainties using PyROSIS can be used for the study of the measurement uncertainties of products derived from sensor data. After converting the simulated radiances into reflectances as described in Subsection 3.D, the simulated results from PyROSIS are used to calculate the uncertainties of a product, the suspended matter concentration C_L. This was done by performing a retrieval of C_L with WASI for a specific geometric pixel of each frame generated in the Monte Carlo simulation.

Figure 6 shows the relative uncertainties for the three described uncertainty models for the simulated reflectances obtained after the removal of atmospheric contributions to the spectra. The combined uncertainty of the data is of the order of 40% to 100% ($k = 2$). Again, the combined uncertainty is dominated by the noise contribution.

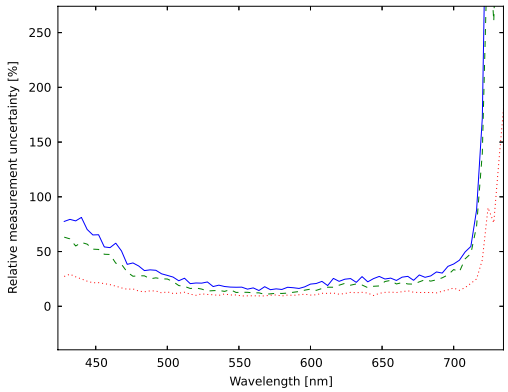

Fig. 6. (Color online) Combined measurement uncertainty for $k = 2$ for the remote sensing reflectance data. The solid curve describes the uncertainties given all effects, the dashed curve the uncertainty obtained if only noise is an uncertainty source in the simulation, and the dotted curve the contributions of all other effects together. The relative uncertainties for wavelengths greater 700 nm are not a reliable measure as the remote sensing reflectance is almost zero in all analyzed spectra.

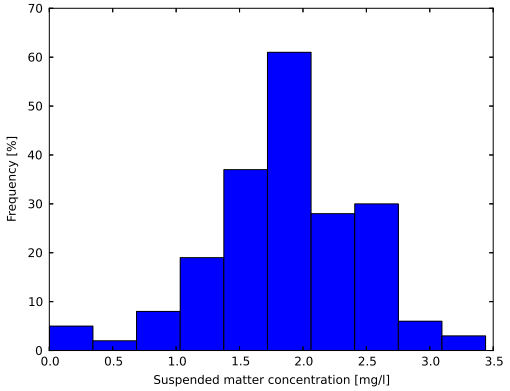

Fig. 7. (Color online) Histogram of the retrieved suspended matter concentrations. Actual concentration, $C_L = 2$ mg/l

The resulting distribution of C_L, derived from a pixel near the center of the detector array, is shown in the histogram in Fig. 7. The retrieved concentration of $C_L = 1.8 \pm 1.2$ ($k = 2$) shows the large influence of the sensor uncertainties on the retrieval.

2. *Influence of Stray Light Correction of C_L Retrieval*

PyROSIS can be used to quantify the effect of each specific calibration step. For example, to estimate the influence of stray light on the retrieval of C_L, a PyROSIS simulation was performed in which the systematic error due to stray light was left uncorrected in the L1 calibration. As shown in Fig. 8, this leads to wavelength-dependent errors with maximum underestimation of radiance levels of 30%.

These differences in radiance levels lead to a complete failure of the retrieval: WASI estimates the suspended matter content to exactly zero in all cases.

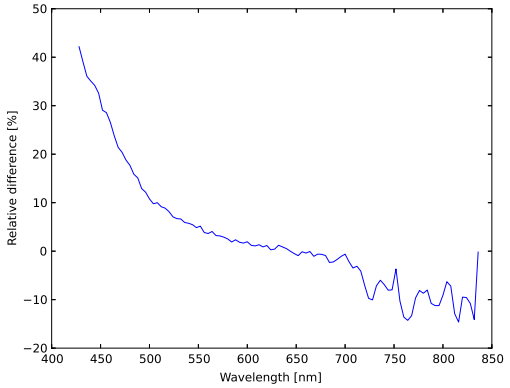

Fig. 8. (Color online) Relative difference between the averaged simulated radiance spectra with and without stray light correction.

6. Discussion

With PyROSIS, to the authors best knowledge, it is for the first time possible to compute the traceable measurement uncertainties for L1 data of hyperspectral sensors, and these kinds of analyses are required if remote sensing data products are to obtain credible measurement uncertainties.

Another feature of PyROSIS that was demonstrated is the assessment of the contribution of the individual uncertainties of the sensor properties to the combined uncertainty. This is needed to assess the improvement achievable through laboratory characterization. The conclusion of Subsection 5.D is that, due to the radiometric noise dominance, improved laboratory characterization procedures for other sensor parameters cannot improve the data quality. Instead, it motivates us to analyze the reduction of radiometric noise, which can be achieved through software or hardware binning of the data.

PyROSIS was used in conjunction with WASI to perform a complete end-to-end simulation to obtain combined measurement uncertainties for an end product based on sensor parameters. The example used in this study was the suspended matter concentration C_L. Possible next steps include the derivation of combined uncertainties for a more realistic multiparameter retrieval or derivation in combination with an atmospheric correction.

Finally, with PyROSIS, more realistic simulated spectra can be generated. This can assist the retrieval algorithm development if the algorithms can be designed considering sensor specific systematic effects. Also, the sensitivity of algorithms to sensor measurement uncertainties can be assessed this way.

7. Conclusion

In this paper, software capable of using imaging spectrometer characterization data to propagate measurement uncertainties through different product levels with a Monte Carlo approach has been presented. This is necessary to calibrate hyperspectral data in a traceable way and to expand previous studies concerning error propagation and estimation of hyperspectral data, such as [1,6,14]. While scene simulators are a prerequisite for algorithm development [15], this type of analysis is necessary for estimating the influence of sensor performance on data products, helpful for sensor optimization, and could assist algorithm development.

It is planned to expand this software to incorporate more instruments when characterization data of these sensors become available. Finally, this tool will be used to define scientifically motivated requirements for DLR's calibration laboratory and to identify limiting measurement procedures and equipment.

The author would like to thank Peter Gege and the anonymous reviewer for their valuable comments.

References

1. J. Beekhuizen, M. Bachmann, E. Ben-Dor, J. Biesemans, M. Grant, G. Heuvelink, A. Hueni, M. Kneubuehler, E. de Miguel Llanes, A. Pimstein, E. Prado Ortega, I. Reusen, T. Ruhtz, and M. Schaale, "Report on full error propagation concept," DJ2.1.2, EUFAR FP7 JRA2—HYQUAPRO (European Facility For Airborne Research, 2009).
2. H. Kaufmann, K. Segl, S. Chabrillat, S. Hofer, T. Stuffler, A. Mueller, R. Richter, G. Schreier, R. Haydn, and H. Bach, "EnMAP a hyperspectral sensor for environmental mapping and analysis," in *Proceedings of the IEEE International Conference on Geoscience and Remote Sensing Symposium, 2006* (IEEE, 2006), pp. 1617–1619.
3. Joint Comittee for Guides in Metrology, "JCGM 101: 2008, Evaluation of measurement data—Supplement 1 to the 'Guide to the expression of uncertainty in measurement'—Propagation of distributions using a Monte Carlo method," Tech. Rep. (Bureau International des Poids et Mesures, 2008).
4. R. O. Green, "Spectral calibration requirement for Earth-looking imaging spectrometers in the solar-reflected spectrum," Appl. Opt. **37**, 683–690 (1998).
5. P. Gege, "The water colour simulator WASI: an integrating software tool for analysis and simulation of optical *in situ* spectra," Comput. Geosci. **30**, 523–532 (2004).
6. P. Schwind, R. Müller, G. Palubinskas, T. Storch, and C. Makasy, "A geometric simulator for the hyperspectral mission EnMAP," presented at the Canadian Geomatics Conference, Calgary, Alberta, Canada, 15–18 June 2010.
7. R. Richter and D. Schläpfer, "Geo-atmospheric processing of airborne imaging spectrometry data. Part 2: atmospheric/topographic correction," Int. J. Remote Sens. **23**, 2631–2649 (2002).
8. A. Berk, L. S. Bernstein, and D. C. Robertson, "MODTRAN: a moderate resolution model for LOWTRAN 7," Tech. Rep. (Geophysics Laboratory, Air Force Command, U. S. Air Force, Hanscom Air Force Base, Massachusetts, USA, 1989).
9. H. Neckel and D. Labs, "The solar radiation between 3300 and 12500 Å," Sol. Phys. **90**, 205–258 (1984).
10. P. Gege, D. Beran, W. Mooshuber, J. Schulz, and H. van der Piepen, "System analysis and performance of the new version of the imaging spectrometer ROSIS," in *Proceedings of the 1st EARSeL Workshop on Imaging Spectroscopy* (European Association of Remote Sensing Laboratories, 1998), pp. 29–35.
11. J. Schulz, "Systemtechnische Untersuchungen an dem abbildenden Spektrometer ROSIS-01 zur Erfassung und Interpretation der Meeresfarbe," Ph.D. thesis (DLR Institut für Optoelektronik, 1997).
12. Y. Zong, S. W. Brown, B. C. Johnson, K. R. Lykke, and Y. Ohno, "Simple spectral stray light correction method for array spectroradiometers," Appl. Opt. **45**, 1111–1119 (2006).
13. K. Lenhard, P. Gege, and M. Damm, "Implementation of algorithmic correction of stray light in a pushbroom hyperspectral sensor," presented at the 6th EARSeL Workshop on Imaging Spectroscopy, Tel Aviv, 16–19 March 2009.
14. S. Lavender, O. F. D'Andon, S. Kay, L. Bourg, S. Emsley, N. Gilles, T. Nightingale, R. Quast, M. Bates, T. Storm, J. Hedley, M. Knul, G. Sotis, R. Nasir-Habeeb, and P. Goryl, "Applying uncertainties to ocean colour data," Metrologia **49**, S17–S20 (2012).
15. A. Börner, L. Wiest, P. Keller, R. Reulke, R. Richter, and M. Schaepman, "SENSOR: a tool for the simulation of hyperspectral remote sensing systems," ISPRS J. Photogramm. Remote Sens. **55**, 299–312 (2001).

Chapter 7

Summary, Conclusion and Outlook

7.1 Summary

The goals set in sec. 1.5 were reached, leading to demonstrable improvements to calibrated hyperspectral image data, and new and improved methods for traceable uncertainty propagation.

The first two objectives of this thesis were defined as:

1. Development and realization of a detailed measurement concept for a thorough sensor characterization. This includes the characterization of DLR's HySpex sensors.

2. Assessment of the potential improvements to calibrated hyperspectral data, and of the impact on the subsequent data analysis.

The optical facilities at DLR (the CHB) and PTB (PLACOS) were used to characterize DLR's NEO HySpex sensors. This is described in chapters 3 and 4. The immediate improvement resulting from these measurements is the possibility to assess the validity of the manufacturers' claims concerning the optical performance of the instruments, and to be able to assign uncertainties to the different sensor parameters.

The optical distortions, smile and keystone, of the HySpex SWIR sensor were found to be within the ranges specified by the manufacturer. Significant differences could be observed in the absolute radiometric calibration: Within the atmospheric spectral bands of water absorption, where airborne measurements are difficult due to the opacity of the atmosphere, and toward the long-wave end of the sensor's spectral range, where the measurement uncertainty of DLR's radiance standard, RASTA [59, 56], increases significantly. Lower measurement uncertainties of the radiometric calibration for the spectral range > 1700 nm will only be feasible after a better calibration of RASTA. Due to electronic effects caused either by the very short laser

pulses of PLACOS or by the saturation of some detector elements introduced by the measurement scheme, a stray light characterization could not be performed for this sensor.

For the HySpex VNIR sensor, the differences between the manufacturer's and our subsequent characterization are more important, as several systematic effects were identified:

- The original radiometric calibration data lead to striping in the calibrated hyperspectral images.
- A detector nonlinearity gave rise to noticeable signal offsets in the images and systematic errors for low signals.
- The optical distortions are about twice as large as stated by NEO, and the geometric and spectral resolutions are varying over the FOV by a factor of close to two.
- Differences in the absolute radiometric calibration and the omission of the stray light correction lead to distorted spectra.

For both spectrometers, we could find that, under laboratory conditions, their properties remained unchanged for the first 1.5 years of operation, within the uncertainties of the respective parameters. Note that only the characterization performed in this detail can lead to the traceability to the *système international d'unités* (SI) of the hyperspectral data, typically required by atmospheric correction and physics-based retrieval algorithms. The traceably calibrated data is also a requirement in order to be able to compare data of two hyperspectral sensors with each other.

The second benefit of the extensive characterization efforts is that this allows to improve the quality of the calibrated data directly. Chapter 4 explores the potential of correcting the discovered issues pertaining to the HySpex VNIR sensor using the supplemental characterization data. To that end, a calibration software was developed that is able to incorporate and use the additional knowledge. This software is embedded in DLR's operational processing chain for large optical remote sensing data sets from airborne and spaceborne sensors, CATENA [34]

The differences between the original calibration by NEO and the improved calibration by DLR were examined using the example of a water scene of lake Starnberg, from which the water depth was retrieved with WASI-2D [18] for the shallow water region. This application of remote sensing of water bodies was chosen as calibration issues are highlighted here due to the nature of the signal. First, most of the recorded signal stems from the atmospheric path radiance, which results in at-sensor-radiances that are very different from those used for the calibration, i.e. peaking in the blue instead of the infrared. Second, as the signal from the water body is much smaller

than the one originating from the atmosphere, calibration issues manifest themselves in failures of the atmospheric correction by yielding unphysical reflectances. Water depth was selected as higher level test parameter since it changes gradually over a large range, and accurate ground references could be obtained using echo sounding.

As immediately noticeable result of the correction of the known systematic effects, the artifacts striping and offset are removed from the hyperspectral image. A notable highlight of this study is that for all investigated calibration procedures, there exists a strong correlation between the water depth derived from the echo sounding measurements and from the HySpex data for the entire depth range of the echo sounding data set, i.e. up to 14 m. This is unexpected, as optical bathymetry should be feasible only up to the Secchi depth [14], which was determined as 4.2 ± 0.5 m.

As predicted due to the differences in at-sensor-radiance during laboratory radiometric characterization and airborne measurements, the stray light correction has the largest impact at shorter wavelengths, leading to changes of up to 20 % in the reflectance spectra for wavelengths < 450 nm. A sensitivity analysis shows that the stray light correction increases the water depth range for which the correspondence between optical and echo sounding data is better than 20 % from 8 m with the NEO calibration to 11 m with the improved calibration procedure. The sensitivity analysis also shows that the remaining wavelength-dependent radiometric uncertainties, caused by imperfect calibration, additional distortions in the spectra introduced by the atmospheric correction and an imperfect retrieval model should result in water depth errors of the observed magnitude. The spectral optical distortions were also corrected, i.e. the smile effect and the non-homogeneous spectral bandwidth, but without noticeable effect. This correction may be more important for retrievals relying on exact positions of spectral features.

In the second part of this dissertation, potential improvements to the generation of the traceability chain, including ameliorations to the determination of measurement uncertainty, were explored. The final two objectives were given as

3. Extension of the traceability of the calibration chain from the laboratory to airborne measurements

4. Derivation of requirements for laboratory characterization from target measurement uncertainties

and are addressed in the chapters 5 and 6.

Chapter 5 presents a software tool, the APEX Calibration Information System (Cal IS). This tool performs several roles within the calibration of APEX data: It provides a database of all laboratory characterization data (i.e., raw sensor data) and meta-data (i.e., the auxiliary laboratory data), and has an interface to the algorithms which perform the routine processing of the characterization data for generation of the sensor model. Furthermore, Cal IS supports the scientists analyzing the sensor's

characterization data with easy access to the database contents coupled with useful visualizations which is helpful in finding spurious sensor effects in the laboratory data.

One core feature of the Cal IS is that it intrinsically links provenance information to the calibration data sets. This means that, starting from a calibration sensor model, it can be easily traced back on which characterization data this model is based. By supplementing this information with the calibration of the respective radiance, spectral or angular standards, Cal IS allows to extend traceably the calibration chain from the primary standards to the data sets required for the calibration of hyperspectral image data.

The last publication in chapter 6 presents the implementation of a method to extend the calibration chain from the laboratory characterization measurements to airborne image data and derived products. Analytical uncertainty propagation methods cannot be used here, as some uncertainties, for example the influence of spectral shifts on the radiometry, and processing steps, such as resampling for the correction of optical distortions or stray light correction, are dependent on the spectra.

Therefore, the uncertainty propagation was performed with a Monte Carlo simulation of the data acquisition process. This also allows the use of a probability distribution function for each uncertainty associated with a sensor parameter that describes the given uncertainty correctly [30]. For this study, a sensor model of ROSIS, based on laboratory characterization data, was used; the scene consisting of a homogeneous water surface. The water spectrum was generated by the water color simulation and analysis tool WASI [17]. Since the content of the scene is well-defined, it can be analyzed and compared to that reference. This effectively allows to extend the propagation of laboratory characterization uncertainties to several product levels, i.e. in this case, the calibrated radiances and the retrieved concentrations of water constituents. Running the Monte Carlo simulation for variations of the ROSIS sensor model allows to assess the impact of the sensor model, or, effectively, of the laboratory characterization, uncertainties on results of airborne measurements.

7.2 Conclusion

Remote sensing of the Earth's surface using spaceborne instrumentation has become a central tool to monitor and understand the changes caused by global warming and other human influences [13]. As there is the need to track even small changes, the requirements for the measurement uncertainties of such sensors are often challenging to achieve [62].

This is especially true for radiometric measurements which remain difficult to perform with accuracies better than a few percent [33]. For this reason, hyperspectral satellite sensors are typically validated and vicariously calibrated using airborne sensors [64] and field spectrometers [43].

One of the objectives of this thesis was to apply advanced methods of sensor calibration to state-of-the-art commercial hyperspectral sensors. Now, for the first time, such an instrument is independently calibrated, with a depth similar to those of spaceborne instruments. This has direct, important consequences: the updated data calibration is able to provide data with significantly reduced systematic effects, and the calibration of hyperspectral imagery can now be traced back to the SI.

Data from DLR's imaging spectrometers can now be properly calibrated, which satisfies the "data uniformity" criterion given in [46]. This enables subsequent users of HySpex-generated data-sets to spend less time caring about systematic sensor effects which, for many other instruments, is not yet the case.

This is especially true for stray light which is currently only rarely characterized for airborne hyperspectral imagers: In discussions with sensor manufacturers and PTB, the consensus was that the stray light levels exhibited by the inspected HySpex VNIR are already quite low for this type of instrument. This means that other imaging and non-imaging (i.e., field) spectrometers are likely to exhibit stray light contributions of a similar magnitude. This is all the more important, as, due to the dependence of the actual at-sensor spectra, stray light issues can not be resolved by typical vicarious calibration schemes, or may be propagated through vicarious calibration schemes to the calibration of satellite sensor data.

The traceability of hyperspectral data to the international system of units which comprises the ability to assign uncertainties to data points, is a necessity for hyperspectral data, both for physics-based retrievals as for multitemporal and multi-sensor analyses [52]. This is achieved by characterization measurements performed using calibrated light sources, and supplemented by the software presented in the second part of this thesis: While tools such as the APEX calibration information system provide an easy interface for data analysis, their real value in this regard is that they gather the necessary information to describe the traceability chain.

As for the Monte Carlo simulation for the propagation of measurement uncertainties: This method allows to assess the contribution of laboratory uncertainties to higher-level processed data. Moreover, analyses of this kind can also assist the development of new hyperspectral data analysis methods, as the Monte Carlo simulation approach complements other sensor simulation tools [5, 57] by providing test data that reflects the uncertainties involved in the data acquisition.

7.3 Outlook

For both HySpex instruments, the laboratory characterization and calibration appears to be mostly complete. Regular checks for changes in the sensor model will be performed. Incremental improvements to the characterization methods available in the CHB remain possible, e.g. a calibration of DLR's radiometric standard with lower

uncertainties, a reduction of the inhomogeneities of DLR's integrating sphere [4] or a characterization method for the stray light of the HySpex SWIR which will in turn result in lower measurement uncertainties of the sensors. There is yet the need to ensure the proper operation of our HySpex sensors by monitoring their spectral and spatial characteristics during airborne data acquisition. As the CHB does not have a climate or pressure chamber to operate the sensors at environmental conditions similar to those found in airplanes, methods to detect changes based on airborne data will have to be employed [24, 25, 12, 9].

Many users of hyperspectral data are not fully aware of issues pertaining to data calibration and systematic errors, and may not realize that this may interfere with their analyses [46]. Thus, the knowledge about the need for independent validation of commercial hyperspectral sensors may need to be propagated through the hyperspectral Earth observation community.

Both airborne and spaceborne hyperspectral remote sensing are founded on ground-based reference measurements, using field instruments. Therefore, the requirements to calibration of the ground-based instruments need to be as stringent as those for airborne or spaceborne instrumentation. While, in principle, this has been recognized [51], many instruments still lack an independent characterization, or even regular function checks. Hence, this is an issue that should be further pursued within the possibilities of the CHB and which may necessitate building up additional measurement capabilities.

Finally, spaceborne hyperspectral instruments are often radiometrically calibrated [64] using the solar irradiance. Radiance based vicarious calibration or validation schemes may therefore profit as well from Sun-based radiometric calibration.

trometer for airborne remote sensing applications. NEWRAD 2014, Helsinki, Finnland.

Schwarzmaier, T., Baumgartner, A., Gege, P.and Lenhard, K., (2013) Calibration of a monochromator using a lambdameter. SPIE Remote Sensing 2013, Dresden, Germany.

Lenhard, K., (2013) Monte-Carlo based determination of measurement uncertainty for imaging spectrometers. WHISPERS 2013, Gainesville, FL, USA.

Baumgartner, A., Gege, P., Köhler, C., Lenhard, K.and Schwarzmaier, T., (2012) Characterisation methods for the hyperspectral sensor HySpex at DLR's calibration home base. SPIE Remote Sensing 2012, Edinburgh, United Kingdom.

Schwarzmaier, T., Baumgartner, A., Gege, P., Köhler, C.and Lenhard, K., (2012) The Radiance Standard RASTA of DLR's calibration facility for airborne imaging spectrometers. SPIE Remote Sensing 2012, Edinburgh, United Kingdom.

Lenhard, K., Baumgartner, A., Gege, P., Köhler, C.and Schwarzmaier, T., (2012) Characterization of DLR's EnMAP simulator. International Radiation Symposium 2012, Berlin, Germany.

Lenhard, K., Baumgartner, A., Gege, P., Köhler, C.and Schwarzmaier, T., (2012) Independent laboratory characterization of NEO HySpex VNIR-1600 and NEO HySpex SWIR-320M-E hyperspectral imagers. IGARSS 2012, Munich, Germany.

Schwarzmaier, T., Baumgartner, A., Gege, P., Köhler, C.and Lenhard, K., (2012) DLR's New Traceable Radiance Standard "RASTA". IGARSS 2012, Munich, Germany.

Schwarz, C.,Gege, P., and Lenhard, K. (2010): Concept For Fast Spectral Characterisation Of Imaging Spectrometers. ESA Hyperspectral Workshop 2010, Frascati, Italy.

Gege, P., Fries, J., Haschberger, P., Lenhard, K., Schötz, P., Schwarz, C., and Schwarzmaier, T. (2010): Concept for improved radiometric calibration of radiance sources at the CHB facility. ESA Hyperspectral Workshop 2010, Frascati, Italy.

Lenhard, K. and Baumgartner, A. (2010): Estimation of radiometric uncertainty after smile correction. ESA Hyperspectral Workshop 2010, Frascati, Italy.

Lenhard, K., Gege, P. and Damm, M. (2009) Implementation of algorithmic correction of stray light in a pushbroom hyperspectral sensor. EARSeL 2009, Tel Aviv, Israel.

Acknowledgments

First of all, I would like to thank my supervisor Peter Gege and my department head Peter Haschberger for giving me the opportunity to do this thesis, as well as their guidance, patience and feedback during my doctoral studies. I also would like to thank Michael Schaepman, Ross Purves and Andreas Hüni for agreeing to read and evaluate my thesis.

During my work at DLR, I received help from many people, without whom I could not have finished this work. This is especially true for Andreas Baumgartner and Thomas Schwarzmaier, who were always great to work with. I would also like to thank my former colleagues Christian Schwarz, Jürgen Fries, Paul Schötz und Willem Vreeling. From my students, I would like to thank Nicola Schneider and Valentin Reinhardt.

Also a great help, both for working and enjoying working here were Jürgen Wörishofer, Erich Bogner, Andreas Wenisch, Eva Fahrenschon and Sanja.

Everybody at NEO, Andreas Hüni and Michael Jehle deserve thanks.

I always valued and enjoyed the helpful and friendly atmosphere in our department, and while we did not actually work together, I am glad to have met Peter Vogt, Stefan Hoch, Easy, Anna Göritz, Philipp Grötsch, Philipp Neugebauer and Claas Köhler. I would also like to thank everyone who made the coffee breaks enjoyable: All of the above, as well as Felix Geiger, Tilman, Philipp Zigann, Manuel Mende, Oleg Kiselev and Marco Kirschner. Those who shared my enthusiasm for coffee, cinema and TV series, soccer and old computer games deserve additional thanks.

Katja I would like to thank for her patience, support and encouragement.

For sharing the suffering, thanks are going to the president of the "Politischer Gesprächs- und Skatkreis Schwarz-Rot-Gold Poppelsdorf."

Thanks also belong to everybody who proofread this thesis.

I would like to thank my father and Brigitte for their encouragement to actually do a thesis, and their moral support over all those years, and my siblings Johanna, Kristinar and Felix for making fun of me when I deserved it (always). From the Moroccan part of my family, special thanks are going to my grandfather, Anis, and Kenza.

Bibliography

[1] G. Acker, B. Hooker, R. Firestone, A. Barnes, W. Holmes, and E. Esaias. Memorandum SeaWiFS Volume 31 , Stray Light in the SeaWiFS Radiometer. *Nasa Technical Memorandum*, 1995.

[2] D. Antoine and A. Morel. *A multiple scattering algorithm for atmospheric correction of remotely sensed ocean colour (MERIS instrument): Principle and implementation for atmospheres carrying various aerosols including absorbing ones*, volume 20. Jan. 1999.

[3] G. Asner and K. Heidebrecht. Imaging spectroscopy for desertification studies: comparing AVIRIS and EO-1 Hyperion in Argentina drylands. *IEEE Transactions on Geoscience and Remote Sensing*, 41(6):1283–1296, June 2003.

[4] A. Baumgartner. Characterization of integrating sphere homogeneity with an uncalibrated imaging spectrometer. In *Proc. WHISPERS 2013*, Gainesville, FL, USA, 2013.

[5] A. Börner, L. Wiest, P. Keller, R. Reulke, R. Richter, M. Schaepman, and D. Schläpfer. SENSOR: a tool for the simulation of hyperspectral remote sensing systems. *ISPRS Journal of Photogrammetry and Remote Sensing*, 55(5-6):299–312, Mar. 2001.

[6] S. W. Brown, G. P. Eppeldauer, and K. R. Lykke. Facility for spectral irradiance and radiance responsivity calibrations using uniform sources. *Applied optics*, 45(32):8218–37, Nov. 2006.

[7] Y.-B. Cheng, P. J. Zarco-Tejada, D. Riaño, C. A. Rueda, and S. L. Ustin. Estimating vegetation water content with hyperspectral data for different canopy scenarios: Relationships between AVIRIS and MODIS indexes. *Remote Sensing of Environment*, 105(4):354–366, Dec. 2006.

[8] B. Cook, L. Corp, R. Nelson, E. Middleton, D. Morton, J. McCorkel, J. Masek, K. Ranson, V. Ly, and P. Montesano. NASA Goddard's LiDAR, Hyperspectral

and Thermal (G-LiHT) Airborne Imager. *Remote Sensing*, 5(8):4045–4066, Aug. 2013.

[9] F. Dell'Endice, J. Nieke, D. Schläpfer, and K. I. Itten. Scene-based method for spatial misregistration detection in hyperspectral imagery. *Applied optics*, 46(15):2803–16, May 2007.

[10] P. D'Odorico, E. Alberti, and M. E. Schaepman. In-flight spectral performance monitoring of the Airborne Prism Experiment. *Applied optics*, 49(16):3082–91, June 2010.

[11] P. D'Odorico, A. Gonsamo, A. Damm, and M. E. Schaepman. Experimental Evaluation of Sentinel-2 Spectral Response Functions for NDVI Time-Series Continuity. *IEEE Transactions on Geoscience and Remote Sensing*, 51(3):1336–1348, Mar. 2013.

[12] P. D'Odorico, L. Guanter, M. E. Schaepman, and D. Schläpfer. Performance assessment of onboard and scene-based methods for Airborne Prism Experiment spectral characterization. *Applied optics*, 50(24):4755–64, Aug. 2011.

[13] ESA. *The Changing Earth*. Number July. 2006.

[14] C. Flener. Estimating deep water radiance in shallow water : adapting optical bathymetry modelling to shallow river environments. *Boreal Environment Research*, 18:488–502, 2013.

[15] N. Fox, A. Kaiser-Weiss, W. Schmutz, K. Thome, D. Young, B. Wielicki, R. Winkler, and E. Woolliams. Accurate radiometry from space: an essential tool for climate studies. *Philosophical transactions. Series A, Mathematical, physical, and engineering sciences*, 369(1953):4028–63, Oct. 2011.

[16] GCOS. The Second Report on the Adequacy of the Global Observing Systems for Climate in Support of the UNFCCC. Technical report, World Meteorological Organization (WMO), Geneva, Switzerland, 2003.

[17] P. Gege. The water color simulator WASI : an integrating software tool for analysis and simulation of optical in situ spectra. *Computers & Geosciences*, 30:523–532, 2004.

[18] P. Gege. WASI-2D: A software tool for regionally optimized analysis of imaging spectrometer data from deep and shallow waters. *Computers & Geosciences*, 62:208–215, Jan. 2014.

[19] P. Gege, D. Beran, W. Mooshuber, J. Schulz, and H. van der Piepen. System analysis and performance of the new version of the imaging spectrometer ROSIS. In *Proceedings 1st EARSeL Workshop on Imaging Spectroscopy*, Zürich, 1998.

[20] P. Gege, J. Fries, P. Haschberger, P. Schötz, H. Schwarzer, P. Strobl, B. Suhr, G. Ulbrich, and W. J. Vreeling. Calibration facility for airborne imaging spectrometers. *ISPRS Journal of Photogrammetry and Remote Sensing*, 64(4):387–397, July 2009.

[21] H. R. Gordon. Atmospheric correction of ocean color imagery in the Earth Observing System era. *Journal of Geophysical Research*, 102(D14):17081–17106, 1997.

[22] R. Green, M. Eastwood, C. Sarture, T. Chrien, M. Aronsson, B. Chippendale, J. Faust, B. Pavri, C. Chovit, and M. Solis. Imaging Spectroscopy and the Airborne Visible/Infrared Imaging Spectrometer (AVIRIS). *Remote Sensing of Environment*, 65(3):227–248, Sept. 1998.

[23] R. O. Green. Spectral calibration requirement for Earth-looking imaging spectrometers in the solar-reflected spectrum. *Applied optics*, 37(4):683–90, Feb. 1998.

[24] L. Guanter, R. Richter, and J. Moreno. Spectral calibration of hyperspectral imagery using atmospheric absorption features. *Applied optics*, 45(10):2360–70, Apr. 2006.

[25] L. Guanter, K. Segl, B. Sang, L. Alonso, H. Kaufmann, and J. Moreno. Scene-based spectral calibration assessment of high spectral resolution imaging spectrometers. *Optics express*, 17(14):11594–606, July 2009.

[26] Headwall Photonics. Headwall Photonics website. `http://www.headwallphotonics.com/`, Dec. 2013.

[27] A. Hueni, K. Lenhard, A. Baumgartner, and M. E. Schaepman. Airborne Prism Experiment Calibration Information System. *IEEE Transactions on Geoscience and Remote Sensing*, 2013.

[28] ITRES. ITRES website. `http://www.itres.com/`, Dec. 2013.

[29] JCGM. Evaluation of measurement data — Guide to the expression of uncertainty in measurement. Technical Report September, Joint Committee for Guides in Metrology, 2008.

[30] JCGM. Evaluation of measurement data — Supplement 1 to the " Guide to the expression of uncertainty in measurement " — Propagation of distributions using a Monte Carlo method. Technical report, Joint Committee for Guides in Metrology, 2008.

[31] JCGM. JCGM 200 : 2008 International vocabulary of metrology — Basic and general concepts and associated terms (VIM), 2008.

[32] M. Jehle, A. Hueni, A. Damm, P. D'Odorico, J. Weyermann, M. Kneubühler, D. Schläpfer, and M. E. Schaepman. APEX - Current Status , Performance and Validation Concept. In *IEEE Sensors*, pages 533–537, Waikoloa, HI, USA, 2010.

[33] H. J. Kostkowski. *Reliable Spectroradiometry*. Spectroradiometry Consulting, La Plata, MD, USA, 1997.

[34] T. Krauß, P. D'Angelo, M. Schneider, and V. Gstaiger. The Fully Automatic Optical Processing System CATENA at DLR. In *ISPRS Int. Arch. Photogramm. Remote Sens. Spatial Inf. Sci., XL-1/W*, pages 177–181, Hannover, 2013. Copernicus Publications.

[35] F. Kruse, J. Boardman, and J. Huntington. Comparison of airborne hyperspectral data and eo-1 hyperion for mineral mapping. *IEEE Transactions on Geoscience and Remote Sensing*, 41(6):1388–1400, June 2003.

[36] B. Kunkel, F. Blechinger, D. Viehmann, H. Van Der Piepen, and R. Doerffer. ROSIS imaging spectrometer and its potential for ocean parameter measurements (airborne and space-borne). *International Journal of Remote Sensing*, 12(4):753–761, 1991.

[37] K. Lenhard. Determination of combined measurement uncertainty via Monte Carlo analysis for the imaging spectrometer ROSIS. *Applied optics*, 51(18):4065–72, June 2012.

[38] K. Lenhard, A. Baumgartner, P. Gege, S. Nevas, S. Nowy, and A. Sperling. Impact of improved calibration of a NEO HySpex VNIR-1600 sensor on remote sensing of bathymetry. *IEEE Transactions on Geoscience and Remote Sensing (submitted)*, 2015.

[39] K. Lenhard, A. Baumgartner, and T. Schwarzmaier. Independent Laboratory Characterization of NEO HySpex Imaging Spectrometers VNIR-1600 and SWIR-320m-e. *IEEE Transactions on Geoscience and Remote Sensing*, 53(4):1828–1841, Apr. 2015.

[40] K. Lenhard, P. Gege, and M. Damm. Implementation of algorithmic correction of stray light in a pushbroom hyperspectral sensor. In *Proceedings 6th EARSeL Workshop on Imaging Spectroscopy*, Tel Aviv, 2009.

[41] R. L. Lucke, M. Corson, N. R. McGlothlin, S. D. Butcher, D. L. Wood, D. R. Korwan, R. R. Li, W. A. Snyder, C. O. Davis, and D. T. Chen. Hyperspectral Imager for the Coastal Ocean: instrument description and first images. *Applied optics*, 50(11):1501–16, Apr. 2011.

[42] C. Lukashin, B. A. Wielicki, D. F. Young, K. Thome, Z. Jin, and W. Sun. Uncertainty Estimates for Imager Reference Inter-Calibration With CLARREO Reflected Solar Spectrometer. *IEEE Transactions on Geoscience and Remote Sensing*, 51(3):1425–1436, Mar. 2013.

[43] E. J. Milton, M. E. Schaepman, K. Anderson, M. Kneubühler, and N. Fox. Progress in field spectroscopy. *Remote Sensing of Environment*, 113:S92–S109, Sept. 2009.

[44] S. Nevas, M. Lindemann, A. Sperling, A. Teuber, and R. Maass. Colorimetry of LEDs with array spectroradiometers. *Mapan*, 24(3):153–162, Dec. 2009.

[45] S. Nevas, G. Wübbeler, A. Sperling, C. Elster, and A. Teuber. Simultaneous correction of bandpass and stray-light effects in array spectroradiometer data. *Metrologia*, 49(2):S43–S47, Apr. 2012.

[46] J. Nieke, D. Schlapfer, F. Dell'Endice, J. Brazile, and K. I. Itten. Uniformity of Imaging Spectrometry Data Products. *IEEE Transactions on Geoscience and Remote Sensing*, 46(10):3326–3336, Oct. 2008.

[47] Norsk Elektro Optikk. NEO HySpex website. `http://www.hyspex.no/`, Dec. 2013.

[48] Norsk Elektro Optikk. Web site of Norsk Elektro Optikk. `http://www.neo.no/`, Dec. 2013.

[49] N. Oppelt and W. Mauser. The Airborne Visible / Infrared Imaging Spectrometer AVIS: Design, Characterization and Calibration. *Sensors*, 7(9):1934–1953, Sept. 2007.

[50] B. Sang, J. Schubert, S. Kaiser, V. Mogulsky, C. Neumann, K. Förster, S. Hofer, and T. Stuffler. The EnMAP hyperspectral imaging spectrometer : instrument concept, calibration and technologies. In *Proceedings of SPIE conf. Imaging Spectrometry XIII*, volume 7086, pages 5–15, 2008.

[51] M. E. Schaepman. *Calibration of a Field Spectroradiometer*. PhD thesis, University of Zurich, 1998.

[52] M. E. Schaepman, S. L. Ustin, A. J. Plaza, T. H. Painter, J. Verrelst, and S. Liang. Earth system science related imaging spectroscopy—An assessment. *Remote Sensing of Environment*, 113:S123–S137, Sept. 2009.

[53] D. Schlapfer and R. Richter. Geo-atmospheric processing of airborne imaging spectrometry data. Part 1: Parametric orthorectification. *International Journal of Remote Sensing*, 23(13):2609–2630, 2002.

[54] J. Schulz. *Systemtechnische Untersuchungen an dem abbildenden Spektrometer ROSIS-01 zur Erfassung und Interpretation der Meeresfarbe*. PhD thesis, DLR Institut für Optoelektronik, Wessling, 1997.

[55] M. Schuster, S. Nevas, A. Sperling, and S. Völker. Spectral calibration of radiometric detectors using tunable laser sources. *Applied optics*, 51(12):1950–61, Apr. 2012.

[56] T. Schwarzmaier, A. Baumgartner, P. Gege, C. Köhler, and K. Lenhard. DLR's new traceable radiance standard "RASTA". In *Proc. IGARSS*, number 1, Munich, Germany, 2012.

[57] K. Segl, L. Guanter, C. Rogass, T. Kuester, S. Roessner, H. Kaufmann, B. Sang, V. Mogulsky, and S. Hofer. EeteS — The EnMAP End-to-End Simulation Tool. *IEEE Journal of Selected Topics in Applied Earth Observations and Remote Sensing*, pages 1–9, 2012.

[58] Specim. Specim website. `http://www.specim.fi/`, Dec. 2013.

[59] D. R. Taubert, J. Hollandt, P. Sperfeld, S. Pape, A. Höpe, K.-O. Hauer, P. Gege, T. Schwarzmaier, K. Lenhard, and A. Baumgartner. Providing radiometric traceability for the Calibration Home Base of DLR by PTB. In *Proc. Intern. Radiation Symposium 2012*, Berlin, Germany, 2012.

[60] S. Thiemann, P. Strobl, P. Gege, N. Stahl, W. Mooshuber, and H. van der Piepen. Das abbildende Spektrometer ROSIS. In *Wiss.-Techn. Jahrestagung der DGPF*, 2001.

[61] S. G. Ungar, J. S. Pearlman, J. A. Mendenhall, and D. Reuter. Overview of The Earth Observing One (EO-1) Mission. *IEEE Transactions on Geoscience and Remote Sensing*, 41:1149–1159, 2003.

[62] B. A. Wielicki, D. F. Young, M. G. Mlynczak, K. J. Thome, S. Leroy, J. Corliss, J. G. Anderson, C. O. Ao, R. Bantges, F. Best, K. Bowman, H. Brindley, J. J. Butler, W. Collins, J. a. Dykema, D. R. Doelling, D. R. Feldman, N. Fox, X. Huang, R. Holz, Y. Huang, Z. Jin, D. Jennings, D. G. Johnson, K. Jucks, S. Kato, D. B. Kirk-Davidoff, R. Knuteson, G. Kopp, D. P. Kratz, X. Liu, C. Lukashin, a. J. Mannucci, N. Phojanamongkolkij, P. Pilewskie, V. Ramaswamy, H. Revercomb, J. Rice, Y. Roberts, C. M. Roithmayr, F. Rose, S. Sandford, E. L. Shirley, W. L. Smith, B. Soden, P. W. Speth, W. Sun, P. C. Taylor, D. Tobin, and X. Xiong. Achieving Climate Change Absolute Accuracy in Orbit. *Bulletin of the American Meteorological Society*, 94(10):1519–1539, Oct. 2013.

[63] W. L. Wolfe. *Introduction to Imaging Spectrometers*. SPIE, Bellingham, WA, USA, 1997.

[64] World Meteoroligical Organization. *Guideline for the Generation of Satellite-based Datasets and Products meeting GCOS Requirements*, volume 128. 2009.

[65] X. Xiong, B. Wenny, J. Sun, A. Angal, A. Wu, H. Chen, T. Choi, S. Madhavan, X. Geng, D. Link, Z. Wang, G. Toller, W. Barnes, and V. Salomonson. Overview of Aqua MODIS 10-year on-orbit calibration and performance. In R. Meynart, S. P. Neeck, and H. Shimoda, editors, *Sensors, Systems, and Next-Generation Satellites XVI*, volume 8533. SPIE, Nov. 2012.

[66] Y. Zong, S. W. Brown, B. C. Johnson, K. R. Lykke, and Y. Ohno. Simple spectral stray light correction method for array spectroradiometers. *Applied Optics*, 45(6):1111–1119, 2006.

[67] Y. Zong, S. W. Brown, K. R. Lykke, and Y. Ohno. Simple matrix method for stray light correction in imaging instruments, 2009.